KU LEUVEN

ARENBERG DOCTORAL SCHOOL
Faculty of Bioscience Engineering

A Computational Framework for Individual Cell-based Models

from yeast sorting to red blood cell mechanics and beyond

Tim Odenthal

Dissertation presented in partial
fulfillment of the requirements for the
degree of Doctor in Engineering

December 2013

A Computational Framework for Individual Cell-based Models

from yeast sorting to red blood cell mechanics and beyond

Tim ODENTHAL

Supervisory Committee:
Prof. Dr. ir. André Maes, chair
Prof. Dr. ir. Herman Ramon, supervisor
Dr. Paul Van Liedekerke, co-supervisor
(INRIA, France)
Prof. Dr. ir. Kevin Verstrepen
Prof. Dr. ir. Hans Van Oosterwyck
Dr. Engelbert Tijskens
Prof. Dr. ir. Liesbet Geris
(Université de Liège and KU Leuven)
Prof. Dr. Dirk Drasdo
(INRIA, France and IZBI, Leipzig)

Dissertation presented in partial
fulfillment of the requirements for
the degree of Doctor
in Engineering

December 2013

Kasteelpark Arenberg 30 bus 2456, B-3001 Heverlee (Belgium)

D/2013/11.109/79

Preface

In my experience happiness has a lot to do with the fact that one can work for positive goals that are of great importance and that the work one has to do is in itself a lot of fun. When it comes to modelling and also measuring, this has often been the case – also thanks to the fun people around me. The goal to better understand the mechanics and behaviour of cells as they interact to form a functioning tissue has certainly been very motivating for me. In particular, I could identify very well with the more concrete goals of Prometheus, the skeletal tissue engineering inter-disciplinary group of KU Leuven, which strives to produce a combination product that allows to (more quickly) heal large bone defects. What is more, I hope that the modelling platform developed in this work will prove valuable in the future for other fundamental scientific and application-oriented questions.

The work described hereafter could not have been undertaken without the encouragement, support and help of a large number of people. Firstly, the basic lines of my research have been designed by Prof. Herman Ramon, whose capacity for genuine enthusiasm, generosity with lending out helpful books and sound advice are at the basis of this undertaking. My Co-Supervisor Paul Van Liedekerke supplied me with the most profound scientific help and discussions as well as challenges to my work, for which I am very grateful. None of the programming work with DEMeter++ would have been possible without Bert Tijskens, who is also the best advisor I know with respect to, amongst others, software design, debugging and (mechanical) modelling with particles. Prof. Hans Van Oosterwyck is owed an immense "thank you" for his time, keen interest, scientific discussions and incredible enthusiasm for trying out new ideas in the models.

For scientific collaboration I am indebted to Prof. Kevin Verstrepen and his lab, especially Marcelo Vinces, Joaquin Christiaens and Elisa van der Zande.

A great "thank you" goes to Dr. Sharon Jewel and Prof. Peter Petrov of the University of Exeter, who welcomed Kristina Šliogerytė and me and introduced us patiently to the micropipette aspiration technique.

I am also especially indebted to the group of Prof. Carmen Bartic, for all the help and support with the atomic force microscope provided by Andreea-Alexandra Ungureanu and Olivier Deschaume.

I am very grateful that I could be part of Prometheus. We had inspiring discussions, especially at the retreats, as well as a lot of fun together! I sincerely hope that our modelling work on 3D cell expansion as well as cell seeding will become more and more useful to the group and the goal of manufacturing bone-grafts.

The largest thank you goes to my colleague and friend Bart Smeets, without whom I could not have achieved this much – my feeling is that by working together so closely, we have accomplished far more than twice the amount of work that I could have accomplished by myself. It was especially great not only to be able to work together, but also to have fun together! I am also thankful for the other colleagues at MeBioS, in particular Kristina, Simon, Xavier and Janos! This brings me to the ALMA-crowd, Rodrigo, Wouter, Tjebbe, Ben, Bart L., Kenny, Tom, Soner, Catalin, Joe – who not only “spiced up” the ALMA experience, but who were also very helpful on occasion with scientific and administrative problems. I would also like to thank the very reliable and efficient secretaries of MeBioS for their patience with my foreign ideas and questions.

Last but not least I would like to thank my family – my parents for enduring longer talks about modelling cells than can be reasonably expected to be interesting for anyone not working in that field themselves, and above all my wife Inga – without your support, I wouldn’t have had the motivation and strength to pull through the rougher times during these four years of research at KU Leuven!

Abstract

The functioning of a biological tissue in many cases crucially depends on the mechanics at the cellular scale. This is shown in several example systems. Firstly, for a system of two phenotypes of yeast cells, which are adhesive and non-adhesive respectively, sorting occurs yielding a structure, in which the more adhesive cells are on the inside whereas the non-adhesive cells are on the outside. The Young's modulus of the two strains was measured in atomic force microscopy experiments showing no difference between the strains. Compared to the results of an individual cell-based model it is found that the difference in adhesion in combination with Brownian motion and the locality of growth of new cells suffices to explain the emergence of this shell-like structure.

In a second case, it is shown that the dynamics of initial cell spreading can be understood as a result of adhesion and dissipative forces at work on the interface of the developing contact plane. Especially for red blood cells, the model perfectly captures the experimental observations of two distinct experiments from the literature. A new deformable cell model with mechanistic contact interactions has been introduced to capture the developing adhesive contact. This model can be generalized to other cell types and applications in the field of individual cell-based models.

To simulate these and a wide variety of similar models, a C++ software platform with a python interface has been developed and its usefulness proven by above mentioned examples. It has been more widely applied together with colleagues to develop models for microcarrier cell expansion and a new formulation of the smoothed particle hydrodynamics method for low Reynolds numbers called NSPH.

Abbreviations

AFM Atomic Force Microscopy. 10, 12, 17, 19, 20, 22, 24, 37, 85, 98, 100, 106, 107, 109

BSA Bovine Serum Albumin. 90, 93

CD Contact Detection. 74

CG Conjugate Gradient. 27, 31, 55, 59, 74

DEM Discrete Elements Method. 77

DMT Derjaguin-Muller-Toporov. 28, 45, 120

DPD Dissipative Particle Dynamics. 7, 44, 64

FEM Finite Element Method. 2, 5

FENE Finitely Extensible Non-linear Elastic. 44, 52, 55, 57, 59–63, 65

IBM Individual cell-Based Model. 7–10, 26, 27, 39, 41, 42, 68, 69, 74, 77, 78, 80, 83–85, 111, 112

JKR Johnson-Kendall-Roberts. 28, 45, 47, 50, 74, 120

MA Micropipette Aspiration. 10, 12–15, 24, 85, 89, 90

MD Maugis-Dugdale. 44, 47, 49–51, 120

NSPH Non-Newtonian Smoothed Particle Hydrodynamics. 75, 78, 80, 84, 85

ODE Ordinary Differential Equation. 79, 80, 84

OT Optical Tweezers. 10, 12, 16, 24

PBS Phosphate Buffered Saline. 90, 93, 97, 98, 104

PDE Partial Differential Equation. 5, 79, 80

PLL Polylysene, ε-poly-L-lysine. 22–24

RBC Red Blood Cell. 7, 14, 24, 42, 44, 45, 48, 52–56, 58–62, 64, 65, 67, 68, 78, 86

RMSD Root Mean Square Deviation. 105, 120

SPH Smoothed Particle Hydrodynamics. 7, 72, 78, 80, 84, 86

TE Tissue Engineering. 2

TEM$_{00}$ fundamental Transverse ElectroMagnetic laser beam mode. 16

WLC Worm-Like Chain model. 52

List of Symbols

D diffusion constant. 111

E Young's modulus. 14, 22, 23, 37, 107

K membrane or cortex stretch modulus, 2D bulk modulus. 13

W total work of adhesion. 14, 23, 28, 29, 31, 35, 38

δ apparent overlap between contacting particles. 28, 29, 107

η_{m} membrane or cortex viscosity. 13

η dynamic viscosity constant. 27, 31, 111, 112

$\hat{E}$ reduced Young's modulus for contact between particles 1,2 with Young's moduli E_1, E_2 and Poisson's ratios ν_1, ν_2, $\hat{E} = \left(\frac{1-\nu_1^2}{E_1} + \frac{1-\nu_2^2}{E_2}\right)^{-1}$. 28, 29, 108

$\hat{R}$ reduced radius of contact between particles 1,2 with radii R_1, R_2, $\hat{R} = \left(\frac{1}{R_1} + \frac{1}{R_2}\right)^{-1}$. 28, 29, 100, 106–108

κ membrane or cortex bending modulus. 13

$\mathbf{F}$ force vector. 3, 27, 47, 50, 51, 54, 55, 75, 111, 112, 119

$\mathbf{v}$ velocity vector. 3, 27, 53–55, 75, 111, 119

$\mathbf{x}$ position vector. 3, 27, 31, 33, 43, 48, 49, 111

μ membrane or cortex shear modulus. 13

ν Poisson's ratio. 14, 23, 107, 108

ζ drag constant. 3, 111

k_{B} Boltzmann's constant. 111, 112

Contents

List of Figures

List of Tables

Chapter 1

Introduction

Nie umsonst.
Im Gebirge der Wahrheit kletterst du nie umsonst:
Entweder, du kommst schon heute weiter hinauf
oder du übst deine Kräfte,
um morgen höher steigen zu können.

Friedrich Nietzsche

1.1 Why develop a framework for computational cell mechanics?

Many fundamental human questions of life – Who are we? Where are we coming from? Where are we going? What is life? How can we fit in with our environment? – are basic questions for the biological sciences[1]. We are getting better and better at understanding the nature of the physical laws that govern our universe (e.g. this year's discovery of the Higgs' boson preliminarily completing the Standard Model of Physics (office 2013)), but regardless, we are still a long way from fully explaining even the simplest known life-forms. The sheer complexity of seemingly elementary organisms such as yeast makes the task impossible on the sole basis of traditional methods of mathematical reasoning supplemented with precise experiments (Noble 2002). Even though great advances have been made in measurement technology and theoretical

---

[1] "The Ultimate Question of Life, the Universe, and Everything" (Adams 2010) also starts with the biological aspect.

description of all basic parts of such an organism, it remains an unsolved challenge to predict its behaviour in more than some aspects.

We are becoming more successful at tackling this challenge through the use of computational models (Noble 2002). Although many recent computational approaches do not allow for rigorous mathematical verification of the predictions, they have proven to be a helpful tool to differentiate between important and secondary effects and to point out gaps in our knowledge or understanding. On occasion, they even have been found to directly further our understanding by exhibiting "emergent" behaviour that was previously not understood as an effect of the mechanisms programmed into the model (Anderson, Chaplain, Rejniak, et al. 2007). There are many advantages of doing "*in silico*" experiments with the available knowledge, the most obvious ones being comparatively low costs in money, time, and suffering of laboratory animals. In this way, computational models can make fact-gathering experiments more specific and effective.

In addition to the fundamental scientific quest, computational models have in many disciplines proven of utmost importance for engineering applications: The Finite Element Method (FEM) as well as finite volume or finite differences methods are routinely used in structural mechanics, for fluid dynamics applications and so forth (Zienkiewicz and Taylor 2000) and this methodology has drastically changed the design-process of new products. Similarly, the still developing discipline of Tissue Engineering (TE) is in urgent need of computational tools to facilitate its progress (Lenas, Moos, and Luyten 2009a,b).

There are, of course, many different tasks in biology that can be accomplished by employing computational models: Data extraction from experiments, interpolating from short-term measurements to long-term effects, prediction of chemical reactions, static responses and dynamic changes. Although several tools from other mathematical, physical and engineering disciplines can be directly applied to these modelling efforts, new tools have to be developed for aspects where existing ones do not suffice (Noble 2002).

One emerging field concentrates on the interplay between mechanical and biochemical aspects of a system (Li, Guan, and Chien 2005). There are many challenges in solely describing the mechanics of a living system, be it a large one, e.g. a skeletal joint, or a small one, e.g. a single cell. One of the key challenges lies in the so-called "multi-scale" nature of practically all biological mechanical systems that are being studied: Bones, for example exhibit mechanically important features from the hydroxylapatite crystal structure over collagen fibres to trabecular structures and the overall shape of the organ (Salgado, Coutinho, and Reis 2004). But also single cells have mechanically important features on several length-scales – from comparatively large-scale structures like the membrane and the nucleus to adhesion molecules and single actin fibres, which form a network (Boal 2012). While geometrically representing these diverse structures in a consistent way for a model poses a challenge, the complexity is enhanced by the fact that distinct “external” physical effects become important at the different length scales. This can best be illustrated by the different structures of the equation of motion for these elements: For the movement of an arm or leg, the well-known and intuitive Newtonian equation holds

$$m\mathbf{a} = \mathbf{F}, \tag{1.1}$$

which is a (vector) second order differential equation for the position $\mathbf{x}(t)$, $\mathbf{a} = \ddot{\mathbf{x}}$. However, on the cellular scale, inertia can be neglected due to the low Reynold’s number (Purcell 1977) yielding a first order equation of motion which is characterized by the friction or drag ζ term instead:

$$\zeta\mathbf{v} = \mathbf{F}, \tag{1.2}$$

where $\mathbf{v} = \dot{\mathbf{x}}$. On the scale of molecules, thermal agitation becomes a dominating force, requiring a stochastic (Langevin) equation of motion which adds a random component (Ullersma 1966):

$$m\mathbf{a} = \mathbf{F} + \mathbf{F}_{\text{rand}}. \tag{1.3}$$

Bearing these challenges in mind, we decided to start with models on the scale of the cell, the basic building block of all living organisms. Cells are not only ubiquitous in biological systems, they also form the most active and dynamic components of any biological system we are interested in studying, and many of their characteristics can be generalised. In addition, cell biology is one of the most intensely studied subjects since the time of van Leeuwenhoek (1632-1723), which means that ample experimental data already exist.

Since only comparatively recent experimental developments made it possible to characterise the mechanics at the scale of cells (or lower), and even more recently the computing power has become available to carry out longer-term simulations with many cells, we perceived a clear need for efficient tools for computational cell mechanics. In the highly complex systems of which cells are the determining constituents, mechanics plays a major role on three distinct levels. At the most basic level the response of the tissue to external forces is dictated by its constituents’ mechanics. At a higher level, the structure of any tissue is guided by the mechanical interactions during growth and remodelling. Both aspects are often reinforced by a feedback mechanism dubbed mechanotransduction – cells will adapt their behaviour (or, more specifically, their gene expression) and especially their mechanical properties depending on the microenvironment they find themselves in. Especially for tissue engineering, the mechanical microenvironment in which cells live has to be taken into account to arrive at the desired outcome. Therefore, the basic question targeted by the described research can be summarised as follows: In what ways and to what extent is a biological system (consisting of cells) influenced or even determined by the geometry of the cells and the physical interactions between them?

The tools we develop will be used more and more in the quest for a deeper understanding of the basic questions of the biophysical sciences, thereby shedding additional light on the basic human questions of life itself.

The next section will give a brief summary of the computational techniques that have been ready to use at the outset of this work or have become available since then.

1.2 Simulation techniques on the cellular scale

There are several quite distinct methods described in the literature which have the aim to model cell behaviour and interaction. It is important to point out that mechanics is not a major concern in many models, which focus on other means (generally chemical) of communication between cells. Since this emphasis is often up to the modeller employing a technique, the following description strives to include all major models of biological tissue which include the cellular scale. A distinction is made between the groups of computational methods, even though a distinction between mathematical descriptions could have been chosen as well. In that case, it would have become more obvious that the same mathematical model can be computed using very different computational means. Nevertheless, to motivate the choice of the computational methods in this work, it is most logical to proceed by explaining the different computational methodologies.

1.2.1 Mesh-based methods

The goal of simplification of all models of biological systems is probably to the largest extent achieved in methods involving cellular automata, a simulation technique which received wide appreciation after the publication of Conway's game of life (Gardner 1970). In this particular instance, a regular grid and just four rules can exhibit highly complex patterns which defy intuition. Introducing more specific rules, very similar techniques are being applied to elucidate the crucial governing mechanisms (or rules) in cellular systems, e.g. (Enderling, Anderson, Chaplain, et al. 2009; Morton, Hlatky, Hahnfeldt, et al. 2011) investigate the role of cancer (stem) cells using cellular automata on a square lattice.

More complex grids derived from Delaunay triangulations[2] may – to some extent –

---

[2] Delaunay triangulations are dual to the well known Voronoi tessellation, which divides space into elements according to a "seed" of points. Then each grid cell consists of all points in space which are closer to the given seed-point than to any other point of the seed.

overcome the implicit limitation of this type of model of “grid artefacts” stemming from the perfect regularity and connectivity of the grids’ cells (Zygourakis, Bizios, and Markenscoff 1991). They are under active development, especially in a three dimensional environment (Schaller and Meyer-Hermann 2005).

Yet another technique based on the idea that complex natural phenomena emerge from simple rules is the lattice-gas cellular automaton based method (Deutsch and Dormann 2004). A major advantage of these automata lies in the fact that continuum equations can be derived for specific rules, allowing for efficient bridging of the scales between cells and tissues or even organs.

A well-established method for different kinds of models on the cellular scale are the Glazier-Graner-Hoogeweg or Cellular Potts models (Graner and Glazier 1992). Thanks to the conceptual simplicity of being defined by one fundamental Hamiltonian[3] and the readily available software for calculating these models (*Compucell3D* n.d.), research interest in this type of model is high. The technique relies on a Monte Carlo-like scheme for updating lattice elements, where the probability of a grid cell to change from e.g. “inter-cellular space” to “(part of) a cell” depends on said Hamiltonian. In addition to questions about the appropriateness of the chosen probability density function, the author often did not find it trivial (and in some cases not even possible) to uniquely relate model parameters to observable physical parameters of the system.

All of the methods mentioned above are computationally very attractive, since (fixed) meshes allow for efficient calculation of the interactions and give an excellent opportunity for parallelised computing.

Finally, typical continuum methods are being used to describe phenomena at a given scale: On tissue level, Partial Differential Equations (PDEs) can be used to describe the development of e.g. an organ or a tumour (Graziano and Preziosi 2007). These models are extremely attractive, since PDEs can be analysed in a strict mathematical way, allowing for rigorous proofs of some results[4]. A drawback incurred by the homogenisation necessary for the continuous field description is the loss of information at the distinct, individual cell level. These methods known from structural mechanics (and often simulated using the FEM or finite volume simulation techniques) are also being applied on the single-cell level (Barreto, Clausen, Perrault, et al. 2013; Herant and Dembo 2010), yielding well-understood and precise model predictions. However, it is currently impossible to construct this type of model for problems spanning the size-range from single cells to large numbers of cells. Since these simulations are typically performed in a quasi-static way, highly dynamic systems pose another hurdle which cannot be overcome by today’s computing power.

---

[3] The Hamiltonian is an energy function defined by a vector field, which fully describes the dynamics of a (classical mechanical) system together with Hamilton’s equations.

[4] The non-linearity and complex interactions of many of these systems explain the need for computational rather than mathematical evaluations.

1.2.2 Mesh-less methods

Without a mesh, all problems and benefits attached to meshes are obviously void: Mesh artefacts do not play a role any more, but the computational advantage of dealing with well-defined interactions has also vanished. Therefore mesh-less methods generally require more computational (and in some cases algorithmic) effort in systems where a static mesh is appropriate. For highly dynamic simulations of biological systems on the cellular scale, however, frequent re-meshing heavily restricts this advantage (Herant and Dembo 2010), or may even make these problems intractable with mesh-based methods.

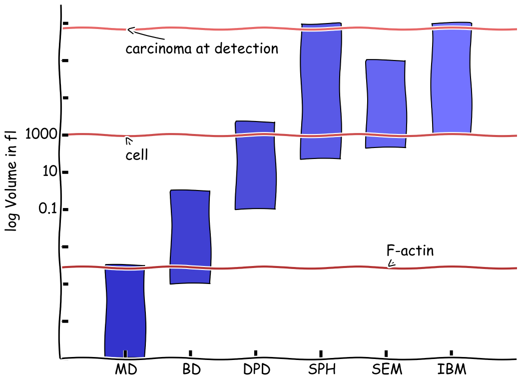

Figure 1.1: Very approximate length scales where the described mesh-less methods are applicable in fl = μm^3. “MD” stands for Molecular Dynamics, “BD” signifies Brownian Dynamics, “DPD” means Dissipative Particle Dynamics, “SPH” are Smoothed Particle Hydrodynamics, “SEM” is the acronym for Sub-cellular Element Models and finally “IBM” are the Individual-cell Based Models.

In the following we will strive to summarise mesh-less or off-lattice simulation techniques from lowest to larger scales (figure 1.1), although there is no clear-cut size-range for some of the described methodologies.
At the lowest scales, Molecular Dynamics simulations can help to elucidate the assembly of larger structures like membranes or parts of the cytoskeleton in the cell, for instance actin-cofilin interaction (Wriggers, Tang, Azuma, et al. 1998). Coarse-graining these methods yields the so-called Brownian Dynamics simulations, which describe whole molecular assemblies as single particles and define appropriate potentials between these coarse-grained actors. These particles are subject to Brownian Motion (hence the name of the method). Brownian Dynamics are very successful at explaining

the mechanics at the scale of cell-organelles, e.g. describing the micro-rheology of an actin network (Kim, Hwang, Lee, et al. 2009). At larger scales, when the Brownian particles might interact via hydrodynamic interactions, a method called Stokesian Dynamics (Brady and Bossis 1988) may be appropriate if the Reynold's number is still small for the particles or cells in suspension. Unfortunately, it is currently still impossible to use these methods to investigate whole cell behaviour or even cell-cell interaction, since the number of particles and the computational domain would be orders of magnitude too large for computations using the Brownian particles.

Instead, several groups homogenise rheology of cell compartments, which yields an interesting class of simulation techniques variously called the Sub-cellular Element Method (Newman 2005), or modelling the cell as "a granular medium" (Maurin, Canadas, Baudriller, et al. 2008), or the Cellular Particle Dynamics method (Kosztin, Vunjak-Novakovic, and Forgacs 2012), amongst others. While cell shape dynamics can be described very successfully by these methods, in some cases many internal elements of the cells do not exhibit very interesting behaviour but merely act as a viscous fluid.

The idea of a modelled cell which is filled with a viscous liquid has lead to the specialisation of the Smoothed Particle Hydrodynamics (SPH) method for dynamical cell-mechanics simulations (Van Liedekerke, Tijskens, Ramon, et al. 2010). This technique is uniquely suited to investigate impact and rupture phenomena, but it is limited to small time-scales due to the required small time-step of the SPH method, even though it can be extended by appropriate multi-scale simulation techniques (Ghysels, Samaey, Tijskens, et al. 2009; Van Liedekerke, Ghysels, Tijskens, Samaey, Smeets, et al. 2010). In principle, SPH allows for simulations of systems described by Navier-Stokes dynamics up to the astronomical scales, for which the technique was originally developed (Gingold and Monaghan 1977).

Another meso-scale simulation technique employed to address single-cell dynamics is Dissipative Particle Dynamics (DPD). Especially for Red Blood Cell (RBC) modelling, DPD has received wide recognition (Dao, Li, and Suresh 2006; Fedosov, Caswell, and Karniadakis 2010; Fedosov, Lei, Caswell, et al. 2011; Peng, Li, Pivkin, et al. 2013). The method is more closely related to Brownian Dynamics than SPH since it explicitly considers thermal agitation. An in-depth comparison of SPH and DPD can be found in (Español, Serrano, and Zuñiga 1997).

All those meso-scale methods are still comparatively expensive to compute for long-time, many-cell simulations. Therefore (Drasdo, Kree, and McCaskill 1995) introduced a method coarse-graining to a level of describing the complete cell as a homogeneous (visco-) elastic solid. At this level of homogenisation, large-scale, long-term simulations become possible, elucidating phenomena on the scale of tumours (Hoehme and Drasdo 2005; Macklin, Edgerton, Thompson, et al. 2012) or even on the organ-level (Hoehme, Brulport, Bauer, et al. 2010). The development of these Individual cell-Based Models (IBMs) has been pushed forward in several distinct fields, e.g. modelling *dictyostelium* *discoideum* (Palsson and Othmer 2000) or (bacterial) biofilms (Kreft, Picioreanu, Wimpenny, et al. 2001). It is an extremely interesting technique to analyse (mechanical) aspects of *in-vitro* experiments (Drasdo, Hoehme, and Block 2007; Galle, Loeffler, and Drasdo 2005; Krinner, Hoffmann, Loeffler, et al. 2010; Smeets, Odenthal, Tijskens, et al. 2013), since experimental cell numbers can be routinely obtained in the simulations as well. IBMs can be adapted to not only investigate cell-cell, but also cell-substrate interactions, as showcased in e.g. (Dunn, Fletcher, Chapman, et al. 2012; Schlüter, Ramis-Conde, and Chaplain 2012). Finally, intra-cellular information can be included by the use of (typically) ordinary differential equations for each individual cell, yielding a multi-scale simulation (Ramis-Conde, Chaplain, Anderson, et al. 2009).

As a software-package, both CHASTE[5] (Mirams, Arthurs, Bernabeu, et al. 2013) and FLAME[6] (Holcombe, Coakley, and Smallwood 2006) had been available as an open-source platform for IBMs at the outset of this work, but were deemed immature and lacking with respect to the implemented mechanical models at the time. Since then, CellSys[7] (Hoehme and Drasdo 2010) has also been made available, albeit only in a rigid, close-sourced version.

From this brief overview of techniques and tools which are available, it is clear that the proposed framework for IBMs described in this thesis is situated in field of research which rapidly advances on both the theoretical as well as the software side.

We have opted for the field of Individual cell-Based Models, since apart from its large range of applications, it has the following appealing properties, amongst others:

- Length-scale range from single cell investigation to tissue architecture in 3D environments,
- Mechanically sound formulations possible, well founded on canonical physical theory,
- Parameters of the models are accessible by available experimental methods,
- Large (time-)scale simulations possible with today's computing power,
- Direct application for design of biological (culture) systems seems in reach,
- Using multi-scale simulation techniques, information at lower scale can be included.

Nevertheless, the design of the framework has been heavily influenced by the notion that other techniques have to come into play when their particular strengths promise more accurate results, which is why the design has to be very modular.

---

[5] `http://www.cs.ox.ac.uk/chaste`

[6] `http://www.flame.ac.uk`

[7] `http://msysbio.com/software/cellsys`

1.3 Goals of the framework for computational cell mechanics

The basic research question addressed by the group of computational cell mechanics at MeBioS is: In what ways and to what extent is a biological system (consisting of cells) influenced or even determined by the geometry of the cells and the physical interactions between them? To our mind, the aspect of spatial interactions, mechanical signalling and the dynamics (changes in time) caused by these fundamental physical facts is still under-appreciated by many researchers, especially in the biomedical field. Obviously, a sufficiently developed simulation platform with intuitive, directly measurable parameters could provide the means to such researchers currently entirely focused on “chemical signalling” to also take spatial and mechanical effects into account.
In addition, there is a wealth of theoretical knowledge from the engineering and physics communities which can be directly applied to biological problems. Thus, one of the basic motivations to develop such a framework for IBMs was to provide a stepping stone between the disciplines towards both more fruitful collaboration and quicker scientific advances.

It is clear that the framework has to showcase its abilities to the closer and wider community to be accepted, so it was challenged even from the very early stages with acute problems such as socio-evolution in yeast (Odenthal, Smeets, Christiaens, et al. 2012; Smeets 2010) and cell culturing for bone tissue engineering (Smeets, Odenthal, Tijskens, et al. 2013; Smeets, Odenthal, Van Oosterwyck, et al. 2012). A final goal was to also contribute to the theoretical/modelling advances in the field by providing an improved means to cope with large cell deformation in IBMs.

Furthermore, since the parameters needed for the proposed models are neither readily retrieved from literature nor routinely measured by many bio(medical) groups, it was determined that suitable measurement techniques had to be investigated and protocols established to accomplish the necessary experiments.

The concrete goals of this work can thus be summarised as follows:

1. Provide a flexible software platform for IBMs or, more generally, mechanical/physical simulations of biological systems at the cellular scale.
2. Establish measurement techniques for at least the most crucial parameters needed for these simulations.
3. Apply the developed simulation and measurement techniques in problems in yeast-interaction modelling and for cell cultures in bone tissue engineering.

4. Advance the current state of the art in simulation technique by tackling the most important open challenges encountered in these endeavours.

To attain these goals, several developments have been pushed forward simultaneously both in the experimental and the computational fields. They are organised as follows in this thesis: In chapter 2, we point out what can be experimentally found about the mechanical state of cells, focusing on the most common and versatile techniques: Micropipette Aspiration (MA), Optical Tweezers (OT), and Atomic Force Microscopy (AFM). Experimental results obtained by the author with both MA and AFM are reported.
In chapter 3 – derived from (Odenthal, Smeets, Christiaens, et al. 2012) – we apply an IBM to an interesting hypothesis concerning the possible evolution of a social trait in baker's yeast, exemplifying the power of a classical IBM.
In chapter 4 – derived from (Odenthal, Smeets, Van Liedekerke, et al. 2013, the first two authors contributed equally to this work) – we extend the concepts of IBMs by introducing a versatile deformable cell model, focusing on the adhesive contact formation during initial cell spreading.
Following these descriptions of the applications of the modelling platform, the concepts of the software platform behind these developments are explained in chapter 5.
Finally, chapter 6 summarises the achievements and outlines directions for future research.

Chapter 2

Measuring mechanical properties of materials on the cellular scale

La lutte elle-même vers les sommets
suffit à remplir un cœur d'homme.
Il faut imaginer Sisyphe heureux.

Albert Camus

Introduction

At first glance, developing a modelling platform for (the mechanics of) cellular systems does not require the author to carry out experiments himself or herself. There are several reasons why this is nonetheless of crucial importance for building useful models for cellular systems. Mainly, to adapt a model specifically for a given experiment, it is in most cases required to measure the parameters in this particular system. Even though a wealth of information exists in the literature, living systems are so complex that it is highly unlikely for existing data to suffice in order to predict the behaviour in the system of interest, especially since in research the topic will typically be chosen for its novelty. As a consequence, it is a simple necessity for the modeller to obtain new experimental data. While in principle this could be accomplished by strategic collaborations, there are several advantages in performing the measurements oneself (from the modeller's perspective):

- Working with a cellular system may give "intuitive insights" into its behaviour: for example, while it is known theoretically that inertia are negligible in the systems of study, one intuitively still tries to "shake loose" a piece of a lysed cell that contaminates the micropipette in one of the initial experiments by "quickly" moving the pipette back and forth. For us living our whole lives in high Reynold's number environments, this is a very natural thing to do, but on the microscopic scale, such a reciprocal motion cannot yield the desired result (cf. "Scallop theorem"). Working with the pipettes and cells yielded the "discovery" that it was indeed impossible to get rid of the contamination, and that a freshly prepared micropipette had to be used instead.
- Since it is still less common in the biological sciences than in the physical sciences to provide (exhaustive) error estimates, the modeller often has to investigate these aspects himself or herself to be able to assess how much variability is inherent to the biophysical parameter measured, and what measurement error might be added by the tools used in the experiment – and especially how this could be minimized.
- It is not always obvious which parameters are experimentally (well) accessible unless one tries to measure them oneself. This assessment obviously has to influence both model construction and especially interpretation of the results of a model.

Summarizing, this means that by performing both the micropipette aspiration assays as well as the atomic force microscopy experiments presented, one not only obtains a "feeling" for the microscopic systems under study, but also valuable data needed for the development of an individual cell-based model.

Several methods are available to measure mechanical properties on microscopical to nanoscopical scales. In recent years, advances in micro- and nanotechnology as well as microscopy have allowed for increasingly precise determination of a cell's properties. To characterize cell mechanics in particular, three techniques are of major importance. Two of these have been investigated as means to substantiate the modelling work with parameters for the specific research questions with which the individual-cell based modelling platform is challenged in the present work. These experimental methods – (now) available at KU Leuven – are Micropipette Aspiration and Atomic Force Microscopy. Since literature data obtained by this method are used in this thesis, Optical Tweezers will be briefly described as well. Other methods, notably traction force microscopy or micro-rheological techniques are not described to keep the focus on the primary techniques yielding (statical) mechanical parameters of materials at the cellular scale. Parameters as primarily obtained by the described methods are used in the modelling platform presented in this thesis.

2.1 Micropipette Aspiration

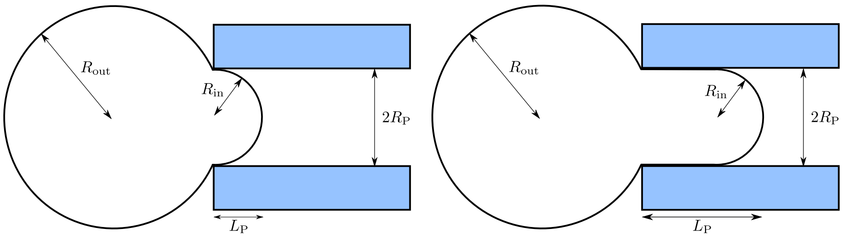

(a) Low ΔP (b) High ΔP

Figure 2.1: Micropipette Aspiration methodology. A cell is aspirated with a low suction pressure (a), or a high suction pressure (b).

The technique that uses the cheapest and most common laboratory materials for measuring cell mechanics is MA. The basic idea is to investigate cells or vesicles in a buffer suspension, see figure 2.1. The cells are aspirated into the pipette with a known pressure difference ΔP between the chamber containing the buffer and cells and the micropipette pressure system. From microscopic images, one can measure the radius of the pipette R_{P}, the length of the intrusion of the cell L_{P} as well as the outer (and if necessary inner) radius of the cell R_{out}, see figure 2.1. Knowing the cell radius and assuming rotational symmetry, one can calculate the cell's volume.

It is clear that the length of the intrusion L_{P} for a given pressure ΔP depends on the mechanical properties of the cell, which can be extracted applying an appropriate model of the cellular structure. To obtain reliable absolute results for e.g. cell stiffness which compare well to measurements using other techniques, profound prior knowledge of the cells measured and subtle analysis[1] are required. In principle, however, several interesting parameters can be measured in this way: the bending modulus of the membrane/cortex κ, the stretching modulus of the membrane/cortex K, the shear modulus μ, and, applying a pressure jump, also the membrane viscosity η_{m} can be

---

[1] (Henriksen and Ipsen 2004) describe a “model free” approach which makes do with fewer and more general assumptions than other methods. Their method requires comparatively complex theory to extract the mechanical parameters, but promises high precision and results which are comparable to e.g. AFM measurements.

extracted (Baaijens, Trickey, Laursen, et al. 2005; Discher, Boal, and Boey 1998; Evans 1980; Henriksen and Ipsen 2004; Hochmuth 2000; Jafari Bidhendi and Korhonen 2012). Additionally, an averaged Young's modulus E can be extracted (supposing a Poisson's ratio ν), as a measure for overall cell stiffness.

Interestingly, the technique can be extended to measure cell adhesion properties by reporting the minimum pressure ΔP required to pull an adhering cell loose with a micropipette, thereby obtaining a measure for the total work of adhesion W, (Chu, Dufour, Thiery, et al. 2005; Chu, Thomas, Eder, et al. 2004; Werner 2004).

The manual work involved in measuring a number of cells to obtain statistically significant results is considerable. In particular, the preparation of pipettes and pressure system require both time and training, see protocol in the appendix (A), as well as (Altinisik 2011).

The following results were obtained during a research stay of Kristina Šliogerytė and the author (7th-18th June 2010) at the University of Exeter, supervised by Prof. Peter Petrov and Dr. Sharon Jewel.

2.1.1 Results of MA trials in Exeter

First, it is shown that on the basis of the protocol explained in appendix A it is possible to aspirate RBCs, figure 2.2. Due to technical difficulties ascertaining the exact scale of the MA setup, no numerical validation was possible. In addition, the angle under which the RBC is aspirated makes it impossible to extract meaningful data: Most methods to analyse cell-stiffness require that the cell is aspirated at a point of low curvature, for an RBC that means ideally the concave centre of the biconcave shape. Despite several attempts, due to the inexperience in these experiments, an RBC could not be caught from the correct angle.

In addition to learning the MA technique, the goal of the research stay in Exeter was to find out, whether the cell wall stiffness of yeast cells was amenable to MA measurements. Despite dedicated and patient trials, the yeast cells could not be properly aspirated. The limitation to the method preventing successful aspiration seems to be that cells with a rough, stiff cell wall are not amenable to aspiration, since the wall deforms too little to effectively seal the micropipette, making it impossible to apply a suction pressure. However, the cells can be held by a constant flow of buffer into the MA pressure system, see figure 2.3.

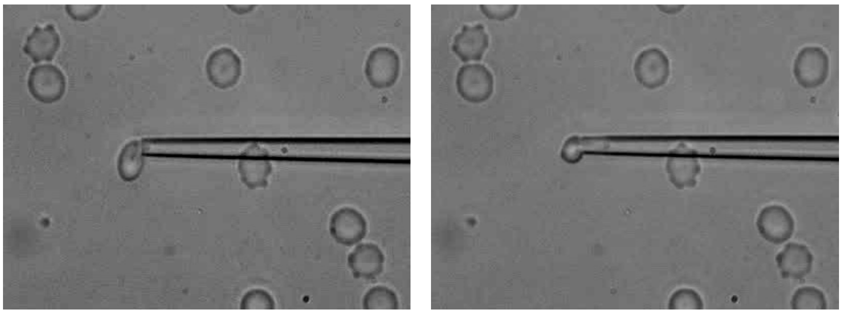

(a) $\Delta P = 0, t = 0\,\mathrm{s}$ (b) $\Delta P = P_{\max}, t = 42\,\mathrm{s}$

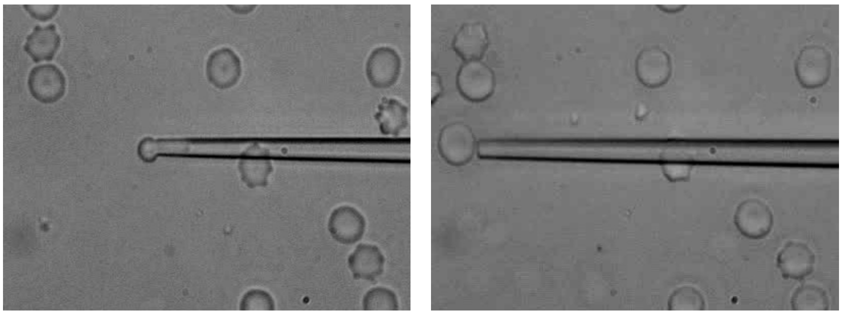

(c) $\Delta P = P_{\max}, t = 100\,\mathrm{s}$ (d) RBC final, $t \sim 600\,\mathrm{s}$

Figure 2.2: Micropipette Aspiration trial of RBC. After aspirating a cell, the pressure difference is adjusted to minimal deformation (a), then a pressure step is induced by quickly moving the reservoir to its lowest position, and the cell deforms; creep can be seen (b), (c). Finally the cell is released, and it returns to its original shape (d).

2.1.2 Conclusions micropipette aspiration

The conclusion can be drawn, that a limitation to the MA technique is that it requires the vesicles or cells to have comparatively deformable, smooth membranes to be aspirated. If that is the case, the technique is comparatively cheap and flexible.

The development of MA at KU Leuven has been further pursued by the Master thesis of Fadil Altinisik (Altinisik 2011) and used in measurements on ATDC5 cells under different osmotical stress conditions by Kristina Šliogerytė.

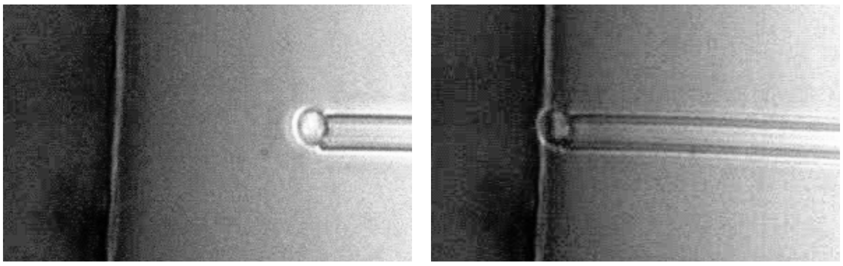

(a) “Aspirated” yeast cell

(b) Pushed against chamber wall

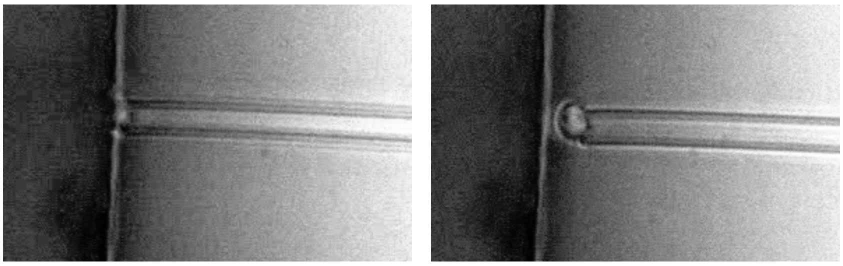

(c) Deforming chamber wall

(d) After pushing

Figure 2.3: Micropipette Aspiration trial of a yeast cell. A cell is “aspirated” with a constant flow of buffer into the micropipette. Yeast cells are stiff enough to deform the chamber wall of the parafilm chamber, see sub-figures (b) to (d).

2.2 Optical tweezers

OT are a highly sensitive means of probing biological materials at small forces. To measure force and displacement of single molecules or more complex structures, these are coupled to a (sub)micron-sized dielectric bead. This bead is trapped in (or slightly downstream of) the focus point of a strong, tightly focused laser beam. In cases where the wavelength of the light is considerably shorter than the beam size, refraction and the momentum carried by the refracted photons can explain the trapping effect: Due to the different optical density of the dielectric, off-centre rays are refracted by the bead through the optical axis. This change of direction of the light imparts a momentum to the bead. If the bead is in the centre of the trap, this momentum transfer perpendicular to the optical axis cancels out precisely for a symmetrical beam mode (typically TEM_{00}). If, on the other hand, a particle is off-centre, more rays will transverse it on the side of the centre, imparting more momentum towards the centre. This yields a net force towards the optical axis. If the bead is centred, the momentum imparted by the refraction pulls the particle in the opposite direction of the impinging light. The resulting force is cancelled by the momentum transferred by scattered photons, which pushes the bead along the the axis of impinging light. This typically traps the bead slightly downstream of the beam waist (Ashkin 1970; Tipler 2000).

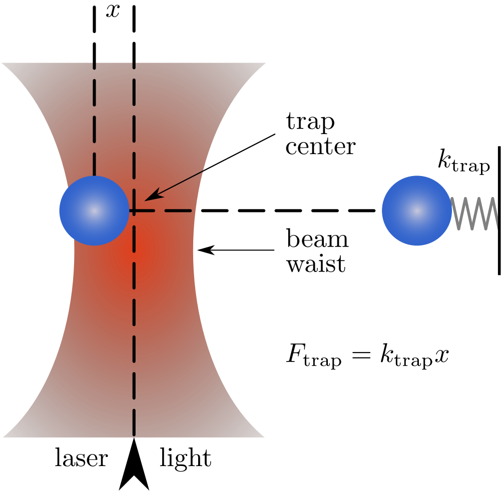

Figure 2.4: Working principle of optical tweezers (OT). A dielectric bead is attracted to the centre of the tightly focused laser beam, slightly above the beam waist. The force applied on the object depends linearly on its displacement from the trap centre, comparable to a Hookean spring system.

If the particle is displaced by an external force, the opposing trapping force is a linear function of the displacement x for small x. This allows measurements of forces in the piconewton (pN) range. The technique is therefore very useful to elucidate mechanical properties of single-molecules or cytoskeleton elements, but less so for global cell mechanical properties, where forces can be in the nanonewton (nN) range. For very soft cell types, the technique allows for highly controlled and precise cell stretching experiments, see chapter 4.2.1.

2.3 Atomic Force Microscopy

AFM is a high-precision method to characterize (and manipulate) surfaces at the microscopic and nanoscopic scales (Binning 1986; Radmacher 1997; Suchodolskis, Feiza, Stirke, et al. 2011). A very complete but in some respects out-of-date review on the technique is provided by (Cappella and Dietler 1999). The principle of how it works is shown in figure 2.5: The surface that is to be analysed is contacted by a nano-fabricated tip attached to a flexible cantilever. The bending of the cantilever is registered by a laser beam which is used as an extended pointer, read out by a subdivided[2] photo diode. The signal produced by this photo diode feeds back into a controller, which adjusts the height of the cantilever so that the laser beam stays centred on the diode, while the tip is pulled in a line over the surface. The height information of that line can be extracted from the corrections the controller performs. In this way, a surface can be scanned line-wise – which explains the alternate name “scanning force microscopy” given to the technique – and the 3D information can be assembled into a height image.

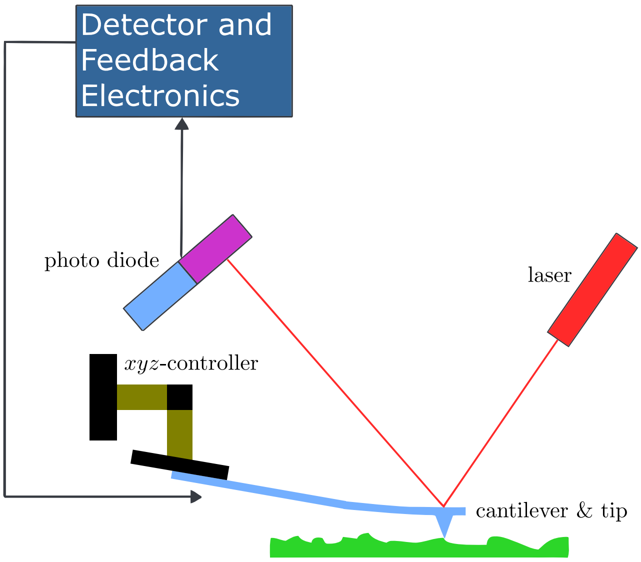

Figure 2.5: Working principle of atomic force microscopy (AFM). A deflection of the cantilever produces a change in the differential signal of the photo diode, which feeds back to the height (z-) controller. Adapted from (OverlordQ 2009).

There are several alternative imaging modes available on most devices based on driven oscillations of the cantilever; feedback can then be tuned on changes due to the (intermittent) interaction with the surface either of the amplitude, or the frequency, or the phase shift of these oscillations. Which mode is used depends on the surface that

---

[2] Typically, an AFM photo diode is divided into four fields, to not only report vertical cantilever deflection, but also the lateral deflection. Although the latter axis cannot be corrected by the piezo-controllers, it may be useful in later analysis of the data, and it can be used to find good imaging parameters.

needs to be characterized, the desired results, the tip, and the cantilever stiffness (and the experience of the operator).

In addition to imaging, AFM can be used to characterize magnetic properties and electric potentials and even conductivity of the sample surface. Furthermore, an AFM device can be used to re-arrange features on a given sample.

Remark 1 (Matterhorn vs. box of apples)**.** *A nice simile elucidating the enormous resolution of an AFM device is the following: Under ideal conditions, the atom lattice structure of a sample can be visualized by AFM (and it was indeed the first technique that allowed that resolution) (Giessibl 2003). If one pictures the atoms at the size of apples, the tip attached to the cantilever (see figure 2.5) would correspond to the size of the Matterhorn.*

Most importantly for characterising the mechanics of biological samples, an atomic force microscope can be used to measure (reaction) forces of a surface. These measurements are called "force spectroscopy" and the result is a force-distance curve for a tested location on the sample surface, see figure 2.6. Applying an appropriate contact-model, one can then derive the stiffness of the tested sample location.

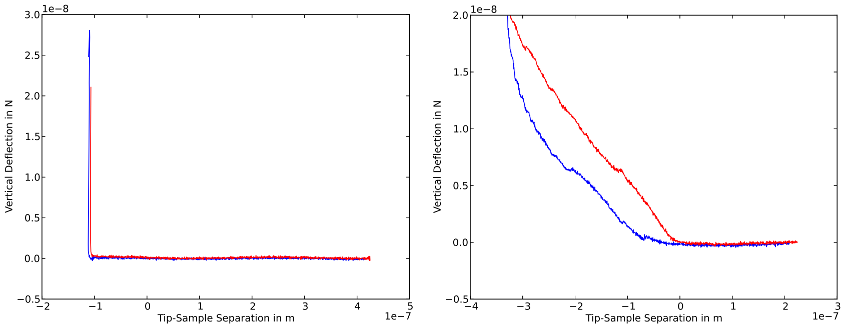

(a) Filter (b) Cell

Figure 2.6: Force-distance curves taken at a location on the filter membrane (a) and on the cell (b). It is clear from figure (a) that the deformation of the cantilever was taken into account (sensitivity): the force increases practically vertically at the contact point, i.e. there is only negligible indentation up until the maximum set-force of $\approx 20\,\mathrm{nN}$. Analysing the curve recorded on top of the cell (b), not only the typical non-linear shape of the force-distance curve is visible, but also the hysteresis behaviour between approach (red) and retract (blue) due to viscous deformation and adhesion. Both curves are smoothed using the standard settings of the AFM device.

2.3.1 Young's Modulus of Saccharomyces Cerevisiae

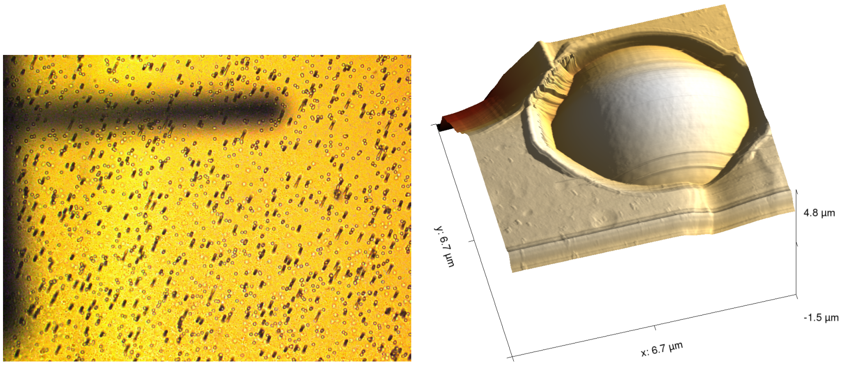

(a) Filter with trapped cells

(b) Relief of trapped, living yeast cell

Figure 2.7: Filter membrane with trapped and free floating yeast cells (a). The shadow of the cantilever and the chip it is attached to is visible on the top and left of the image. (b) 3D view on living yeast cell as measured by AFM. Typical artefacts from the tip-shape are visible at the edge of the hole in which the cell is trapped – as well as single-line artefacts. The surface of both the filter membrane and the cell are very smooth.

An important question for the work described in chapter 3 is: Is there a difference in the Young's modulus (or stiffness) between a genetically modified *Saccharomyces Cerevisiae* yeast strain (JC1) and the wild-type (WT) strain it was derived from? The JC1 strain continuously expresses a gene, $FLO1$, which codes for a protein that resides on the cell wall and drastically enhances adhesion between the yeast cells. This strain is therefore in the following called FLO^+, while the wild-type strain does not under normal circumstances express that gene (flo^-).

To measure the Young's moduli of the respective strains, the protocol described in appendix B.1, inspired by (Alsteens, Dupres, Mc Evoy, et al. 2008; Touhami, Nysten, and Dufrene 2003), was carried out. The results are detailed in appendix B.2.

Summarizing, the yeast cells are trapped in a filter membrane with holes of $\approx 5\,\mu\text{m}$ diameter, matching roughly the size of an average yeast cell, see figure 2.7(a). Using a cell that is mechanically trapped, AFM measurements can be conducted – yielding a view on the surface (figure 2.7(b)) as well as absolute, quantitative stiffness information (see figure 2.8).

From the about 40 measurements collected, due to measurement artefacts, 11 flo^- and 15 FLO^+ datasets could be analysed, yielding average Young's moduli in the

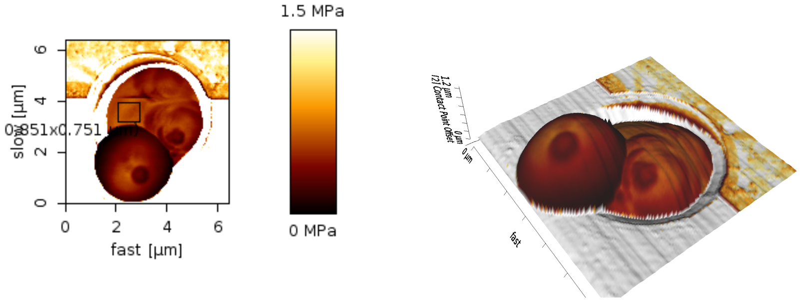

(a) Young's modulus (b) Relief, color Young's modulus

Figure 2.8: 2D (a) and 3D (b) view on apparent Young's modulus of a yeast cell with bud. The filter membrane is "infinitely stiff" compared to the cells (white); Structures of varying stiffness (possibly bud-scars) are clearly visible on the cells. In figure (a), a rectangle is shown from which the average Young's modulus for the cell can be extracted, see description of the method in appendix B.1 and B.2.1.

range of stiffness previously reported in the literature (Alsteens, Dupres, Mc Evoy, et al. 2008; Pelling, Sehati, Gralla, et al. 2004; Touhami, Nysten, and Dufrene 2003), albeit with a wide spread. A detailed analysis of the observational errors can be found in appendix B.2.1. The large range of stiffness data might be explained by the fact that the analysis includes cells of all ages, i.e. cell cycle effects; we cannot exclude the possibility of data for non-viable cells, and the tonicity of the medium could have changed due to uncontrolled evaporation during the experiments. These factors add to the expected biological variability between cells and different cell cultures[3]. It is worth noting, however, that the value reported by Touhami et al. (Touhami, Nysten, and Dufrene 2003), i.e. $600 \pm 400\,\mathrm{kPa}\,(N = 9)$, also shows a large standard deviation which the authors explain in the following way:

> "The rather large standard deviation on the obtained average values reflects variability of the measurements across the surface of the same cell as well as variability associated with independent cell cultures." (Touhami, Nysten, and Dufrene 2003, p. 4543)

The results (table 2.1) clearly show a large variation within each group but no discernible variation between the groups for the statistics collected. This is corroborated by a Kruskal-Wallis one-way analysis of variance by ranks (Kruskal and Wallis 1952) which

---

[3] The same cell culture was used on two subsequent days of measurements, while new cultures were performed by colleagues in the Verstrepen lab for every week in which experiments were performed.

Table 2.1: Summarized results for the Young's modulus of *Saccharomyces Cerevisiae*. Since the total range of the data is large compared to the mean and the statistics is limited, the standard deviation on the mean is of little value. Therefore, the median values with statistical and systematic error estimates are given.

	E flo^- (N=11)	E FLO^+ (N=15)
range	54.7–621.1 kPa	25.7–1080 kPa
mean	221 ± 178 kPa	265 ± 299 kPa
median	167 ± 27 (stat) ± 56 (syst)kPa	116 ± 38 (stat) ± 39 (syst)kPa

reports $p = 0.66 > 0.05$ for the medians of the distributions. In any case, even if the mean stiffness of the two strains were different, the intra-strain differences in stiffness are so big that from a compressive mechanics point of view, the two strains cannot behave significantly different.

2.3.2 Adhesion measurements

Inspired by reports of adhesion measurements in the literature with "cell probes" (Bowen, Lovitt, and Wright 2001; Hinterdorfer and Dufrene 2006), an attempt has been made at directly measuring cell-cell adhesion for yeast cells with the AFM (very interesting work has been done on characterizing the adhesion force of one or several proteins to their counterparts on the yeast surface, e.g. (Lipke, Garcia, Alsteens, et al. 2012), but the integrated cell-cell adhesion may of course depend on additional effects). Despite numerous attempts, no reliable protocol could be established that allowed for repeatable successful probe-preparation and subsequent adhesion measurements (for details see appendix B.3).

The most successful protocol using Polylysene, ε-poly-L-lysine (PLL) (an agent commonly used to increase cell adhesion) to coat the tip-less cantilever yielded the force curves shown in figure 2.9. The repeatability of the protocol is insufficient for measurements with larger statistics, and there are some doubts about the binding strength provided by the PLL: The experiment relies on the fact that the adhesion or binding of the cell to the cantilever is much stronger than the cell-cell adhesion that is to be measured, since the deformation upon retraction would otherwise be modified by the potential of that binding. Since the binding of a cell to the PLL coated cantilever only worked spuriously, it is difficult to assess this binding strength.

A force-distance curve has been recorded every second and the movement did not pause when the cells were in contact, since the instantaneous adhesion has been the measure of interest. In figure 2.9(b) and figure 2.9(d) data are shown in which very strong adhesion has been found as indicated by the blue shaded area in the retraction curve. The extracted adhesion energies E_{adh} are reported directly in the figure captions. To calculate the total work of adhesion per area W, the Hertz contact area for the "average" yeast cell ($E = 250\,\text{kPa}$, $\nu = 0.4$, $R_{\text{Cell}} = 2.5\,\mu\text{m}$) under the the maximal compressive force of 5 nN was assumed. This leads to maximal values of W of $W \approx 8 \times 10^{-4}\,\text{J}/\text{m}^2$. In most of the recorded curves (similar to 2.9(a) and 2.9(c)) in the same experiment, the work of adhesion is found to be $W \approx 1 \times 10^{-4}\,\text{J}/\text{m}^2$.

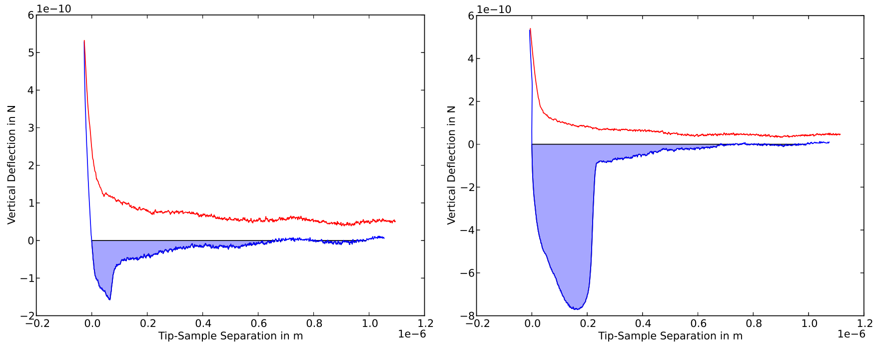

(a) $t = 0\,\text{s}$, $E_{\text{adh}} = 2.25 \times 10^{-17}\,\text{J}$ (b) $t = 1\,\text{s}$, $E_{\text{adh}} = 1.55 \times 10^{-16}\,\text{J}$

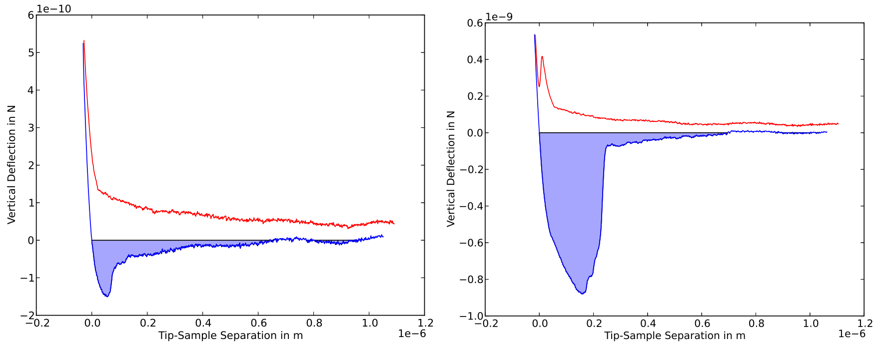

(c) $t = 4\,\text{s}$, $E_{\text{adh}} = 2.35 \times 10^{-17}\,\text{J}$ (d) $t = 7\,\text{s}$, $E_{\text{adh}} = 1.74 \times 10^{-16}\,\text{J}$

Figure 2.9: Force-distance curves showing adhesion between two FLO^{+} yeast cells. Both approach (red) and retract (blue) curves are shown; the blue area corresponds to the reported adhesion energy E_{adh}.

It is very difficult to interpret these results, especially as they could not be reproduced. It is conceivable that as the force curves shown in figures 2.9(b) and 2.9(d) have been recorded, the "cell probe" did not make direct contact with the trapped cell in the membrane, but that the PLL-coated cantilever itself came into direct contact with it.

In this case, those two large adhesion energies would represent the adhesion of the specific trapped cell with the PLL-coated silicon of the cantilever rather than cell-cell adhesion.

2.4 Summary and conclusions on the measurements performed

Several interesting techniques are available to investigate mechanics at the cellular scale. Three basic ones have been discussed in detail: Micropipette Aspiration, Optical Tweezers and Atomic Force Microscopy. Measurements have been carried out using MA to show its validity, and support and supervision have been supplied for a master thesis project establishing the technique for our group at KU Leuven. Furthermore, it has been made clear that MA is not suitable to elucidate mechanical properties of cells with a stiff cell wall such as yeast.

Optical Tweezers allow for high-precision experiments on very low scales; OT measurements described in the literature are being used to validate RBC mechanics in chapter 4.

Different types of measurements have been undertaken with the AFM device. Next to obtaining high-resolution, three-dimensional images of the surface of yeast trapped in a micro-filter membrane, also mechanical parameters have been measured. It could be shown that it is possible to measure cell-cell adhesion with an AFM device, although further optimization of the experimental protocol is required to obtain more robust and extensive data.

Finally, (force-mapping) indentation experiments have been performed on *Saccharomyces Cerevisiae* to extract Young's moduli of the cell wall of living yeast cells. The results show that there are no mechanically important differences between the cell wall stiffness of the two tested strains (a wild-type flo^- and a genetically modified FLO^+ strain). This means that despite the surface proteins which strongly affect adhesion forces, FLO^+ cells behave as flo^- cells when compressed.

Chapter 3

Yeast cell sorting and evolutionary implications

> Artikel 1: Et es wie et es.
> Artikel 2: Et kütt wie et kütt.
> Artikel 3: Et hätt noch emmer joot jejange.
>
> Rheinisches Grundgesetz,
> zitiert nach Konrad Beikircher

Introduction

In order to prove the capability of the developed software to construct and run a meaningful individual cell-based model, a valuable test-case in a genetics problem in yeast is considered. While this has been carried out in close collaboration with a co-worker (Smeets 2010) as well as a number of other people (Odenthal, Smeets, Christiaens, et al. 2012), the main part of the work has been undertaken in the framework of this thesis, contributing to the model building, the software design and implementation aspects as well as running simulations and producing figures.

The system of two growing yeast strains constitutes a prime example of how the individual-cell based modelling platform can be applied, since one strives to explain a dynamic biological phenomenon purely from a mechanical point of view. In the following, the (classical) individual cell-based model will be explained.

A novelty compared to models described in the literature is the budding mechanism which was needed to describe the "budding yeast" used in the corresponding experiments. Additionally, the methods developed to measure cell-sorting, especially the "compaction" parameter might be of more general interest. It will be shown that it is possible to construct a physically sound cell mechanical model supplemented with a morphological model for cell growth and division, which explains the experimentally observed cell sorting in this system. Thereby the hypothesis is corroborated that this mechanism increases cooperation between cells expressing the adhesion-genes, which makes this system a prime example of a "green beard gene", an interesting example of the evolution of cooperation.

In budding yeast *Saccharomyces Cerevisiae*, the expression of FLO genes[1] has been identified as a cause of flocculation in colonies. For yeast, flocculation is a protection mechanism in stress conditions. Cells expressing the $FLO1$ gene preferably stick to other cells that also express this gene. Since they adhere more strongly, $FLO1^+$ cells aggregate to the centre of the flock, where they are physically shielded against toxins in the medium, including ethanol and antimicrobials. From a socio-evolutionary viewpoint, $FLO1$ can be considered a "green beard gene", which promotes cooperation between individuals that express this gene (Dawkins 1976, p. 89). It is known that the FLO genes code a number of surface proteins influencing inter-cellular interactions. The following work substantiates the hypothesis (Smukalla, Caldara, Pochet, et al. 2008) that the "kin-recognition" mechanism relies solely on the fact that cells expressing the $FLO1$-protein adhere more strongly to other cells expressing the protein than to cells which do not express it.

To investigate the flocculation behaviour of yeast cells in solution *in silico*, a mathematical model is constructed which is as simple as possible while completely capturing the flocculation dynamics.

3.1 Yeast sorting model structure

The cell shape is approximated to be spherical, since the shape of yeast cells in solution deviates only slightly from spheres. A true, mesh-free IBM which avoids artefacts in

---

[1] The FLO genes are a family of genes linked to flocculation behaviour (hence the name). Their expression is dynamically switched in wild-type yeast, in which they are typically not expressed in non-stress conditions (flo^-), whereas they can be genetically modified to be always expressed (JC1-strain, FLO^+).

the number of possible contacts a cell can have is chosen, since these direct contacts with a cell's next neighbours strongly influence the dynamics of the system.

To model the "kin-recognition" process, it is crucial to capture the movements of the cells with sufficient precision to resolve the dynamics of single contact-events.

The IBM for cell expansion was implemented by extending the DEMeter++ framework (Geris, Liedekerke, Smeets, et al. 2009; Tijskens, Ramon, and De Baerdemaeker 2003). Cells are considered as particles that interact by physical forces. At each time-step, the forces are integrated for each particle, its resulting velocity is calculated and the cell positions are updated using an explicit Euler integrator.

3.1.1 Equation of motion

Central to the individual-based model is the equation of motion. Since yeast lives in a low Reynolds number environment, their inertia can be neglected. Therefore a first-order equation of motion for each cell i is obtained that needs to be solved for the velocity, similar to (Drasdo, Hoehme, and Block 2007; Hoehme and Drasdo 2005):

$$\sum_{j\in\mathcal{N}} \mathbf{F}_{ij} + \mathbf{F}_{i,\text{budding}} + \mathbf{F}_{i,\text{Brownian}} = \Gamma_{iw}\mathbf{v}_i + \sum_{j\in\mathcal{N}} \Gamma_{ij}(\mathbf{v}_i - \mathbf{v}_j), \tag{3.1}$$

with at the left hand side the conservative mechanical forces $\mathbf{F}$ between cell i and its neighbours $j \in \mathcal{N}$, the biological force of cell division (budding) and a force representing Brownian motion (a derivation of the magnitude of this random force term is given in appendix C). The viscous, velocity ($\mathbf{v}$) dependent terms are at the right hand side of this equation: the viscous drag force due to suspension in liquid (with the dynamic viscosity η), $\Gamma_{iw} = 6\pi\eta\, r_i$ and the cell-cell friction forces between cell i and its contacting cells $\Gamma_{ij} = \gamma_n \hat{\mathbf{n}}\hat{\mathbf{n}}^{\mathrm{T}} + \gamma_t \left(\mathbf{I} - \hat{\mathbf{n}}\hat{\mathbf{n}}^{\mathrm{T}}\right)$, where $\hat{\mathbf{n}}$ is the normalised direction vector between the two cells and γ_n, γ_t are, respectively, the normal and tangential friction constants.

The Conjugate Gradient (CG) method is used to obtain a coupled solution for the velocities, since the friction matrix Γ is positive-definite, see appendix D. Next, a forward Euler scheme updates the cell positions as $\mathbf{x}_i(t+\mathrm{d}t) = \mathbf{x}_i(t) + \mathbf{v}_i(t)\cdot \mathrm{d}t$.

3.1.2 Contact Mechanics

The crucial step in "kin-recognition" happens when two yeast cells come into close contact. There are abundant models in the literature to capture the potential between two cells in close contact, see e.g. (Chu, Dufour, Thiery, et al. 2005; Drasdo, Hoehme, and Block 2007; Hertz 1881; Johnson, Kendall, and Roberts 1971; Pathmanathan, Cooper, Fletcher, et al. 2009). The simplest would be a harmonic potential, i.e. a linear spring which is at rest for a non-zero apparent overlap δ of the cells. Hertz showed that the repulsive forces between solid, elastic bodies are actually non-linear. This repulsive potential can be modified to take adhesion forces into account. In chapter 4, section 4.1.1 a more general theory (Maugis-Dugdale) for contact forces between adhesive, elastic bodies is explained. That theory captures the full range between the Derjaguin-Muller-Toporov (DMT) zone of comparatively long reaching adhesive forces and small adhesive deformations to the Johnson-Kendall-Roberts (JKR) limit of short interaction ranges and comparatively large adhesive deformations in the transition parameter λ[2]:

$$\lambda = \sigma_0 \left(\frac{9\hat{R}}{2\pi W \hat{E}^2} \right)^{1/3}. \tag{3.2}$$

In equation 3.2, σ_0 is the maximum adhesive tension (measured in Pa) from a Lennard-Jones potential, W (in J/m^2) the adhesion energy, $\hat{R}$ is the reduced radius of the contact of the cells and $\hat{E}$ their combined elastic modulus:

$$\hat{E} = \left(\frac{1-\nu_i^2}{E_i} + \frac{1-\nu_j^2}{E_j} \right)^{-1} \text{ and } \hat{R} = \left(\frac{1}{R_i} + \frac{1}{R_j} \right)^{-1} \tag{3.3}$$

with E_i and E_j being the Young's moduli, ν_i and ν_j the Poisson numbers and R_i and R_j the radii of cells i and j, respectively.

Filling in the values (see table 3.1) and assuming the Maugis-Dugdale approximation for

$$\sigma_0 = W/h_0,$$

with an effective range of adhesive interaction h_0 of 2×10^{-8} m (Israelachvili 2011), one arrives at $\lambda \approx 0.09$, yielding a value for which the DMT approximation holds (Johnson and Greenwood 1997, Figure 5)(for more details see also section 4.1.1).

For this case, when the adhesion itself causes relatively low deformations, it is assumed that the energy released by "binding" of adhesion-molecules is constant, and that those molecules are relatively evenly distributed. Then, the total energy released by the contact is proportional to the area of contact, thus yielding for the modified Hertz-potential:

$$V(\delta) = -\frac{8\hat{E}\sqrt{\hat{R}}}{15}\delta^{5/2} + \pi W \hat{R} \delta. \tag{3.4}$$

In equation (3.4), W is defined as "surface energy per unit area" and is therefore the measure for cell adhesion. It can also be very approximately interpreted as average

---

[2] The transition parameter λ relates to the "Tabor coefficient" by a factor of 1.16 (Johnson and Greenwood 1997).

number of adhesion-molecules per area multiplied with their respective adhesion-energy.

Interestingly, the adhesive part of the interaction-force due to this model for cell-cell contact does not directly depend on the overlap:

$$F(\delta) = -\frac{4\hat{E}\sqrt{\hat{R}}}{3}\delta^{3/2} + \pi W \hat{R} \tag{3.5}$$

3.1.3 Budding and Growth

It is assumed that the proliferating yeast cells are in the exponential growth phase. Because the intracellular biology of the cell cycle is not required to test the sorting hypothesis, only the changes of cell shape during the cell cycle have to be taken into account, as they will influence the cellular interaction forces. Morphologically, the cell cycle can be subdivided into two important stages: cellular growth and cytokinesis. According to (Qu, Weiss, and MacLellan 2004), cellular growth can be described by:

$$\frac{dm}{dt} = K[R]A_o, \tag{3.6}$$

in which the rate of mass change in time (dm/dt) is proportional to the outer surface area of the cell just after division (A_o) and the total ribosome content, which is assumed to remain constant[3].

Cells of *S. Cerevisiae* divide by budding. The daughter cell appears as a small bulge from the cell wall of the mother cell, and steadily grows while still attached until it separates from the mother cell. Analogous to how binary fission can be described by two overlapping spheres with changing distance and radius ((Drasdo, Hoehme, and Block 2007; Drasdo, Kree, and McCaskill 1995)), the budding mechanism is geometrically approximated by a combination of two spheres, see also (Smeets 2010) for mathematical description. During the budding process, the increase in volume over time of the mother-bud complex is assumed to remain constant. The average time for the budding process to complete is a model parameter. Then, the appropriate bud radius

---

[3] The growth rate is not necessarily constant in time for many cell types. For example, (Fingar, Salama, Tsou, et al. 2002) report a three-fold change in growth rate during the growth of a single cell. However, the precise dynamics of the growth rate is not well understood, and it can be shown that the difference in the dynamics of the cell size when using a non-constant growth rate with the same final size is very small.

Consider a worst case scenario for a monotonously increasing growth rate change (as reported by (Fingar, Salama, Tsou, et al. 2002)). This would be a step function that increases from a minimal low value to a maximal high value at $t = 1/2T_g$, T_g being the total growth-time until division. The maximal error in cell radius would occur at $t = 1/2T_g$. For the yeast cells considered, a simple calculation shows that this error would be smaller than 4 % if the step function shows a threefold increase in growth rate. In fact, the approximation of a cell as a (deformable) sphere will introduce a larger error for the space taken up by the cells.

r and displacement d can be calculated assuming a linear growth of the displacement over time. Figure 3.1 shows how two overlapping spheres are connected to approximate the shape of budding cells.

At this point the experimentally observed variation in final cell size is introduced as well: A normally-distributed random variable δ_{div} is added to the final size of the newly budded yeast cell.

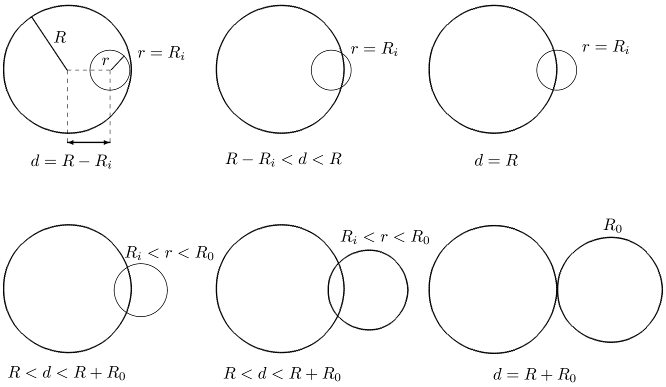

Figure 3.1: Approximation of a budding cell by two overlapping spheres. Initially, the minor sphere (bud) has a predetermined radius R_i and is completely inside the mother cell. The displacement d increases until $r = R_i$. Next, both radius and displacement increase until the bud separates from the mother cell when $r = R_o$.

Mechanical inhibition of cell division is modelled by including a division force F_d. Biologically, this force arises from the assembly of cytoskeleton and polysaccharides in the cell wall. The magnitude of F_d is dependent on the mechanical environment: a higher force is required when the cell is closely surrounded by other cells than when the cell is freely suspended in liquid. In the model F_d is adjusted dynamically in order to complete division in the prescribed time. Furthermore, a maximum value for F_d is set which corresponds with the threshold for mechanical inhibition.

3.1.4 Model parameters

The model parameters used for the simulations are listed in table 3.1. This set represents the standard conditions for a growing colony starting with both one FLO^+ and one flo^- cell.

Table 3.1: Base parameter set for the individual-based model investigating yeast sorting. The values have been estimated from various sources: [1](Smeets 2010), [2](taken "high enough" to lead to exponential growth), [3](Smukalla, Caldara, Pochet, et al. 2008), [4](Touhami, Hoffmann, Vasella, et al. 2003), [5](Galle, Loeffler, and Drasdo 2005).

Parameter	Symbol	Value	Units	Estimated from
time step	Δt	$0.5 \cdot 10^{-3}$	s	trial simulations
simulation time	T_{end}	$65 \cdot 10^{3}$	s	trial simulations
CG precision	e_{max}	$10 \cdot 10^{-12}$	N	trial simulations
division size	R_0	$2.5 \cdot 10^{-6}$	m	microscopy, [1]
division size sdev	δ_{div}	$0.1 \cdot 10^{-6}$	m	microscopy, [1]
division force threshold	$F_{d,max}$	$0.5 \cdot 10^{-9}$	N	trial simulations [2]
division time	T_d	$3.6 \cdot 10^{3}$	s	[3]
growth time	T_g	$7.2 \cdot 10^{3}$	s	[3]
adhesion FLO^+-FLO^+	W_{++}	$8 \cdot 10^{-6}$	$\mathrm{J/m^2}$	[4]
adhesion FLO^+-flo^-	W_{+-}	$4.5 \cdot 10^{-6}$	$\mathrm{J/m^2}$	assumed
adhesion flo^--flo^-	W_{--}	$1 \cdot 10^{-6}$	$\mathrm{J/m^2}$	assumed
Young's modulus	E_c	1600	Pa	assumed, see text
Poisson's ratio	ν_c	0.4		assumed, range [5]
tangential friction coef.	γ_t	$0.06 \cdot 10^{-6}$	kg/s	assumed, range [5]
normal friction coef.	γ_n	$0.2 \cdot 10^{-6}$	kg/s	assumed, range [5]
temperature	T	310	K	typical experiment
viscosity	η	$0.7 \cdot 10^{-3}$	Pa s	water @ T

3.2 Measuring yeast cell sorting

There are several ways to measure how "well sorted" the system consisting of the two adhesion phenotypes FLO^+ and flo^- is at all times during a simulation. This is a non-trivial problem because the overall shape of the flocks can be highly irregular.

3.2.1 Centres of mass

The easiest is to compare the centres of mass for the different constituents: defining

$$\varepsilon = \left| \sum_{i=0}^{N_{flo^-}} \frac{m_i \mathbf{x}_i}{M_{flo^-}} - \sum_{i=0}^{N_{FLO^+}} \frac{m_i \mathbf{x}_i}{M_{FLO^+}} \right| / \sqrt[3]{Vol_{total} \cdot \frac{3}{4\pi}}, \tag{3.7}$$

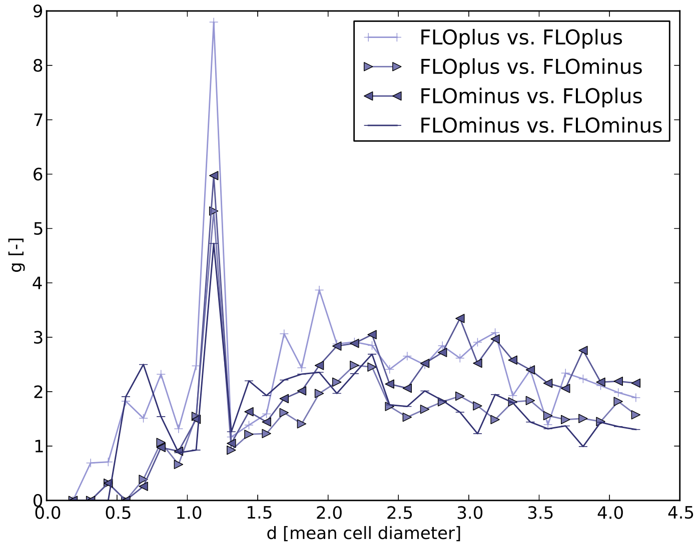

Figure 3.2: Radial distribution function of yeast strains at $t \approx 18\,\mathrm{h}$ for a simulation with Young's modulus $E = 6.4\,\mathrm{kPa}$.

which is normalized with the theoretical minimum radius of a cell-mass with the same volume for better comparison (see figure 3.4 (e)). For an ideally sorted and spherical flock, ε approaches zero. A problem of this method is, that ε becomes zero for completely randomly mixed flocks as well.

3.2.2 Radial distribution function

Another generic description of particle distribution in such a system that is often used, is the radial distribution function (also called pair-correlation or two-point correlation function). This approach entails two problems: The statistics are even at the end of the simulation not very good, and the normalization is questionable, since the algorithm employed uses the smallest rectangular box aligned with the global coordinate system into which the whole colony fits. This leads to results comparable to figure 3.2, but both problems make it impossible to compare more than the first peaks of different realizations of the system. Therefore, it is preferable to directly compare the average coordination numbers of the constituents for which the first peak of the radial distribution function is indicative:

3.2.3 Coordination number

The average coordination number can be calculated by counting how many other cells a given cell has contact with – here the contact is defined as being closer than 102 % of the added radii of the cells. The precise number does not influence the outcome (see figure 3.4 (a) - (d)). Contacts between a $FLO1$ expressing cells (FLO^+) and non-expressing cells (flo^-) as well as the mixed contacts can be distinguished. The coordination number has a comparatively low "resolution" in the sense that small changes in cell density may be missed by only comparing this value.

3.2.4 Cluster analysis & compaction

Regarding simulations with a very low adhesion strength (e.g. 3.5(a), 3.6(a)) for the flo^- strain, it is worthwhile to do a cluster analysis, and compare the number and sizes of cell clusters for the two cases. A typical procedure would be to define a distance function for cells i and j as

$$s_{ij} = \frac{\left|\mathbf{x}_i - \mathbf{x}_j\right|}{R_i + R_j}. \tag{3.8}$$

Note that $s_{ij} \leq 1$ for all cells defined to be in contact and larger for other cells, and it is proportional to the distance of their centres.
Using a hierarchical clustering scheme as described by e.g. (S. C. Johnson 1967)[4], one can therefore easily find all clusters of adhering cells in either the combined flock, or the individual FLO^+, flo^- constituents. The higher the number of clusters is, and the smaller the cluster size is, the less well-protected these yeast cells obviously are. Unfortunately, as one increases the adhesion energy of the flo^- cells, all cells will generally stay together in one large cluster, and therefore the measure is less useful in these cases. It should be kept in mind, though, that using this method, one can always easily define the "main" flock to be used for further analysis, the only downside being the rather considerable computational cost.

To obtain a completely shape-independent measure for cell compaction (or density), the following procedure has been devised: It is possible to construct the "convex hull" (Chazelle 1993) of a flock (or one of its constituents) which is a convex polyhedron with triangular faces in three dimensions[5]. Comparing the volume V_{Hull} of said polyhedron with the volume of the cells it contains, one can compute a shape independent measure

---

[4] The hierarchical clustering scheme used has been provided by the python package "cluster", which cites (Matteo n.d.), which in turn refers to the reference given.

[5] A python module built on top of the "qhull" library has been used (Barber, Dobkin, and Huhdanpaa 1996).

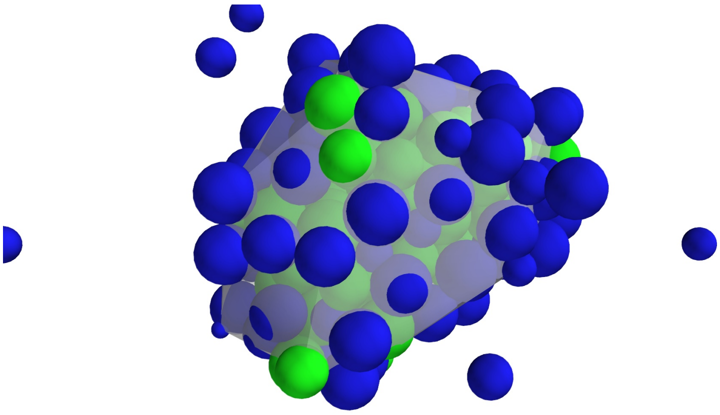

Figure 3.3: Convex hull (transparent plains) as constructed for simulation of yeast strains at $t \approx 18\,\mathrm{h}$, $W_{++}/W_{--} = \mathrm{inf}$. The algorithm works on the cells' centres.

for "how compact" the flock is (figure 3.3):

$$c_x = \frac{\sum_{i \in x} \frac{4}{3}\pi R_i^3}{V_{\mathrm{Hull},x}}, x \in \left\{FLO^+, flo^-, \text{complete flock}\right\}. \tag{3.9}$$

To compare the two constituents of the flock, this measure is normalised with the overall compaction of the combined flock:

$$\hat{c}_y = \frac{c_y}{c_{\text{complete flock}}}, y \in \left\{FLO^+, flo^-\right\}. \tag{3.10}$$

Calculating this measure is very expensive, so it was used only as an end-point analysis (see section 3.3.2), but it proved very stable; the standard deviation of c_x in the last 5 min of simulated time was always below 0.1 %, and is therefore not given for each specific value.

3.3 Results and Discussion of yeast sorting simulations

3.3.1 Natural Young's Modulus of yeast

It is not currently feasible to simulate how yeast grows and sorts with the natural Young's modulus of the cells because the time-step would have to be prohibitively low[6], therefore the influence of stiffness on sorting behaviour is analysed. The results (see figure 3.4 (a) - (e)) show that increased stiffness leads to better sorting[7], but that the differences become negligible in the kPa range. The differences between 1.6 kPa to 6.4 kPa Young's modulus are comparable to the differences of two simulations with the same Young's modulus and a different random seed. The figures 3.4(a)-3.4(d) show averages over six different realisations of the simulation. The measures used for the comparison are explained in depth in section 3.2: Comparing the average coordination numbers, i.e. how many other cells of a given phenotype a cell is in contact with, and for a simpler measure the centres of mass of the different phenotypes.

3.3.2 Sorting by adhesion strength

In absence of reliable measurements of adhesion strength incurred by the expression or non-expression of the $FLO1$ protein (see section 2.3.2), several absolute and relative adhesion strengths for both types were simulated. Strongest sorting as well as most dissociated flo^- cells were found, if the flo^- strain had an adhesion energy $W_{--} = 0\,\mathrm{J/m^2}$ (figure 3.6(a)). The adhesion energy between the two different types was set to $W_{+-} = \frac{W_{++}+W_{--}}{2}$, since the $FLO1$ proteins not only adhere to each other, but also to other cell wall proteins.

The results shown in figures 3.5, 3.6 indicate that sorting still occurs for differences in adhesion strength W_{++} vs. W_{--} as small as two-fold. While there is obviously no strict limit indicating a "too small" difference in adhesion strength for sorting to occur, the compaction numbers (see equation 3.10) given in the figure clearly indicate that in all simulations the FLO^+ cells are more "compact" and therefore better protected than the flo^- cells. The compaction reached by the cells in the simulations depends also on the given realization of an "*in silico*" experiment. Therefore, the difference in compaction reported in figure 3.6(d) may be too small to reliably indicate a sorted flock – in a way this figure exemplifies, what a non-sorted flock would look like.

3.4 Conclusions on the application of an IBM to yeast sorting

The individual-cell based model has been specialized for the case of budding yeast, in which motion is caused by Brownian agitation and movement due to budding. The

---

[6] estimated time for one simulation to complete: 190 days

[7] Better sorting at higher stiffness may seem somewhat contrary to the finding reported by (Palsson 2008). In that case, though, a "low" stiffness leads to substantial changes in aspect-ratio of the *dictyostelium* cells, thereby changing the basic geometrical conditions, whereas yeast cells remain rounded in all physiological situations investigated.

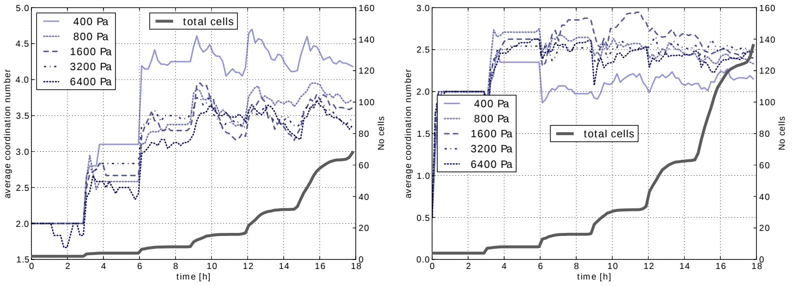

(a) $flo^{-} - flo^{-}$ (b) $flo^{-} - FLO^{+}$

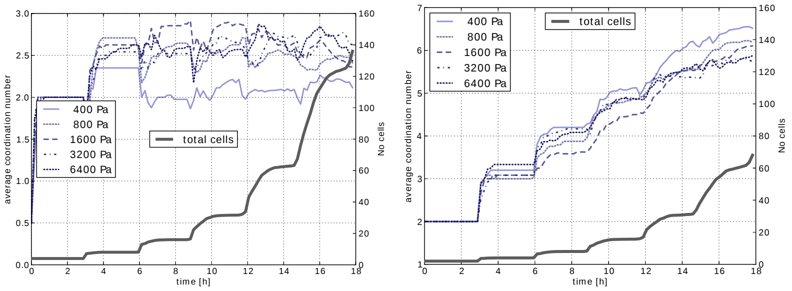

(c) $FLO^{+} - flo^{-}$ (d) $FLO^{+} - FLO^{+}$

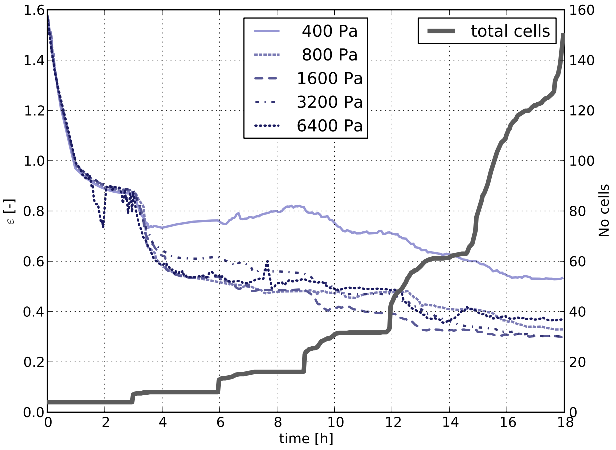

(e) Centre-of-mass comparison

Figure 3.4: Average coordination numbers (see section 3.2) and the centre-of-mass comparison show that stiffness does not significantly influence sorting above ca. 1.6 kPa. Plots are averages over six different sets of random numbers.

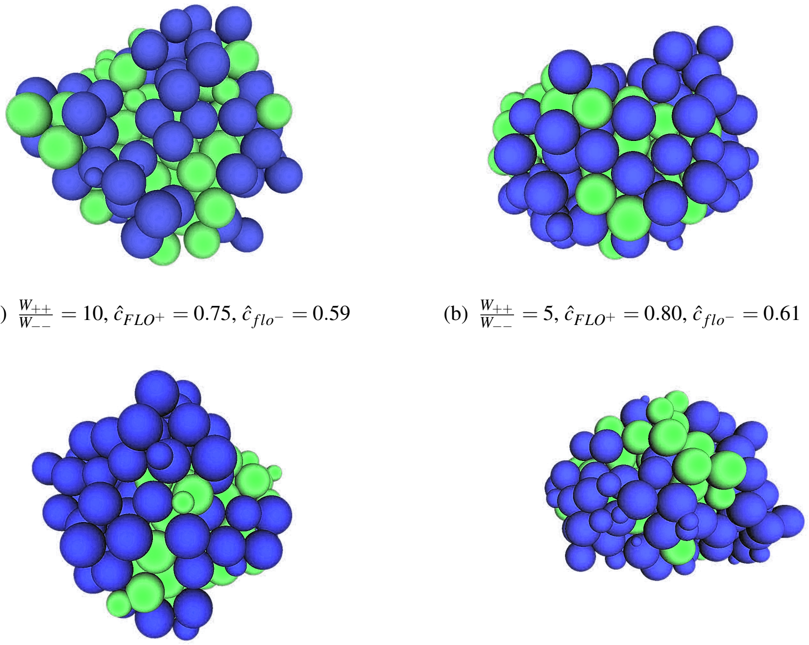

(a) $\frac{W_{++}}{W_{--}} = 10$, $\hat{c}_{FLO^+} = 0.75$, $\hat{c}_{flo^-} = 0.59$

(b) $\frac{W_{++}}{W_{--}} = 5$, $\hat{c}_{FLO^+} = 0.80$, $\hat{c}_{flo^-} = 0.61$

(c) $\frac{W_{++}}{W_{--}} = 3.3$, $\hat{c}_{FLO^+} = 0.85$, $\hat{c}_{flo^-} = 0.65$

(d) $\frac{W_{++}}{W_{--}} = 2.5$, $\hat{c}_{FLO^+} = 1.04$, $\hat{c}_{flo^-} = 0.63$

Figure 3.5: Typical representations of sorted flocks at $t \approx 18\,\text{h}$. Green cells represent the FLO^+, blue cells the flo^- phenotype. The adhesion energy between the FLO^+ cells is $W_{++} = 10 \times 10^{-6}\,\text{J//m}^2$ and the value of adhesion W_{--} changes according to the given relations. Most of the micro-flocks are well sorted according to their phenotype, as evidenced by the given “compaction” numbers $\hat{c}$.

mixed flocks consisting of a FLO^+ and a flo^- strain generally evolve in a way that (some) of the FLO^+ cells are better protected against environmental stresses by being tightly packed in other cells of both genetic make-ups. This “sorting” of the flock provides an advantage to the FLO^+ strain, since the protected cells are more likely to sustain periods of high doses of environmental toxins.

The stiffness (above a certain limit) of yeast-yeast contact (E) has been predicted to be of no importance for the sorting in the simulations, which has been corroborated by the AFM measurements (chapter 2), in which the Young’s modulus has been found to be the same for both strains.

The hypothesis that the $FLO1$ gene is recognized simply by the mechanical parameter

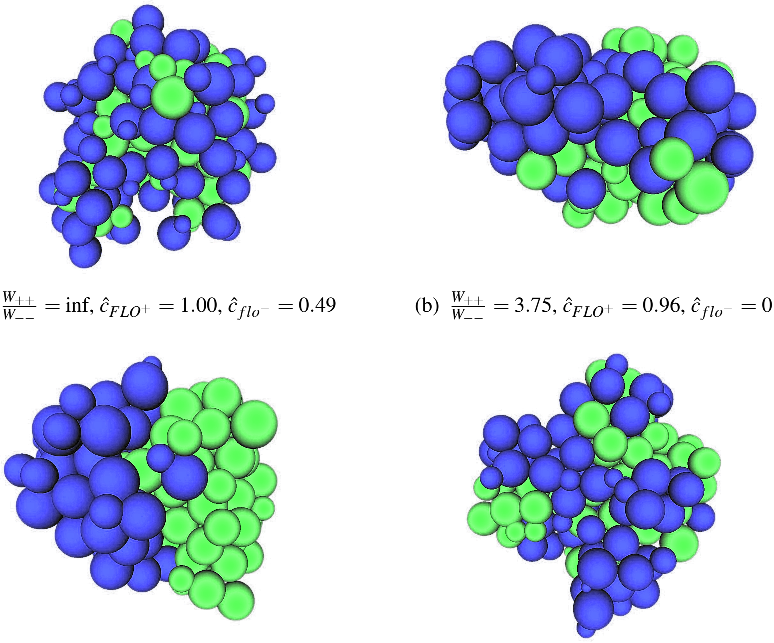

(a) $\frac{W_{++}}{W_{--}} = \mathrm{inf}$, $\hat{c}_{FLO^+} = 1.00$, $\hat{c}_{flo^-} = 0.49$

(b) $\frac{W_{++}}{W_{--}} = 3.75$, $\hat{c}_{FLO^+} = 0.96$, $\hat{c}_{flo^-} = 0.68$

(c) $\frac{W_{++}}{W_{--}} = 1.875$, $\hat{c}_{FLO^+} = 1.13$, $\hat{c}_{flo^-} = 0.87$

(d) $\frac{W_{++}}{W_{--}} = 1.5$, $\hat{c}_{FLO^+} = 0.71$, $\hat{c}_{flo^-} = 0.65$

Figure 3.6: Typical representations of sorted flocks at $t \approx 18\,\mathrm{h}$. Green cells represent the FLO^+, blue cells the flo^- phenotype. The adhesion energy between the FLO^+ cells is $W_{++} = 7.5 \times 10^{-6}\,\mathrm{J//m^2}$. While the first three microflocks are well sorted according to their phenotype, as evidenced by the given “compaction” numbers $\hat{c}$, the flock shown in sub-figure (d) does not look sorted, and, indeed, the difference in compaction numbers is very low.

of adhesion strength W by other cells also expressing $FLO1$ has been significantly substantiated. Sorting occurs even for comparatively small differences in adhesion strength.

This is an interesting case of a “green beard gene”, which has both the function of recognizing a (likely) copy of itself in another organism as well as showing altruism towards it. Thus, a “green beard gene” is one of the most basic ways of how “selfish” genes (Dawkins 1976) can lead to cooperation between their carrying organisms. In addition to the preferential sorting due to differential adhesion, the two groups of cells segregate naturally due to their initial growth patterns: As is obvious in e.g. figure 3.6(c), the flo^- cells will mostly bud in an environment with flo^- cells, and the FLO^+ yeast will divide mostly in an environment with other FLO^+ cells. This aspect of spatial segregation, which is reinforcing (or reinforced by) the differential adhesion sorting, has been elucidated in the literature by e.g. (Nadell, Foster, and Xavier 2010).

The hypothesis of sorting due to adhesion, Brownian motion and local growth showcases the strengths of a classical IBM: A well-defined set of minimal biomechanical assumptions can describe a system which evolves in a non-obvious way towards comparative order. Due to the simplicity and perfect control of the model, insight is therefore gained into the mechanisms driving the considerably more complicated and less controlled *in vitro* system.

Chapter 4

A deformable cell model for IBM

> Doe wat je hand te doen vindt.
> Doe het met volle inzet, want
> er zijn geen daden en gedachten,
> geen kennis en geen wijsheid in het dodenrijk.
> [. . .]
>
> Prediker, 9:10

Introduction

To deal with softer cells without a cell wall, IBMs face the difficulty of taking cell shape into account. In the following, a mathematical model which is able to deal with arbitrary shapes and deformation of the cell is constructed and explained.

The focus is set on the seemingly simple problem of initial cell spreading to show the usefulness and applicability of the detailed mechanistic cell model. It has been shown before that many cell types display very similar early spreading (i.e. “touch-down” and adhesion to a flat substrate). This observation has been linked to the mechanical nature of the phenomenon, during which a cell cannot yet react by changing its structure and behaviour. Understanding in detail how this passive spreading occurs – and to what clues a cell may later respond – is the goal of this work. At the same time, the model developed here is expected to be very valuable for more complex situations of interacting cells, since it is able to reproduce the purely mechanical response in detail. Finally, a view on possible extensions of the model for cells with a (discrete) cytoskeleton is presented.

This very novel work has been carried out within a close collaboration; as indicated in the publication on which this chapter is based, the two first authors contributed equally to the conception of the model, its implementation and the analysis of the results (Odenthal, Smeets, Van Liedekerke, et al. 2013). While model development and implementation progressed quite quickly due to previous experience with IBMs, several major challenges had nevertheless to be overcome: Especially making the model results independent of the chosen mesh proved quite difficult and lead to the inclusion of the numerical integration scheme using quadrature rules. Smaller “breakthroughs” were achieved by using the proper FENE potential instead of a linear spring for the coarse-grained spectrin network and by not only taking normal forces but also the actual moments due to the contact potential into account.

The dynamics of initial cell spreading – that is during the first few minutes – are governed by energy release through binding events of cell surface molecules, rather than by active cellular processes such as e.g. tension generated by stress fibres. These molecular binding events dominate the total adhesion energy of the cell. This adhesion creates a pulling effect that in turn generates strong local forces which result in deformations of the actin cortex. The dynamics of initial cell spreading (the increase of radius of the contact area with time t) universally correspond to an early ($\sim t^{1/2}$), and a later ($\sim t^{1/4}$) power law behaviour (Cuvelier, Thery, Chu, et al. 2007). It is only at an advanced stage when the cell is already moderately spread out that active pulling of actin stress fibres on focal adhesion complexes will reinforce cell spreading, depending on the cell type in question, see e.g. (Huveneers and Danen 2009).

The viscoelastic behaviour of the cell boundary is determined not so much by the cell membrane itself, but by the intracellular cytoskeleton, or, in the case of red blood cells (RBCs), a network of spectrin filaments directly underlying the membrane (Fedosov, Caswell, and Karniadakis 2010; Fedosov, Lei, Caswell, et al. 2011).

A model that can be used for describing cellular mechanics should be able to accurately describe the mechanical interactions that take place at the cell boundary, i.e. the contact interface with its substrate, the extracellular matrix or surrounding cells. Lattice-free, particle-based methods can describe the interaction forces and the resulting movement and deformation of particles in a natural way. At a point of contact between two particles, contact forces are calculated explicitly based on an appropriate contact force model. From these forces, movement of the particles is calculated by integrating the equation of motion. In the simplest approach, particles are assumed to be spherical. In that case, contact forces can be directly calculated from the sphere-sphere overlap distance $\delta = r_1 + r_2 - \|\mathbf{x}_1 - \mathbf{x}_2\|$ ($r_{1,2}$ are the radii of the spheres and $\mathbf{x}_{1,2}$ the spacial coordinates of their centres). Calculating contact forces for non-spherical shapes is more challenging: approximations have to be made for the contact force model and it is not trivial to calculate a meaningful overlap distance for all cases. Arbitrary shapes have been modelled by using combinations of connected overlapping spheres (Lu and McDowell 2007), or by using polyhedra or poly-arcs and calculating a contact force proportional to the overlapping volume of the shapes (Matuttis, Luding, and Herrman 2000; Pöschel and Schwager 2005). Besides, the surface of an arbitrary shape can be approximated by sampling points (Spillmann and Teschner 2005). For each sampling point, a contact force can be calculated based on the indentation in the surface of another object. Disadvantages of using sampling points include the fact that it is hard to directly compare it to a physical contact model such as the Hertz model for spheres, that they generally do not allow to reach complete force equilibrium, and that the precision of the approximation of the contact depends crucially on the local density of nodes, so that the contact parameters need to be re-scaled for different node densities (Spillmann and Teschner 2005).

We present a novel computational framework for describing the mechanical behaviour of cells with an emphasis on the interaction between the cell and its environment. Although this model is only applied to cell spreading on a flat surface, the current implementation already allows for more complex settings of interaction with arbitrarily shaped smooth bodies, and cell-cell interaction.

The main novelty of the method developed in this work lies in the fact that the contact between a triangulated surface with "rounded" triangles reflecting the local curvature of a cell and its microenvironment is calculated by applying Maugis-Dugdale theory (see section 4.1.1) to all contacting triangles. To apply this adhesive contact model for the triangulated surfaces in our models, we build on the following six ideas (see section 4.1.3):

1. The triangulated surface can locally be approximated by spheres, i.e. a specific curvature is assigned to each triangle, see section 4.1.3.
2. All contact forces are normal to the intersection plane, which is defined by (encompassing) sphere-sphere or sphere-plane intersection. An in-depth discussion is provided in appendix E.
3. For the approximation of a spherical surface, the sum of all contact forces on the individual triangles must be equal to the appropriate continuum-mechanics force response. For details on this, the reader is referred to appendix F.

4. To integrate the contact force on each single triangle, quadrature rules can be used to calculate approximate pressures in specific points of the triangle. The details of this are discussed in section 4.1.3.
5. Having thus calculated the force on each triangle, it must be distributed to the nodes of the triangulation. This is done so that both total force and moments of the pressure contributions on that triangle are conserved. Details are to be found in section 4.1.3.
6. Finally, an over-damped equation of motion (comparable to (Drasdo, Hoehme, and Block 2007)) is solved for the nodes of the triangulation, see section 4.1.5.

This novel contact model is combined with an existing mechanical model for red blood cells (Dao, Li, and Suresh 2006; Fedosov, Caswell, and Karniadakis 2010). This model has been previously computed using a DPD solver, a different meso-scale simulation method. There is an abundance of increasingly detailed RBC models to be found in the literature. In particular, the approach of (Peng, Li, Pivkin, et al. 2013) is interesting, since it explicitly distinguishes the cytoskeleton and the membrane – a recent review is given by (Li, Vlahovska, and Karniadakis 2013). The mechanical model of the cortex of the RBC includes Finitely Extensible Non-linear Elastic (FENE) connections and viscous dissipation between the nodes of the triangulation, volume conservation and surface area conservation, as well as bending resistance – see section 4.1.4.

Finally, this newly developed method is applied to an in-depth computational investigation of RBC spreading (see figure 4.1) as reported by both (Hategan, Sengupta, Kahn, et al. 2004) and (Cuvelier, Thery, Chu, et al. 2007) in order to unravel the governing mechanisms.

4.1 Mathematical model of a deformable RBC

To explain the model developed in this work, Maugis-Dugdale theory is briefly summarized. Building on this theory, an in-depth description of the application of this theory to the contact mechanics of a cell with its mechanical microenvironment is given. Finally, the integration of that model with an existing mechanical model for the cortex of a Red Blood Cell is explained.

4.1.1 Maugis-Dugdale Theory

For two spherical asperities in contact or one asperity in contact with a flat surface (see figure 4.2), Maugis-Dugdale (MD) theory can be used to describe the contact

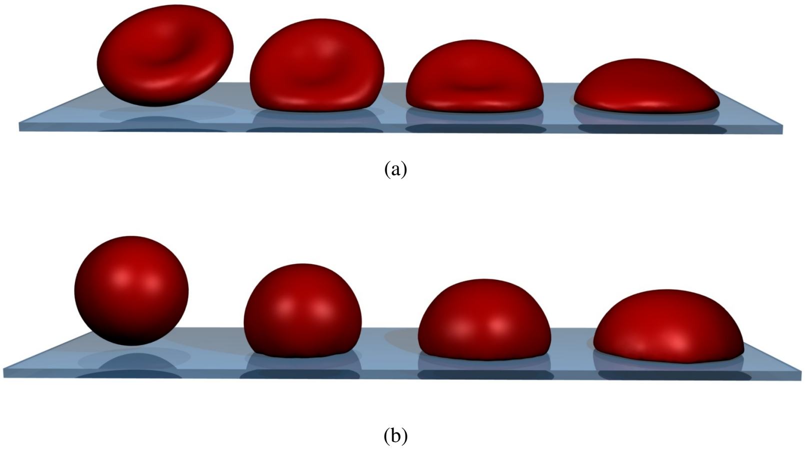

(a)

(b)

Figure 4.1: Simulated cell spreading of a Red Blood Cell at three different time-points. (a) biconcave RBC spreading. (b) "sphered" RBC spreading. From left to right: no contact at $t = 0\,\mathrm{s}$, early contact at $t = 0.1\,\mathrm{s}$, approximately the cross-over between the two regimes at $t = 0.3\,\mathrm{s}$ and the fully spread cell at $t = 1\,\mathrm{s}$. The biconcave RBC has approximately 40% less volume than the osmotically swollen spherical Red Blood Cell.

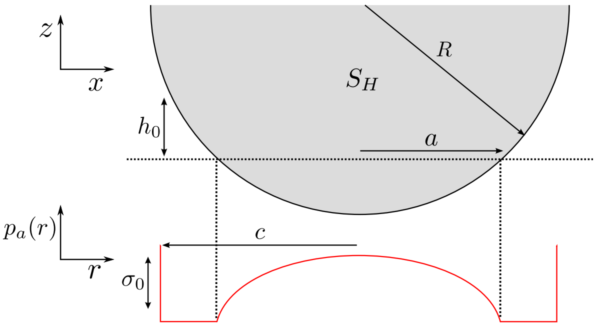

Figure 4.2: Schematic of a half-sphere S_H with radius R indenting a flat plane and adhesion stress p_a according to the Maugis-Dugdale model.

mechanics (Maugis 1992). As mentioned in section 3.1.2, this theory can be used to describe the full range between the DMT zone to the JKR limit of short interaction ranges and comparatively large adhesive deformations. The transition parameter λ has been defined by (equation 3.2):

$$\lambda = \sigma_0 \left(\frac{9\hat{R}}{2\pi W \hat{E}^2} \right)^{1/3}. \tag{4.1}$$

In equation 4.1, σ_0 is the maximum adhesive tension (measured in Pa) from a Lennard-Jones potential, W (in J/m^2) the adhesion energy, $\hat{R}$ is the reduced radius of the asperities and $\hat{E}$ the combined elastic modulus, as defined before.

The (repulsive) Hertz pressure associated with a contact of radius a is given by

$$p_H(r) = \frac{2\hat{E}}{\pi\hat{R}} \sqrt{a^2 - r^2}. \tag{4.2}$$

Assuming a spherical asperity – and therefore a circular contact area – the total Hertz force can be calculated by integrating equation 4.2 over the complete circular contact area with radius a, which yields the total Hertz force:

$$F_H = \frac{4\hat{E}a^3}{3\hat{R}} \tag{4.3}$$

An adhesive stress can be formulated as (K. Johnson 1997; Maugis 1992), see figure 4.2:

$$p_a(r) = \begin{cases} -\frac{\sigma_0}{\pi} \arccos\left\{ \frac{2a^2 - c^2 - r^2}{c^2 - r^2} \right\}, \; 0 \le r \le a, \\ -\sigma_0, \; a \le r \le c. \end{cases} \tag{4.4}$$

In the Maugis-Dugdale model, local adhesion tension is assumed to be independent of the overlap until a cut-off distance h_0. If the asperity is further than h_0 away from the flat surface, the adhesive tension drops to zero. Therefore, σ_0 is related to the adhesion energy W as:

$$W = h_0 \sigma_0. \tag{4.5}$$

W is the total work of adhesion, i.e. the work required to move the asperity away from the surface and out of contact. To pull a small area dA out of contact, the required work w is:

$$w = 2W \, \mathrm{d}A. \tag{4.6}$$

The total (global) adhesive force is the integral over the entire zone of adhesive contact with radius c, which according to (K. Johnson 1997) becomes:

$$F_a = -2\sigma_0 \left\{ c^2 \arccos\left(\frac{a}{c}\right) + a\sqrt{c^2 - a^2} \right\}. \tag{4.7}$$

The force in equation 4.7 is dependent on a. As equation 4.7 expresses the global adhesive force of the complete asperity, it is not a constant force, but through a dependent on the indentation. To calculate the adhesive radius c from the actual geometrical contact area with radius a, the height at the edge of the adhesive zone $h(c) = h_0 = W/\sigma_0$ can be calculated out to be (Johnson and Greenwood 1997):

$$\begin{aligned} 1 \quad = \quad & \tfrac{\lambda}{2}\left(\tfrac{a^3\hat{E}}{3\pi W\hat{R}}\right)^{2/3} \cdot \left[\left(m^2-2\right)\sec^{-1} m + \sqrt{m^2-1}\right] \\ & + \tfrac{4\lambda^2}{3}\left(\tfrac{a^3\hat{E}}{3\pi W\hat{R}}\right)^{2/3} \cdot \left(\sqrt{m^2-1}\sec^{-1} m - m + 1\right), \end{aligned} \tag{4.8}$$

where $m = c/a\,(\in \mathbb{R}^{>1})$. In general, to calculate both c and a from a given state of the contact, one needs to solve this equation simultaneously with the equation for the net contact force (Johnson and Greenwood 1997):

$$\|\mathbf{F}\| = \frac{a^3\hat{E}}{3\pi W\hat{R}^2} - \lambda\left(\frac{a^3\hat{E}}{3\pi W\hat{R}^2}\right)^{2/3}\left(\sqrt{m^2-1} + m^2\sec^{-1} m\right). \tag{4.9}$$

A very well validated contact model for soft, adhesive bodies like cells, the JKR theory (Barthel 2008; Chu, Dufour, Thiery, et al. 2005; Johnson, Kendall, and Roberts 1971), is a limiting case of Maugis-Dugdale theory for negligible cutoff-distance for the adhesive interaction h_0 (or $\lambda \gg 1$) . It has therefore a parameter less than MD theory. The adhesive pressure according to JKR (compare to equation 4.4) is

$$p_a(r) = \frac{F_{ij}}{2\pi a_{\mathrm{JKR}}^2}\left(1 - \frac{r^2}{a_{\mathrm{JKR}}^2}\right)^{-\frac{1}{2}}. \tag{4.10}$$

Note that this pressure diverges at $r \equiv a_{\mathrm{JKR}}$.

Summarizing the Maugis-Dugdale theory for an adhesive contact, one considers three distinct zones:

- The Hertz-zone with contact radius a, in which Hertz' theory determines the repulsive pressure. Apart from that, there is also an adhesive tension present in this contact zone.
- A purely adhesive zone with width $c - a$, in which no actual contact is formed but a constant adhesive tension is present. The adhesive force in this zone is determined by comparatively long-range interactions.
- From the edge of that adhesive zone outwards, no interactions take place, and contact pressures and tensions vanish.

4.1.2 Generating triangulated meshes of cells

The meshes used in this work are derived from spherical shapes by subdividing an icosahedron and projecting the nodes on a sphere (Van Liedekerke, Tijskens, Ramon, et al. 2010). In a subdivision, each triangle gets split into four triangles as is illustrated in figure 4.3. Here it is shown how one triangle with an encompassing sphere that matches the local curvature of the cell is split into four triangles. Since the local curvature is kept, the new triangle nodes are all located on the surface of the same encompassing sphere. Every subdivision of an icosahedron has only twelve nodes with a five-fold connectivity and slightly longer distances to their neighbours; otherwise, the mesh is perfectly regular with six-fold connectivity and is ideal for curvature calculations (see section 4.1.3) as reported by (Xu 2006).

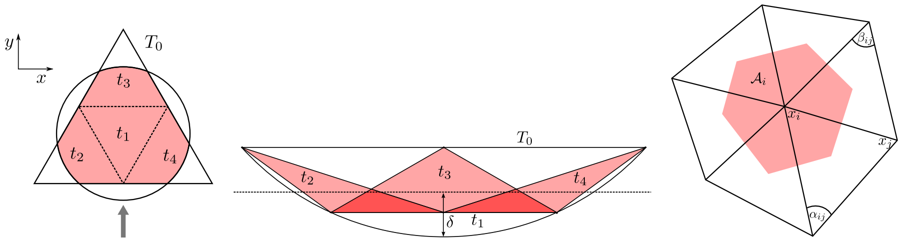

(a) Top view (b) Side view (c) Curvature calculation

Figure 4.3: Geometrical properties of triangulations with local curvatures. The top view (a) indicates the line of sight of the side view (b). (c) The contact between the cell boundary and external structures is calculated from encompassing spheres over the triangles with an inverse curvature that matches the local surface curvature. The drawing provides the geometrical definition of the Voronoi region area $\mathcal{A}_i$, angles α_{ij}, β_{ij} and points $\mathbf{x}_i, \mathbf{x}_j$ as used in equation 4.11.

The bi-concave shape of an RBC can be obtained by reducing the volume of the sphere to approximately 60 %, and letting a system of linear springs with appropriately chosen parameters relax again. This is the reverse process to the well described technique of RBC sphering, see e.g. (Fung and Tong 1968).

Meshes of either four or five subdivisions of an icosahedron are used, corresponding to 642 and 2562 nodes, respectively.

4.1.3 Contact mechanics of a triangulated surface

Local curvature of the 3D shape

Interaction between a surface and its surroundings is calculated as the interaction between two spheres, since this is an implicit requirement for Maugis-Dugdale theory. To that end, the encompassing sphere of each surface triangle is used. The outward side of the triangle is defined to be convex[1]. The radius of the encompassing sphere is calculated to correspond to the local inverse curvature of the triangulated surface. The inverse curvature of a triangle is calculated as the mean curvature of the three corner points, each weighted by their corresponding Voronoi region in the triangle. The curvature at each corner point i can be calculated as (Meyer, Desbrun, Schröder, et al. 2002):

$$\mathbf{K}(\mathbf{x}_i) = \frac{1}{2\mathcal{A}_i} \cdot \sum_{j \in \mathcal{N}_i} [\cot(\alpha_{ij}) + \cot(\beta_{ij})] (\mathbf{x}_i - \mathbf{x}_j) \tag{4.11}$$

K is called the Laplace-Beltrami operator, and its L^2-norm is twice the mean curvature while it points to the outward direction at this node. The variables in equation 4.11 are defined in figure 4.3(c) and the sum runs over all first order neighbours of node i, which are shown in the figure.

It should be noted, that a minimum curvature $\frac{1}{2}\|\mathbf{K}\| > 0$ is prescribed to avoid “infinite” radii. This becomes necessary to calculate contact forces in completely flat parts of the contact – here, the contact force is generally close to zero since the contact is long established and therefore in its equilibrium state. Although the calculation of the adhesive range c in MD theory loses accuracy by this artificial curvature, the force integration should still be a reasonable approximation, since all integration points (see below) can be expected to be in the “close contact” range a in this case.

Integrating the force on a triangle from the pressure distribution

When two triangulated surfaces come into contact, the contact potential is calculated from the overlap of their respective encompassing spheres. For two contacting spheres, there will be a circular contact area between the two of them, which also defines the direction of “normal” and “tangential” forces for this contact. If the two spheres are physical spheres, the contact point C_{Hertz} will always be located at the centre of this circular area since at this point the overlap distance δ (see figure 4.3(b)) will be maximal. In the case of contacting triangles, however, only a fragment of the sphere is

---

[1] This is a practical consideration: theory only requires $\hat{R}$ to be positive – see equation 3.3 – so in cases where particles with only relatively high convex curvature come in contact with particle(s) with relatively lower concave curvature (e.g. cells in a test-tube), this restriction can be relaxed.

physical and it has to be checked that a contact force needs to be calculated – appendix E details how that can be done for any pair of rounded triangles. The cases of a contact with a sphere or a (polygonal) plane are dealt with analogously.

If the check asserts that a contact force can be expected between the triangles (or the triangle and a plane, and so forth), for computational reasons distinguish two regimes are distinguished: In the first case, the contact area between the encompassing spheres is relatively large (see below, equation 4.15). In this case, we can assume a relatively big, well established contact between the two surfaces. Therefore, the pressures in equations 4.2 and 4.4 are integrated. This integral is approximated using quadrature rules for numerical integration (Cowper 1973; Zhang, Cui, and Liu 2009). For integrating any function f over a triangle surface $A_\triangle$, the approximation has the form:

$$\iint_{A_\triangle} f(\alpha,\beta,\gamma)\,dA \approx A_\triangle \sum_{i=1}^{N} w_i f(\alpha_i,\beta_i,\gamma_i) \tag{4.12}$$

in which α, β and γ are barycentric coordinates inside the triangle, and w_i are the weights assigned to each quadrature point i.

To calculate both forces and moments caused by a specific pressure/traction of the triangle, we first determine the coordinates of the integration test points. From these points, the squared distance r^2 from the centre of the circle of contact can be calculated. Using equation 4.12 the weighed sum can be evaluated, thus approximating the double integral for the force on a triangle:

$$\mathbf{F}_t = \sum_{i=1}^{N_Q} \frac{A_\triangle}{N_Q} w_i p\left(r_i\right) \hat{\mathbf{n}}, \tag{4.13}$$

where $p\left(r_i\right)$ is the sum of the adhesive Maugis-Dugdale pressure (equation 4.4) and Hertz' repulsion (equation 4.2), and $\hat{\mathbf{n}}$ is the normal unit vector to the contact plane; N_Q is the number of quadrature points. The divergence in the JKR adhesive stress (equation 4.10) makes it difficult to numerically integrate. For this reason and the added flexibility of MD theory, this more general framework is chosen. Since the radius of intimate contact, a, is directly known as the radius of the intersection circle of the two encompassing spheres, we only have to solve equation 4.8 numerically for m to obtain the adhesive contact radius c (used in equation 4.4).

The pressure $p\left(r_i\right)$ is evaluated in the positions corresponding to those quadrature points. Additionally, the moments of each individual force component with respect to the centre of the contact plane are summed up:

$$\mathbf{M_t} = \sum_{i=1}^{N_Q} \frac{A_\triangle}{N_Q} w_i p\left(r_i\right) \mathbf{r}_i \times \hat{\mathbf{n}}. \tag{4.14}$$

To ensure sufficient precision at an adequate speed, a 16-point quadrature rule of degree eight (Zhang, Cui, and Liu 2009) is used that is still acceptably fast, since calculations only take place for triangles for which contact has been ascertained.

If the area of contact between the two encompassing spheres is relatively small compared to the typical area of each integration point:

$$\pi c^2 < 2A_{\triangle}/N_Q, \tag{4.15}$$

we can expect a bad approximation for force and moment. Therefore, a different approach is chosen: The integrated MD force (equation 4.9) calculated from the total area of contact of the encompassing spheres can be scaled with the fraction of the area, which is contained in the intersection of the two triangles. This total force is then applied to the contact point C_{Hertz}, if the point is within the triangle's intersection, or the point closest to it in that intersection polygon. In this case, the moment is still calculated according to equation 4.14, although the sum only contains the integrated MD force and radius vector.

This second approximation for the forces and the moments one triangle of the body is subject to, is insufficient for bigger overlaps, because the moments generated by the repulsive and adhesive pressures described in equations 4.2 and 4.4 differ profoundly from that simple approximation. For small overlaps, it is obvious from equation 4.14 that the moment is close to $\mathbf{0}$ since the lever length $\mathbf{r}$ is very short, anyway.

The contact force calculated in this way does not depend on the chosen mesh – see appendix F.

Distribution of force to the nodes of the triangulation

To calculate the force at each node of the triangle, both the force vector and the moment vector must be taken into account. The moment-vector necessarily lies in the contact plane, since the force is defined to be normal to this plane. Let the contact plane without loss of generality be the x-y plane. This implies that $\|\mathbf{F}_t\| = F_t^z$ and the position vectors of the $i = (1,2,3)$ nodes w.r.t. the Hertz contact point are $\mathbf{r}_{n_i} = \left(r_{n_i}^x, r_{n_i}^y, 0\right)$. Then, the system of equations can be conveniently written as

$$\left(\begin{array}{rcrcrcl} r_{n_1}^y \cdot F_{n_1}^z & + & r_{n_2}^y \cdot F_{n_2}^z & + & r_{n_3}^y \cdot F_{n_3}^z & = & M_t^x \\ -r_{n_1}^x \cdot F_{n_1}^z & - & r_{n_2}^x \cdot F_{n_2}^z & - & r_{n_3}^x \cdot F_{n_3}^z & = & M_t^y \\ F_{n_1}^z & + & F_{n_2}^z & + & F_{n_3}^z & = & F_t^z \end{array}\right). \tag{4.16}$$

This system can be inverted to find the correct forces on the nodes of the triangulation.

4.1.4 Elastic model of the cortex

In the deformable cell model, the cortex nodes interact through viscoelastic potentials. In the most simple approach, a linear elastic spring could be used. For a given displacement of nodes i and j, the elastic spring force over a connection is:

$$F_{\text{Linear}} = k_s \left(d_{ij} - d^*_{ij}\right), \tag{4.17}$$

in which d_{ij} and d^*_{ij} are the actual distance and equilibrium distance between connected node i and j. The linear spring stiffness is called k_s. For red blood cells, two non-linear spring models have been used in literature: the FENE and the Worm-Like Chain model (WLC) (Fedosov, Caswell, and Karniadakis 2010). These models express that upon stretching, the biopolymers of the cytoskeleton – a sub-membranous network of spectrin connections for RBCs – first uncoil, providing relatively little resistance, but when completely stretched out, become practically non-extensible.

Between two connected nodes i and j, the FENE attractive potential reads:

$$U_{\text{FENE}} = -\frac{k_s}{2}\, d^2_{\text{max}} \log\left[1 - \left(\frac{d_{ij}}{d_{\text{max}}}\right)^2\right], \tag{4.18}$$

where d_{max} is the maximal distance, and k_s the stretching constant. The force derived from this is:

$$F_{\text{FENE}} = -k_s\, d_{ij} \left[1 - \left(\frac{d_{ij}}{d_{\text{max}}}\right)^2\right]^{-1}. \tag{4.19}$$

FENE springs exert purely attractive forces. In order to account for the (limited) incompressibility of the spectrin, a simple power law is used (power L):

$$F_{\text{POW}} = \frac{k_c}{d^L_{ij}} \tag{4.20}$$

The incompressibility coefficient k_c can be derived for the assumption that the total force must vanish for $d_{ij} \equiv d^*_{ij}$:

$$k_c = k_s \left(d^*_{ij}\right)^{L+1} \left[1 - \left(\frac{d^*_{ij}}{d_{\text{max}}}\right)^2\right]^{-1} \tag{4.21}$$

In the present model, $L = 2$ as suggested by (Fedosov, Caswell, and Karniadakis 2010). It is convenient to denote the maximal stretch $\frac{d_{\text{max}}}{d^*_{ij}}$ by x_{max}, the fraction of maximal extension and equilibrium distance

In addition to this purely elastic potential, dissipation as per the Kelvin-Voigt model is included by adding a parallel dashpot with the damping constant c:

$$F_{\text{Dashpot}} = -c\,\hat{\mathbf{n}}_{ij} \cdot \mathbf{v}_{ij}. \tag{4.22}$$

Here, $\hat{\mathbf{n}}_{ij} \cdot \mathbf{v}_{ij}$ is the projection of the relative velocity of a pair of connected cortex nodes on their connecting axis. The force is also applied in the direction of the connection.

Whereas in-plane stretching and compressive forces can be calculated purely based on the distance between two neighbouring cortex nodes, bending forces are calculated for two neighbouring triangles. The bending moment between two adjacent triangles is given as

$$M = k_b \sin\left(\theta - \theta^*\right). \tag{4.23}$$

Here, k_b is the model parameter determining the bending rigidity, θ is the instantaneous angle and θ^* the spontaneous angle between a pair of triangles with a common edge. A corresponding force is applied to the non-common points of each of the two triangles, with a compensating force applied to the points on the common edge, ensuring that the total force on the cell remains unchanged. This type of bending-stiffness is commonly found in the literature for RBC models, e.g. by (Fedosov, Lei, Caswell, et al. 2011) and (Discher, Boal, and Boey 1998) – a more general analysis is provided by (Boal and Rao 1992).

Additionally, both a global and local area constraint is used, making sure that both the individual triangle areas and the total area of the red blood cell cannot strongly increase or decrease. As described by (Fedosov, Lei, Caswell, et al. 2011), this is achieved by a local force with magnitude:

$$F_{A,\text{local}} = k_a\left(A_\triangle - A_\triangle^*\right), \tag{4.24}$$

in which $A_\triangle$ is the triangle area, $A_\triangle^*$ the resting triangle area and k_a the local constraint constant. The magnitude of the global force is formulated as:

$$F_{A,\text{global}} = k_d\left(A_{\text{tot}} - A_{\text{tot}}^*\right), \tag{4.25}$$

where A_{tot} is the total RBC area, A_{tot}^* the total resting area and k_d the global constraint constant. For both constants, values were taken from (Fedosov, Caswell, and Karniadakis 2010). These forces are applied in the plane of each triangle in the direction from the barycentre of the triangle.

Finally, a volume constraint is added since for short time-scales, the total cytosol volume of the cell can be considered constant. As for the area, magnitude of the force takes the form

$$F_{\text{volume}} = k_V\left(V - V^*\right), \tag{4.26}$$

with the instantaneous cell volume V and the initial cell volume V^*. This force is applied to each node of the cell in its outward direction as found by the Laplace-Beltrami operator, see equation 4.11.

4.1.5 Equation of motion

In the low Reynolds number environment in which cells live, motion is dominated by viscous forces (Purcell 1977). In other words, inertial forces are negligible. For each integration node, Newton's second law (with explicit Stokes' drag)

$$\mathbf{F}^i = m\mathbf{a}^i + \zeta \mathbf{v}^i, \tag{4.27}$$

by leaving out the inertial term, becomes

$$\begin{aligned} & \sum_{\text{triangles } l} \mathbf{F}^{il}_{\text{contact}} + \mathbf{F}^{il}_{A,\text{local}} + \mathbf{F}^{il}_{A,\text{global}} \\ + & \sum_{\text{conn. } k} \mathbf{F}^{ik}_{\text{FENE}} + \mathbf{F}^{ik}_{\text{POW}} + \mathbf{F}^{ik}_{\text{bend}} \\ + & \mathbf{F}^{i}_{\text{volume}} + \mathbf{F}^{i}_{\text{gravity}} + \mathbf{F}^{i}_{\text{random}} \\ = & \sum_{\text{triangles } l} \Gamma^{il}_{\text{substrate}} \mathbf{v}^i + \sum_{\text{conn. } k} c(\mathbf{v}^i - \mathbf{v}^k) + \Gamma^{i}_{\text{liquid}} \mathbf{v}^i . \end{aligned} \tag{4.28}$$

The total force on node i is the sum of all the individual forces: Firstly, the forces that are calculated on the triangles are transferred to the nodes – the contact forces $\mathbf{F}_{\text{contact}}$ only exist for triangles, which are in contact with the substrate. Also, the local and global area constraints for the membrane are added here. Secondly, the cortex connection forces between node i and all fixed connections k are added, and finally the volume constraint and the gravitational force $\mathbf{F}_{\text{gravity}}$ as well as a random force $\mathbf{F}_{\text{random}}$ for taking into account fluctuations of the membrane can be added. Since those fluctuations do not much influence the spreading dynamics in for the presented results, that term can be neglected.

For the right-hand side, we not only discard the term proportional to mass, but we also more explicitly state the components of the constant ζ: starting with the dissipative/friction term generated from the encompassing sphere - encompassing sphere friction between two contacting triangles – in the case of RBC spreading, friction with the substrate $\Gamma_{\text{substrate}}$. This coefficient is weighted by the distance of the node i from the contact point in that triangle. This ensures symmetry of the friction-matrix (see below) and corresponds to the distribution of the contact force. The component of the substrate friction for a triangle is defined as (compare to e.g. (Hoehme and Drasdo 2005)) $\Gamma_\triangle = A^C_\triangle \left[\gamma_n \hat{\mathbf{n}}\hat{\mathbf{n}}^{\mathrm{T}} + \gamma_t \left(\mathbf{I} - \hat{\mathbf{n}}\hat{\mathbf{n}}^{\mathrm{T}}\right)\right]$ where $A^C_\triangle$ is the area of contact in that triangle, $\hat{\mathbf{n}}$ is the normalized direction vector between the two encompassing spheres and γ_n, γ_t are, respectively, the normal and tangential friction constants.

Secondly, we have the dissipative dashpot of the connections of this node, and lastly we add the drag coefficient Γ_{liquid} for the whole cell in plasma: here, in a first order approximation, we simply divide the formula from Stokes' law by the number of nodes per cell, thereby recapturing the exact result for a spherical cell in Stokes flow.

For nodes, whose surrounding triangles are all in contact with the substrate, we define a very high friction constant $\Gamma^i_{\text{substrate}}$, effectively fixing those nodes in place. No influence of this factor on the spreading curves was found (it can be completely left out), but it helps to dampen out small numerical fluctuations in the stiff potential of the contacting plane. This allows us to use larger time steps Δt when solving the equation of motion.

Equation 4.28, which is used in essentially the same form by e.g. (Galle, Loeffler, and Drasdo 2005; Hoehme and Drasdo 2005; Hoehme, Brulport, Bauer, et al. 2010; Krinner, Hoffmann, Loeffler, et al. 2010; Ramis-Conde, Chaplain, Anderson, et al. 2009; Van Liedekerke, Smeets, Odenthal, et al. 2013), is a first order differential equation, which couples the movements of all particles together. When writing the whole system as

$$\underline{\Gamma} \cdot \underline{\mathbf{v}} = \underline{\mathbf{F}}, \tag{4.29}$$

it can be shown – compare appendix D, (Van Liedekerke, Smeets, Odenthal, et al. 2013) – that the matrix $\underline{\Gamma}$ is positive definite, and therefore the system can be iteratively solved for the velocities by using the CG method. Subsequently, the nodes' movement is integrated by a forward Euler scheme. For a low Reynolds number environment, the amount of kinetic energy (or motion) directly corresponds to the amount of dissipated energy. Equation 4.29 shows all dissipative terms in the matrix Γ which dictates the degree of motion induced by the (conservative) forces $\underline{\mathbf{F}}$. Identifying all significant dissipative mechanisms is therefore crucial for calculating the dynamics of this system.

4.2 Results of the RBC model

To show the validity of the model assumptions concerning cortex mechanics, we first compare simulated red blood cell stretching to experiments reported in the literature (Suresh, Spatz, Mills, et al. 2005). A combination of a FENE potential and a power law for area incompressibility was used to model the elastic properties of an element of the RBC cortex (see section 4.1.4).

4.2.1 Validation of the RBC cortex model

RBC stretching experiments

Using the deformable cell model, cell stretching simulations can be used to validate the elastic constants of the RBC with respect to optical tweezers measurements, in which a red blood cell is attached to two beads on opposite sides. In the experiment, the beads are pulled apart with a set force, and the deformation of the RBC is measured (Suresh, Spatz, Mills, et al. 2005)

To simulate the RBC behaviour, the outermost 5 % of the nodes are pulled with the same force, and the system is left to equilibrate. The same parameters as used by (Fedosov, Lei, Caswell, et al. 2011) in their DPD model yielded comparable results for the presented model – see table 4.1.

Figure 4.4(b) gives a visualization of the stretched RBC for stretching forces of 0, 50 and 150 pN. In figure 4.4(a) the change in both axial diameter D_A and transversal diameter D_T is shown for different cell stretching forces. This curve corresponds well to the computational results presented in the paper of (Fedosov, Lei, Caswell, et al. 2011), who report a maximal axial diameter of 16 µm and a minimal transversal diameter between 4 and 5 µm at a force of 200 pN, as well as experimental data by (Suresh, Spatz, Mills, et al. 2005).

RBC Relaxation

In order to validate the dissipation constants of the cortex itself (see equation 4.22), a relaxation simulation was performed. In this *in-silico* experiment, the cell is first stretched with a fixed force until a constant axial diameter D_A of approximately 8.9 µm is observed. Subsequently, the force is released and the change in D_A over time is monitored. For a liquid viscosity of blood plasma, we found that the cortex damping coefficient c should be chosen in the order of 5×10^{-7} Pa s to match experimentally observed RBC relaxation dynamics (Figure 4.5). In this case, the computational results are in good agreement with experimentally observed RBC relaxation times in the order of 0.1-0.3 s (Van Liedekerke, Smeets, Odenthal, et al. 2013).

4.2.2 Cell spreading experiments

In the experiments reported by (Cuvelier, Thery, Chu, et al. 2007), biotinylated RBCs were osmotically swollen to become spherical and the change of the radius of the contact area with time was measured for spreading on a streptavidin coated surface. To compare to the spreading dynamics reported in that paper as well as by (Hategan,

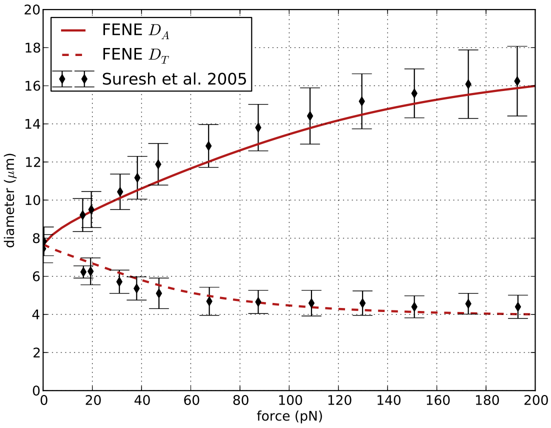

(a) Numerical results cell stretching

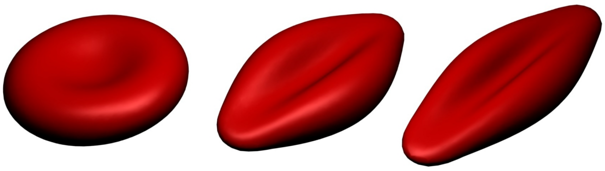

(b) Left: 0 pN, middle: 50 pN, right: 150 pN

Figure 4.4: Results of cell stretching. (a) shows the change of axial diameter D_A and transversal diameter D_T in function of the stretching force, compared to experimental data from (Suresh, Spatz, Mills, et al. 2005). (b) visualizes red blood cells for different stretching forces.

Sengupta, Kahn, et al. 2004) (where the cells spread on a polylysine coated surface), simulations of the described model were set up with the parameters as given in table 4.1.

The red blood cell is modelled with a viscoelastic cortex including bending stiffness and Maugis-Dugdale contact interactions. Most parameters in table 4.1 are taken directly from the literature as indicated. The effective range of interaction h_0 (see equation 4.5) was estimated at 24.8 nm by interpolating from (Leckband and Israelachvili 2001) for cells with a radius of $\approx 3\,\mu$m. The cortex Young's modulus used in the Maugis-Dugdale model is the material stiffness of the phospholipid-spectrin complex (the elasticity of the deforming membrane is already taken into account by the FENE potentials). This

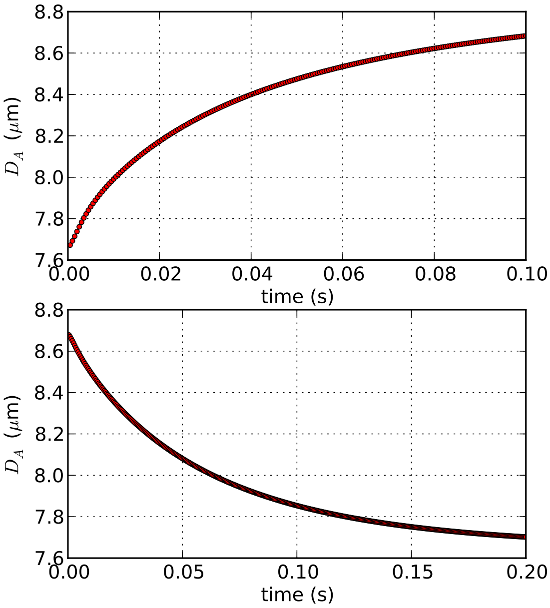

Figure 4.5: Computational results for cell relaxation. Top: cell stretching dynamics. Bottom: cell relaxation dynamics; cortex damping $c = 5 \times 10^{-7}$ Pa s

material stiffness can be assumed to be much higher compared to the whole cell's Young's modulus and is set at a value of 800 kPa. The parameters for the cortex are validated by performing the cell stretching and relaxation experiments explained in the previous section 4.2.1.

4.2.3 Visual and static comparison to data

A view on three stages of the cell spreading for both biconcave and sphered RBCs is presented in figure 4.1. Note that the volume of the biconcave RBC is only about 60 % of the volume of the sphered RBC. As a result of that, for the sphered RBC, the final height of the spread-out cell is greater and it has a higher angle of contact compared to the final shape of the initially biconcave RBC.

For this simulation, a triangulation based on a five-fold subdivision of an icosahedron was used – see section 4.1.2. This level of mesh refinement is required to reproduce the final high curvatures at the edge of the contact area when the cell is fully spread out: The triangles at the edge have encompassing spheres with radii of ca. 200 nm, while

Table 4.1: Parameters used for the RBC-spreading model matching data from (Hategan, Sengupta, Kahn, et al. 2004). *: Values matching data from (Cuvelier, Thery, Chu, et al. 2007): $W = 88 \times 10^{-6}\,\mathrm{J/m^2}$ (as reported in (Cuvelier, Thery, Chu, et al. 2007)), $\gamma_n = 200 \times 10^9\,\mathrm{N\,s/m^3}$, $\gamma_t = 120 \times 10^9\,\mathrm{N\,s/m^3}$, $\Delta t = 50 \times 10^{-6}\,\mathrm{s}$. Parameter values estimated from [1](Cuvelier, Thery, Chu, et al. 2007), [2](Hategan, Sengupta, Kahn, et al. 2004), [3](Drasdo, Hoehme, and Block 2007), [4](Galle, Loeffler, and Drasdo 2005), [5](Hoehme, Brulport, Bauer, et al. 2010), [6](Israelachvili 2011), [7](Fedosov, Caswell, and Karniadakis 2010), [8](Boal 2012).

Parameter	Symbol	Value	Units	estimated from:
time-step*	Δt	$6 \cdot 10^{-6}$	s	trial runs
simulation time	T_{end}	1.2	s	[1]
CG precision	e_{max}	$10 \cdot 10^{-15}$	N	trial runs
cell radius	r	$3.25 \cdot 10^{-6}$	m	surface area RBC [2]
medium viscosity	η	$0.8 \cdot 10^{-3}$	Pa s	Blood plasma at 37 °C
Young's modulus cortex	E	$800 \cdot 10^{3}$	Pa	trial runs
Poisson's ratio	ν	0.4	-	[3]
tangential friction coef.*	γ_t	$6 \cdot 10^{9}$	$\mathrm{N\,s/m^3}$	"fitted", [4,5]
normal friction coef.*	γ_n	$8 \cdot 10^{9}$	$\mathrm{N\,s/m^3}$	"fitted", [4,5]
adhesion constant*	W	$1 \cdot 10^{-3}$	$\mathrm{J/m^2}$	[1]
effective adhesive range	h_0	$20 \cdot 10^{-9}$	m	interpolated from [6]
FENE constant (stretch)	k_s	$3.2 \cdot 10^{-6}$	J	[7], [8]
maximal FENE stretch	x_0	2.05	[-]	[7]
cortex bending constant	k_b	$240 \cdot 10^{-21}$	N m	[7], [8]
cortex damping	c	$1.5 \cdot 10^{-6}$	Pa s	relaxation exp.
local area constraint	k_a	$6 \cdot 10^{3}$	$\mathrm{N/m^2}$	[7]
global area constraint	k_d	$6 \cdot 10^{3}$	$\mathrm{N/m^2}$	[1]
volume constraint	k_V	$10 \cdot 10^{3}$	$\mathrm{N/m^3}$	trial runs

(Hategan, Law, Kahn, et al. 2003) report a typical radius of the rim for this situation of $125 \pm 40\,\mathrm{nm}$, which is of comparable order of magnitude.

The shape of the final spread-out cell is a spherical cap. By fitting a sphere through the top 95 % of the nodes, the effective contact angle (Seifert and Lipowsky 1990) can be estimated. For the modelled RBC, an effective contact angle of $\approx 65^\circ$ can be obtained, which corresponds reasonably well to the measured effective contact angle of around 60° (Hategan, Law, Kahn, et al. 2003).

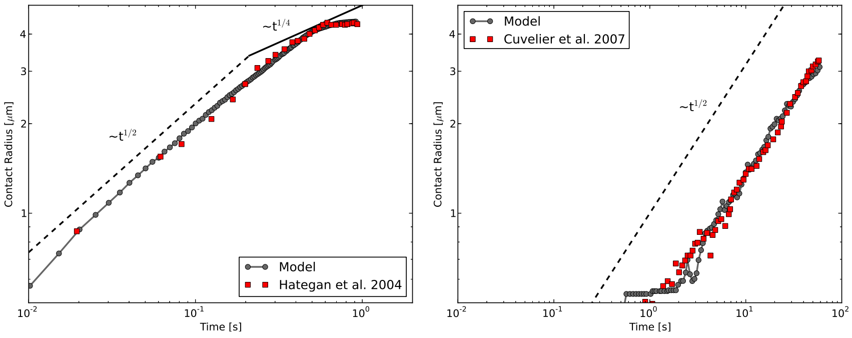

(a) Experiment Hategan et al. (b) Experiment Cuvelier et al.

Figure 4.6: Contact radius vs. time for cell spreading simulations: comparison with experimental data from (a) (Hategan, Sengupta, Kahn, et al. 2004) for adhesion strength of 1 mJ/m^2 and with data from (Cuvelier, Thery, Chu, et al. 2007) (b) for adhesion strength of 88 μJ/m^2 – here, a coarser mesh with 642 nodes instead of 2562 nodes is used since the cell does not spread completely in the given time-frame and therefore does not exhibit the high local curvatures as in the Hategan experiment.

4.2.4 Comparison to dynamic data & influence of parameters

Figure 4.6 shows the power-law behaviour of the sphered RBC spreading in double logarithmic representation. The "contact radius" of the RBC r_{cc} in these and the following figures is calculated from the sum of all the triangles' areas which are in contact $A^C = \sum_\triangle A^C_\triangle$ by defining $r_{cc} = \sqrt{A^C/\pi}$. The spreading dynamics of the model match the experimentally observed cell spreading (Hategan, Sengupta, Kahn, et al. 2004) very well.

Figure 4.7 summarizes the influence of varying one parameter at a time for the most influential parameters of the model starting from the base parameter set reported in table 4.1. Its first sub-figure 4.7(a) shows simulation results of cell spreading for different values of the cell-substrate adhesion strength W. A lower adhesion strength results in a smaller final contact radius, but also makes the spreading slower. However, the $\sim t^{1/2}$ power law behaviour as reported by (Cuvelier, Thery, Chu, et al. 2007) stays well conserved for different adhesion strengths.

The influence of the FENE stretching constant k_s is shown in figure 4.7(b). In the range of the RBC FENE constant (in the order of 1×10^{-6} N/m), the influence of k_s on the spreading dynamics is comparatively small. For larger deviations, higher values of k_s limit the final spreading radius to a smaller value, or conversely, lower values allow the

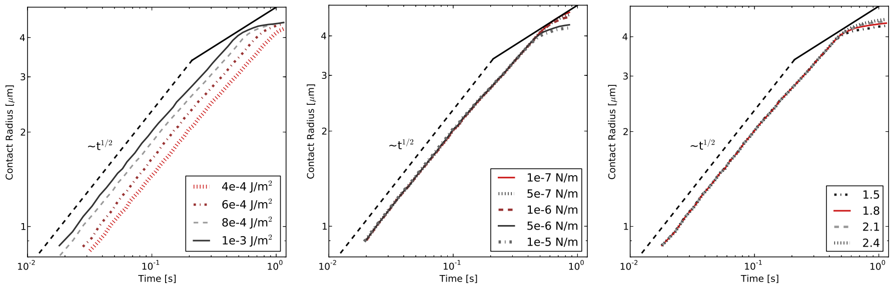

(a) Adhesion strength W (b) FENE stiffness k_s (c) Maximal FENE stretch $x_{\max}$

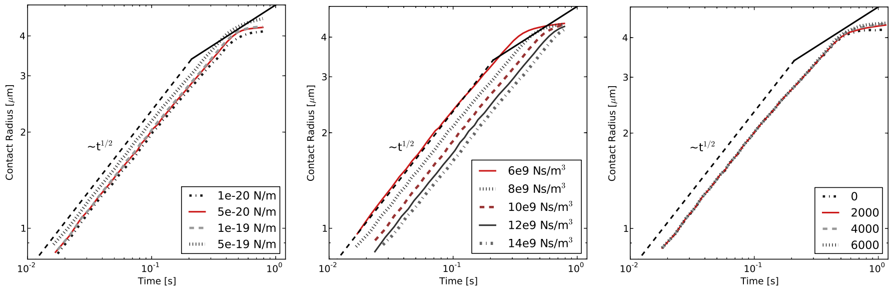

(d) Bending stiffness k_b (e) Parallel friction γ_n (f) Local area constant k_a

Figure 4.7: Variation of most influential model parameters. Double-logarithmic plots of cell contact radius r_{cc} versus time. (a) varying cell-substrate adhesion strength W yields both a shift in speed and final contact radius. (b) varying the FENE stretching constant k_s yields different final contact radii, (c) varying the FENE max stretch $x_{\max}$ also mostly influences the final contact radii, (d) varying bending stiffness k_b influences both spreading speed and final contact radius, (e) varying the normal friction coefficient γ_n influences spreading speed and (f) varying the local area constraint constant k_a influences the final spreading radius.

cell to spread considerably more.

A FENE connection is also characterized by the maximal stretch $x_{\max}$ (figure 4.7(c)), which expresses the maximal extension of the spring, at which the FENE force diverges (equation 4.19). The initial spreading dynamics are not affected by the precise value of $x_{\max}$, but the final spreading radius is. For higher values of $x_{\max}$, the same tension in the cortex corresponds to a larger extension and therefore a larger radius of the spread out cell.

The effect of the bending stiffness on RBC spreading is shown in figure 4.7(d). A higher bending resistance of the cortex speeds up cell spreading, the probable reason being that, through resisting to bending, the cortex keeps the contact angle within the effective range of adhesive interaction close to 180°. This range is of the order of 20 nm for microscopic biomolecular surfaces (Leckband and Israelachvili 2001). It should be noted that for a theoretical vesicle with bending resistance, the actual contact angle is always 180° (Seifert and Lipowsky 1990). However, for a real RBC, the width of the adhesive spreading front is non-zero and determined by the effective range of interaction h_0. This effective adhesive range is taken into account in Maugis-Dugdale theory (equation 4.5) and relates the maximal adhesive tension at the edge of contact to the total work of adhesion W.

The normal friction coefficient γ_n is determined by the energy dissipation when adhesive contact is initiated. The dissipation is caused by snap-in-contact events when adhesion molecules form bonds, and the hysteresis arising from unbinding stochastically again (Leckband and Israelachvili 2001). In figure 4.7(e), the effect of changing γ_n on the RBC spreading dynamics is shown. As could be expected, a lower value of γ_n diminishes the energy dissipation due to adhesion and therefore increases the rate of cell spreading. However it does not change the initial $\sim t^{1/2}$ power law behaviour of cell spreading.

Finally, in figure 4.7(f), the effect of the local area constraint on the spreading dynamics is shown. When the value of k_a is too low, degenerate triangle shapes can arise with a strongly decreased area. This will result in an underestimation of the final spreading radius. It can be observed that for values of $k_a \geq 2000\,\mathrm{N/m^2}$, the local area of the triangles is sufficiently well conserved and the predicted spreading dynamics are not affected.

4.2.5 Evolution of forces acting on the cell

In figure 4.8(a), the outward normal pressure on the nodes is visualized for three distinct phases of the cell spreading process for a sphered RBC. The normal pressure is defined here as the magnitude of the sum of all forces in the nodes projected onto the normal in that node – therefore this normal pressure is dominated by contact forces, where adhesive ones yield a positive pressure in this case. Figure 4.8(b) shows the in-plane tension τ (in J/m^2) of the cortex at the same time points. This tension is characterized by the FENE force at the inter nodal connections. Positive forces in these connections correspond to tensile stress in the cortex, while negative values are associated with compressive stress:

$$\tau_i = \frac{1}{N_c^i} \sum_{j \in N_c^i} \sqrt{3} \frac{F_{\mathrm{FENE}}}{d_{ij}}, \tag{4.30}$$

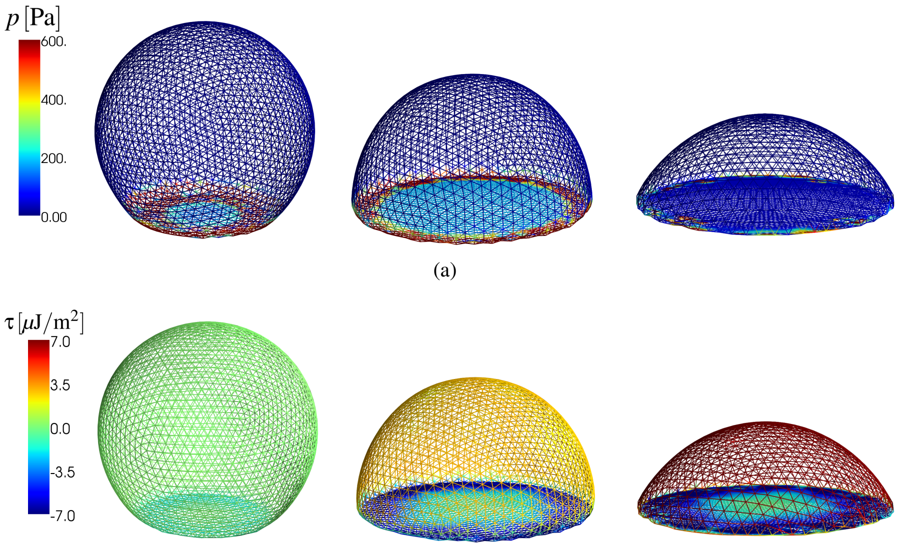

(a)

(b)

Figure 4.8: Normal pressure and cortex tension of a spreading RBC. (a) Normal pressure calculated at the nodes at different time points during cell spreading. left: $t = 100\,\text{ms}$, middle: $t = 350\,\text{ms}$, right: $t = 900\,\text{ms}$. (b) Tension (see equation 4.30) averaged at the nodes during cell spreading at the same time points.

where N_c^i is the number of FENE connections of node i and d_{ij} is the inter-nodal distance (see e.g. (Boal 2012)).

At $t = 100\,\text{ms}$ the spreading dynamics correspond to the $\sim t^{1/2}$ power law regime. At this stage, adhesive forces are strong especially at the edge of contact, but also in the entire rapidly increasing circular contact area. The elastic energy stored in the membrane at this point in time is very low, as the stretch and bending in the membrane is small. As a result, almost all the energy dissipation (see section 4.1.5) takes place in the contact area.

At $t = 350\,\text{ms}$, a distinct adhesive edge can be observed, in which the magnitude of forces is much stronger than in the inner circle of the contact area, where the contact potential is already nearly minimal. At the edge, the cortex's bending stiffness provides resistance to the strong adhesive tension. Meanwhile, the upper spherical cap is being stretched while at the plane of contact the membrane – together with the substrate it is adhering to – is under compressive stress. At this stage, energy dissipation takes place not only at the substrate interface, but also in the entire stressed cortex. As a result of this, the spreading slows down to a lower rate than the $\sim t^{1/2}$ power law regime.

At $t = 900\,\mathrm{ms}$, spreading has stopped and the cell has reached equilibrium. The forces at the nodes are zero, and the adhesive tension at the edge of contact is being balanced out by the elastic stress in the RBC membrane/cortex. The cortex in the spherical cap is under strong tensile stress and the stretch in the connections is close to its maximal value x_{max}. At the substrate interface, compressive stresses have built up even more. For an elastic substrate, these compressive forces will cause radial inwards deformation of the substrate, as has been observed in traction force microscopy measurements (Legant, Choi, Miller, et al. 2013; Wang, Ostuni, Whitesides, et al. 2002) – although these experiments concern late cell spreading.

It should be noted that the maximal normal pressure at the nodes – occurring in the first stage of cell spreading – corresponds to a force in the order of 100 pN, which is in the range of the force applied in the stretching simulations which were used to validate the model parameters of the elastic cortex, see section 4.2.1.

4.3 Discussion of the RBC modelling results

4.3.1 Model performance and limitations

First, with regard to the performance of the newly developed model for a triangulated, deformable cell obeying Maugis-Dugdale contact tractions, we conclude that:

1. The quasi-static cell stretching experiments as analysed by (Fedosov, Caswell, and Karniadakis 2010; Fedosov, Lei, Caswell, et al. 2011) are reproduced with nearly identical parameters although the simulation technique used is different (DPD vs. first-order equation of motion inspired by Stokesian dynamics (Brady and Bossis 1988)) – see section 4.2.1.
2. The model recapitulates the mechanical behaviour of a spreading red blood cell with high precision. From known mechanical parameters it accurately reproduces the cell spreading curves experimentally obtained by (Hategan, Sengupta, Kahn, et al. 2004) and (Cuvelier, Thery, Chu, et al. 2007).
3. Contact calculations between (rounded) facets of the triangulation show three important advantages over naive node-node based contact calculation schemes:
    (a) Parameters are physically meaningful, well defined and (in principal) measurable;
    (b) using these parameters for different mesh refinements yields very similar results for cell spreading, and

   (c) the desired accuracy is tunable – both by choosing a finer mesh or more quadrature points for higher accuracy, as needed.

4. The dynamics of both experiments (RBC on polylysine-coated glass, biotinylated RBC on streptavidin substrate, (Hategan, Sengupta, Kahn, et al. 2004), (Cuvelier, Thery, Chu, et al. 2007)) can be matched by only changing the adhesion energy as given by (Cuvelier, Thery, Chu, et al. 2007) and adjusting the friction constants γ_n, γ_t (table 4.1). The contact dissipation cannot be expected to be identical for these two situations, since in the first case, the cell is completely spread within a second, whereas in the second case it takes about a minute. Therefore, rates, numbers and nature of binding/unbinding events will be vastly different, giving rise to different dissipation levels (for a more thorough explanation, see e.g. (Israelachvili 2011), chapter 9.4).

5. The use of a FENE-like potential is important to consistently obtain these spreading dynamics (data not shown). The same behaviour cannot be captured by simple linear springs since they would be either too stiff to allow the initial “fast” spreading phase, or too soft to keep the cell from spreading out too much when the adhesion driven spreading stops. The FENE potential captures this initial softness and final stiffness of the spectrin connections very well (see figure 4.4). As a result, the predicted spreading dynamics are very robust – no reasonable change of any parameter yielded anything but an initial $\sim t^{1/2}$ spreading.

6. A five-level subdivision of the icosahedron is required to accurately model the high curvatures occurring when the cell is fully spread out – see section 4.2.3. Using a lower order triangulation yields very similar initial spreading dynamics, but fails to reproduce the final spreading radius of the cell.

7. The model is general enough to allow for simulations in more complex situations – cells interacting with smooth shapes, cells interacting with other cells, and so forth. It is also well suited for inclusion of cytoskeletal elements (such as the actin network, microtubules, nucleus) in a discrete way.

The modelling technique described in this work has a number of limitations:

- The mesh that is used needs to be refined enough to capture the smallest structures/curvatures that are of interest in the system. This results in comparatively expensive simulations or the additional complication of re-meshing in appropriate regions.

- The linear approximation for the dissipative forces in the equation of motion must be regarded as a first-order approximation of a very complex phenomenon: e.g. (Leckband and Israelachvili 2001) notes, that the dissipation upon contact is a time-scale dependent effect, which indicates the limited applicability of the “viscous friction constants” (γ_n, γ_t). This is the reason why not both observed spreading curves in the experiments by (Hategan, Sengupta, Kahn, et al. 2004) and (Cuvelier, Thery, Chu, et al. 2007) could be matched with the same values for γ_n and γ_t. For cell spreading that happens at the same time scale with similar materials involved, we expect the constants to be very similar.

- The current state of the model does not describe the phenomena affecting late cell spreading which are relevant for other cell types. The dynamics of this active spreading are regulated by cellular processes such as actin polymerization, formation of focal adhesion complexes and stress fibres.

4.3.2 Understanding initial cell spreading

Finally, regarding the initial dynamics of cell spreading, we find:

1. The “universal” (Cuvelier, Thery, Chu, et al. 2007) $\sim t^{1/2}$ power law behaviour of initial cell spreading is found consistently. Moreover, this behaviour is very robust to changes in model parameters, because it is caused by geometrical properties of the spreading cell. From the simulations we observe that this first spreading phase is characterized by the absence of tension in the cortical membrane. Since almost no forces are present there, little energy is stored elastically or dissipated in the cortical shell. To understand the $t^{1/2}$ power-law for the radius of contact, we follow the analysis presented by (Cuvelier, Thery, Chu, et al. 2007). We conclude that the energy dissipation rate is mainly affected by contact dissipation due to friction. It is therefore proportional to $\gamma_n a^2 \left(\frac{\mathrm{d}a}{\mathrm{d}t}\right)^2$, which can be balanced by the adhesive power. This adhesive power (rate of adhesion-energy gain) is proportional to $Wa\frac{\mathrm{d}a}{\mathrm{d}t}$, yielding for the trivial integration (ignoring all constants)

$$a \sim \sqrt{\frac{2W}{\gamma_n} t^{1/2}}, \tag{4.31}$$

which explains (assuming the given approximations) the characteristic $\sim t^{1/2}$ power law dynamics for the contact radius a. Summarizing, the total energy dissipation per area which is coming into contact with the substrate is constant at this very early stage of cell spreading, yielding the observed dynamics.

2. The first, “fast” slope can only be maintained until the cell’s cortex is under tensile stress: In that case, spreading further dissipates more energy – the stretching deformation causes viscous dissipation in the dashpot-like elements, while some is also stored in the (still weak) FENE-like potential. (Cuvelier, Thery, Chu, et al. 2007) show for several cell types, that in this region a second power law $\sim t^{1/4}$

can be found, but it is least pronounced in the experimental RBC data (see figure 4.6(a)). From the simulations we observe that there is no clear second power-law regime, but merely a slowing down of the spreading.

3. The final spread-out phase is characterized by a high tensile, in-plane stress in the spectrin-phospholipid cortical shell. This stress is caused by the balance between adhesion forces that occur at the edge of the spread out cell (in the flattened out centre, repulsive and adhesive forces balance out and the contact force is very low) and the FENE connections approaching their maximum extension in the upper spherical cap. The adhesive tension at the edge also causes the membrane-substrate interface to be compressed in a radially inward direction. For a substrate that has shear elasticity, the model therefore predicts that the substrate would deform in a radially inward direction. This prediction is in good agreement with experiments using Traction Force Microscopy (Wang, Ostuni, Whitesides, et al. 2002) – although these experiments are more concerned with the late, active cell-spreading state.

4. Most of the energy dissipation during initial cell spreading occurs due to contact dissipation. The simulations indicate that for a red blood cell, no irreversible deformation in the cortical shell is required to reproduce the experimentally observed spreading dynamics. This means that, should we pull back the cell from the substrate, the cell would re-gain its initial shape, as the equilibrium lengths of the FENE connections and the equilibrium angles of the bending connections have not been changed. This is contrary to the simpler, conceptual model proposed by (Cuvelier, Thery, Chu, et al. 2007), which relies on the dissipative "flow" of the cytoskeleton for energy dissipation.

Although the model as shown is restricted to RBC spreading dynamics, we expect that these conclusions can be generalized to other cell types: The same key mechanical components are present in other systems as well, and despite the fact that other cells' cytoskeletons are more complex and the cells can dissipate energy through "active biological processes", the initial cell spreading phase will still be characterized by contact dissipation. Eventually, stress in the membrane / cortex will build up as well and through this, the cell will dissipate energy in the entire cortical shell. However, it is possible that this dissipation involves irreversible deformation in the cortex.

4.4 Possible extensions for cells with a more complex cytoskeleton

4.4.1 Random network of actin cortex

The actin cortex could be represented by a random network of internal nodes. In the following example, positions of the internal nodes are chosen randomly, with the restriction that two nodes can never be closer to each other than a given distance[2]. Next, each internal node i is connected with the N_c - typically six or eight - closest internal or cortex nodes, thereby obtaining a random network. The advantage of this detailed approach is that the obtained network shows deformations that are very similar to the behaviour of an actual actin network. The parameters of the individual "coarse-grained actin connections" can be chosen (using a curve-fitting iterative algorithm) in such a way that realistic bulk behaviour of a reconstituted actin network cross-linked with scruin is captured, see figure 4.9. If such a network is added to the RBC model, relatively low initial spreading can be observed: see figure 4.10(a).

4.4.2 Other elements of the cytoskeleton

Additional elements of the cytoskeleton may be added as well, obvious candidates being radial struts from a central location ("centrosome") representing the microtubuli, whereas the nucleus could be represented by a comparatively stiff sphere which interacts elastically with any node of the cytoskeleton or cortex. Figure 4.10(b) shows a trial with these structures in addition to the described actin cortex. It is very difficult to validate the different elements' mechanical contributions and especially their interactions with data from the literature, but recently interest in these interactions is growing (Barreto, Clausen, Perrault, et al. 2013), and more and more refined measurement techniques become available – see also chapter 2.

4.5 Conclusions on the use of the deformable cell model for IBM

In this chapter an extension to the well-known method of IBM has been explained. In cooperation with B. Smeets and on the basis of well-founded mechanical models, the author developed a deformable cell model that captures the adhesive interaction

---

[2] This distance is chosen so that the volume per node, where other nodes are excluded, is 5 % of the total volume divided by the number of nodes.

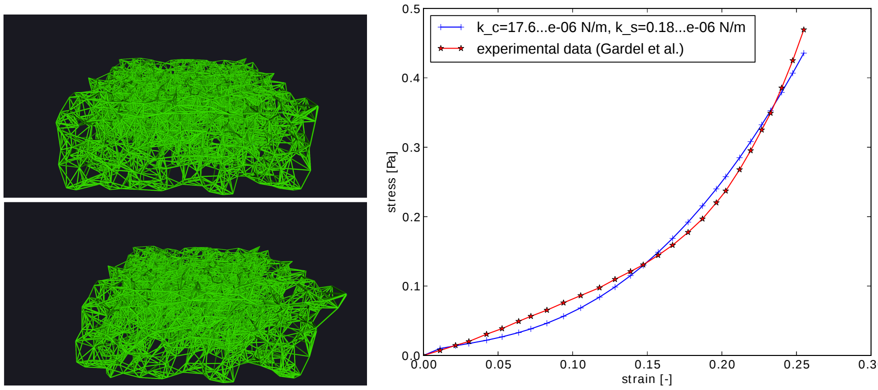

(a) (b)

Figure 4.9: Shown in (a) is a view on the initial and final step of a shear-test for the random network representation of the cytoskeleton. (b) A two-parameter fit for the compressive (k_c) and stretching (k_s) stiffness yields sufficiently realistic results compared to experimental data used by (Van Oosterwyck, Rodríguez, Doblaré, et al. 2012), originally obtained by (Gardel, Nakamura, Hartwig, et al. 2006). Here the actin monomer concentration was 8 mM and the ratio of actin monomer to cross-linking protein (scruin) concentration was 3 %.

and deformation of a cell spreading on an adhesive surface. This allows for a deeper understanding of the mechanisms which dictate initial spreading dynamics: In particular, the role of energy dissipation upon contact as a main determinant for spreading speed is emphasised. In addition, we show that no irreversible deformations of the cell are needed to explain the observed spreading dynamics.

Clearly, the full potential of the underlying methodology has yet to be harnessed, but the explanation of what happens when a cell first comes into adhesive contact with its substrate already adds substantially to the knowledge and methods available to the field.

The way in which the model accurately calculates contact interactions for arbitrarily shaped cells is promising in several regards:

- The method can be integrated seamlessly with the traditional IBM solver, generating a much more detailed picture of what happens mechanically at the level of an individual cell.

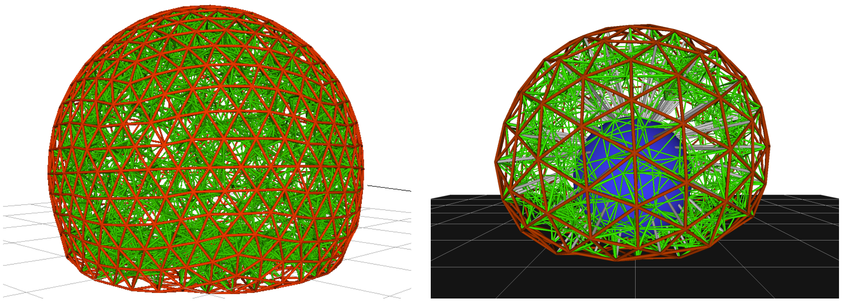

(a) Actin cortex only (b) Actin cortex, microtubuli, nucleus

Figure 4.10: View on final state of initial spreading with a random “actin” network cortex (a) and a combination of actin cortex, microtubuli and nucleus (b) (final stages).

- The method can be used to explore the dynamic contributions of cytoskeletal elements to the mechanical responses of a cell.
- The internal elements can be made “active”, thereby offering the possibility of exploring mechanistic models for active cell motion, be it active spreading, sensing, or locomotion.

Chapter 5

Software design and computational aspects

The Zen of Python

Beautiful is better than ugly.
Explicit is better than implicit.
Simple is better than complex.
Complex is better than complicated.
Flat is better than nested.
Sparse is better than dense.
Readability counts.
[. . .]

Tim Peters

Introduction

Writing a large software framework is a somewhat daunting task for a PhD student with some programming skills, but only rather limited software engineering experience. Luckily, the existing DEMeter++ framework, which had been developed in the group at MeBioS for nine years at the start of this project, could be taken as a guideline and reference. The DEMeter++ -Bio extension largely designed and implemented collaboratively in the present work caused some modifications and extensions in the basic framework – in addition to a large number of new modules. The collaborative effort of the people writing the major part of the source code lead to considerable synergies; typically programming problems could be solved efficiently with the help of the other developers.

While some early designs and implementations had to be abandoned (e.g. the first version of the Conjugate Gradient solver, and an explicit Runge-Kutta-type time-integrator which updated the time-step), a large portion of the code produced has proved to be useful in the latest DEMeter++ -Bio software, which shows the great flexibility of the underlying library as well as the excellent guidance given by the group. While the nature of this software development model as a team makes it impossible to distinctly separate individual contributions, all aspects described in this chapter apart from the pure SPH implementation have been to a large extent developed and implemented in this PhD project.

While the novelty of the algorithms employed and the idea of a comprehensive software platform are at the state-of-the-art, several details implemented in this platform are truly novel and cannot be found in any other software. Especially the broad perspective of using several particle-based methods, also in combination, may be unique.

To achieve the results described in the previous chapters (3 and 4), a very flexible, highly efficient software platform has been developed to investigate bio-mechanical and biophysical interactions at the meso-scale. There are already several computational tools available to investigate many cellular interactions in a mesh-less way (Hoehme and Drasdo 2010; Holcombe, Coakley, and Smallwood 2006; Mirams, Arthurs, Bernabeu, et al. 2013). In addition to the results presented, the aim of the software platform DEMeter++ -Bio is to provide a general particle-based simulations platform which allows to encompass and combine several different approaches towards mechanistic simulations of tissue. The platform is based on the successful DEMeter++ software (Tijskens, Ramon, and De Baerdemaeker 2003; Vanmaercke, Tijskens, Van den Eynde, et al. 2011) that is under continuous development in the group.

Investigating the interactions of cells leads to several interesting computational problems which can be addressed in a particle-based approach: cell mechanics and forces generated by the cells, low-Reynolds number flows as well as diffusion of highly diluted biochemical signals, amongst others. The research questions encountered often require treatment in three dimensions and with a large number of interacting entities, which calls for efficient solution techniques despite the ever-increasing computational power available.

At the same time, a researcher often works on very specific problems which deal with unique geometries and settings. A general software platform must therefore be easily adaptable to the researchers' needs and requirements, imposing as little restrictions as possible on the modelling options. Despite this flexibility, using the software must provide a consistent user interface which can be quickly understood and is easy to work with.

5.1 Simulation work-flow

The general work-flow using DEMeter++ -Bio is that a simulations with all its actors and geometry is set up using python tools and possibly computer automated design software such as FreeCAD[1]. In the second step DEMeter++ -Bio "runs" the simulation for a specific period of (simulated) time, and finally the results are analysed using again python tools and visualization front-ends such as Mayavi[2] and Paraview[3].

5.2 Implementation choices

DEMeter++ -Bio addresses these issues by creating a very modular and extensible design in C++ , which is accessed via a python interface. The C++ algorithms ensure high flexibility and modularity for the developers in writing near-optimally efficient programs. To ascertain highest quality as well as the latest developments of the underlying libraries, the use of libraries is restricted to the C++ standard template library and the boost[4] libraries. The design is object oriented and uses generic programming wherever appropriate, mostly through template (meta)programming (but to a lesser extent also using preprocessor macros) to minimize code duplication.

From a researchers' perspective, most of their models' implementation should only require python development, although for added flexibility or efficiency reasons C++ development may become necessary to a smaller extent.

5.2.1 Key aspects of the software

Given the strategic aim of the software, the source code itself cannot be exhaustively commented upon, but some choices of major importance for usability and efficiency of the software are highlighted in the following.

---

[1] `http://www.freecadweb.org/`

[2] `http://code.enthought.com/projects/mayavi/`

[3] `http://www.paraview.org/`

[4] `http://www.boost.org/`

Contact Detection

The most performance-critical aspect of particle based simulation software is the Contact Detection (CD) algorithm. The reason is quite obvious, understanding that it is not clear a priori which cells' or particles' interactions need to be calculated at any given time. If one simply tries all possible combinations (brute-force), the algorithm scales as N^2 in the number of particles N. Already for relatively few particles this becomes extremely costly. So, instead of the brute-force algorithm, a (three-dimensional) grid is overlaid over the space in which particles are present, and interactions are only calculated between particles in neighbouring grid-cells, thereby reducing the scaling of the problem to N. Of course, mesh creation itself incurs an additional cost, but it typically compares favourably for $N \geq 30$ (in the yeast simulations, see chapter 3)[5]. The algorithm can be further optimized if the particles' sizes encompass a big range – then a multi-grid CD algorithm (He, Dong, and Zhou 2007), which takes advantage of the different "reach" of the particles, will generally outperform a simple grid-based algorithm. In fact this multi-grid algorithm (He, Dong, and Zhou 2007) and a restricted version for a single grid has been implemented and tested for DEMeter++ -Bio.

Independent of whether the (multi-)grid-based or brute-force CD algorithm is used, it is crucial that the detected contacts are stored between time-steps. For some contact force models such as the JKR model this is even explicitly required, since depending on whether the contact had been established before, there might be a residual adhesion force even when the particles have come apart so much that the apparent overlap becomes negative (obviously, the force must vanish for particles that have not yet been in contact and which also do not touch). This information about the contact between particles is stored in the "contact state", which is kept in memory for every interaction between two particles or cells.

Conjugate Gradient method

A central aspect of code that was specifically written for IBMs is the CG method, which iteratively solves the equation of motion (see equations 3.1, 4.29) for the velocities, given the friction constants and the forces on all particles. It has proven to be very advantageous to use the "contact states" as storage for the matrix Γ, since it avoids unnecessary access to yet another data structure, and the access-pattern is very similar. Only the diagonal elements, which also contain the fluid drag, have to be treated specially.

---

[5] Many implementations prefer an $N \log N$ scaling, which may yield a smaller linear factor and therefore be better at medium-sized problems.

The algorithm itself is fairly simple[6], relying mostly on matrix (Γ) - vector ($\mathbf{v}$) multiplication to converge to a solution of a given precision (Barrett 1994; Heath 2005). There are two additional complications imposed by DEMeter++ -Bio: Firstly, to appropriately represent different types of particles (e.g. distinct cell types or cells and micro-beads, see figure 5.3), they may be kept in separate memory, making it necessary to construct a meta-array of velocities ($\mathbf{v}$) and forces ($\mathbf{F}$) as well as a meta friction-matrix (Γ). Secondly, the parts of a deformable cell which make contact (the rounded triangles) do not move as such – the forces have to be distributed to the nodes, which then move accordingly. Therefore, the friction, which is determined also for the contacting particles, has to be like-wise transferred to the nodes' friction matrix Γ, which is accomplished by an intermediary step. A very similar procedure is applied for "ghost-particles" which can be used to represent periodic boundaries. This has been adequately solved relying on the existing data structures in DEMeter++ . Interestingly, this technique allowed for easy translation to the Non-Newtonian Smoothed Particle Hydrodynamics (NSPH) (see section 5.3.3) algorithm.

Python tools

As indicated in the work-flow section (5.1), for pre- and post-processing we rely on small python programs. These are quick to write and test and since the computational complexity required is generally much lower than a full particle-based simulation, the overhead incurred by using an interpreted language is less important. As such, the python tools to set up complex simulations e.g. with deformable cells are an integral part of the software package developed for DEMeter++ -Bio. Likewise, the post-processing tools, which have undergone several evolutionary transformations, are of major importance to quickly extract the needed data and representations (e.g. graphs and figures) from the simulations. It has proven important that simulation results be kept as dedicated files, since often only in hindsight an analysis may become relevant which has to be applied to the data. Using blender[7], full renderings of simulation results are possible – see figure 5.1.

5.2.2 Documentation and sharing of code

A crucial part of any computer interpreted or compiled source code is documentation for human readers. DEMeter++ is generally documented in its header files at the level of classes and free functions. To make this documentation more consistent and user-friendly, doxygen-style[8] comments are used for the parts added in DEMeter++ -Bio,

---

[6] The CG algorithm can be expressed in less than 15 lines of pseudo-code (Barrett 1994).

[7] `http://www.blender.org/`

[8] `www.doxygen.org`

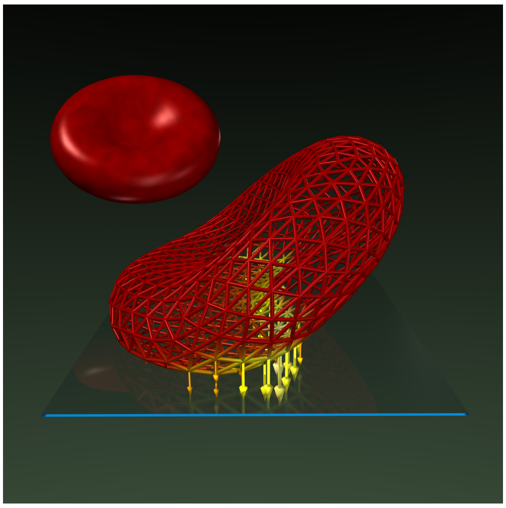

Figure 5.1: An example of a rendered red blood cell as it is spreading on a flat substrate. Arrows and colours represent the strength of the conservative forces at the nodes.

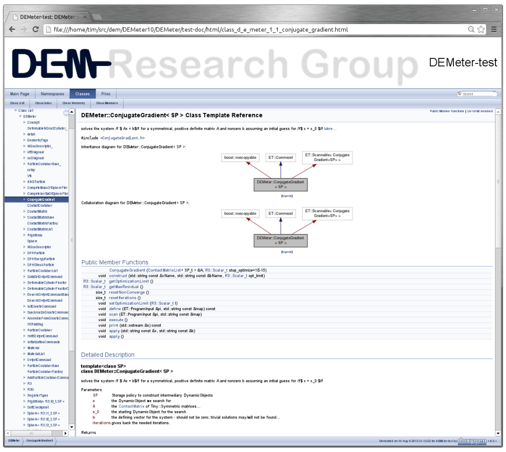

DEMeter::ConjugateGradient< SP > Class Template Reference

solves the system /f $ Ax = b$/f for a symmetrical, positive definite matrix A and nonzero b assuming an initial guess for /f$ x = x_0 $/f More...

`#include <ConjugateGradient.h>`

Inheritance diagram for DEMeter::ConjugateGradient< SP >:

Collaboration diagram for DEMeter::ConjugateGradient< SP >:

Public Member Functions

	ConjugateGradient (ContactMatrixList< SP_t > &A, R3::Scalar_t stop_optimize=1E-15)
void	construct (std::string const &xName, std::string const &bName, R3::Scalar_t opt_limit)
R3::Scalar_t	getOptimizationLimit ()
R3::Scalar_t	getMaxResidual ()
size_t	resetNonConverge ()
size_t	resetIterations ()
void	setOptimizationLimit (R3::Scalar_t l)
void	define (ET::ProgramInput &pi, std::string const &map) const
void	scan (ET::ProgramInput &pi, std::string const &map)
void	execute ()
void	print (std::ostream &o) const
void	apply (std::string const &x, std::string const &b)
void	apply ()

Detailed Description

template<class SP>
class DEMeter::ConjugateGradient< SP >

solves the system /f $ Ax = b$/f for a symmetrical, positive definite matrix A and nonzero b assuming an initial guess for /f$ x = x_0 $/f

Parameters

SP	Storage policy to construct intermediary DynamicObjects
x	the DynamicObject we search for
A	the ContactMatrix of Tiny::Symmetric matrices...
x_0	the starting DynamicObject for the search
b	the defining vector for the system - should not be zero; trivial solutions may/will not be found...
iterations	gives back the needed iterations.

Returns

Generated on Fri Aug 9 2013 21:13:22 for DEMeter-test by doxygen 1.8.3.1

Figure 5.2: An example html page documenting the implementation of the conjugate gradient method.

and some of the DEMeter++ documentation was re-written to follow that style. This has the advantage that the documentation can be extracted from the pure source code and be viewed independently, e.g. as a html file, see figure 5.2.

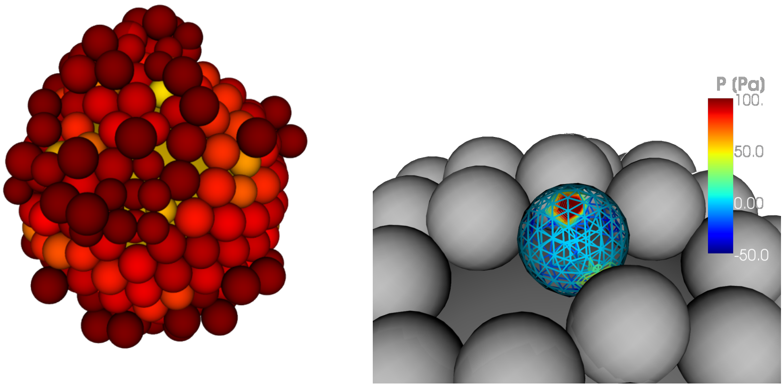

(a) Mechanical stress on microbead (b) IBM with deformable cell

Figure 5.3: Views on stresses of cells grown on microcarriers; (a) depicts a result from (Smeets, Odenthal, Tijskens, et al. 2013) (brighter color means higher compressive stress) and (b) shows a simulation, where a single cell was replaced by a deformable cell and the local stresses on that cell are shown.

Documentation for the python interface is more complete and easier to access for the user, as the (boost-) python built-in documentation tools are used: when a python function or class is declared, a documentation-string can be easily added directly in the source code which is then immediately available from the python interface for the user. Documentation of the installation procedure can be found in appendix G.

To facilitate code-sharing and co-operative programming, a version control system called “subversion”[9] was set up and used in the context of DEMeter++ -Bio.

5.3 Modelling techniques currently available

The modelling techniques currently implemented in DEMeter++ -Bio in addition to the traditional Discrete Elements Method (DEM) are threefold (5.3.1, 5.3.2 and 5.3.3).

5.3.1 Individual-cell based models

IBMs in which the cells’ mechanical and biological responses are investigated; recent advancements were made in elucidating basic socio-evolution in yeast (see chapter

---

[9] http://sourceforge.net/p/forge/documentation/svn/

3) as well as a more general investigation of an important three-dimensional cell culturing technique for tissue engineering: cell growth on microcarriers (Smeets, Odenthal, Tijskens, et al. 2013). In the latter case it was found that the mechanical microenvironment for different cells on the beads becomes highly inhomogeneous (see figure 5.3(a)) when the cells reach confluency on the bead, and we speculate that this might lead to an amplified inhomogeneity in the cells' biological responses.

Extending the applicability of IBMs, furthermore a mechanistic model of a deformable cell was developed, investigating how the cell interacts with its micro-environment. This led to interesting insights into initial cell-spreading (see chapter 4, (Odenthal, Smeets, Van Liedekerke, et al. 2013)), as well as deeper insight into the local differences of mechanical stresses incurred by cells growing on microcarriers (see figure 5.3(b)).

5.3.2 Smoothed particle hydrodynamics

SPH is a method to investigate fluid flows and responses. It was employed using DEMeter++ -Bio to elucidate the micro-mechanics of plant cells, combining the solution of the responses of the fluid phase with a cell wall interaction model (Van Liedekerke, Ghysels, Tijskens, Samaey, Roose, et al. 2011; Van Liedekerke, Tijskens, Ramon, et al. 2010). Additionally, viscoelastic solids can be implemented using SPH which forms an interesting basis for extra-cellular matrix simulations.

5.3.3 Non-Newtonian smoothed particle hydrodynamics

Expanding on the SPH method for creeping flow systems as most commonly encountered in cell based systems, a new methodology was developed using DEMeter++ -Bio called NSPH (Van Liedekerke, Smeets, Odenthal, et al. 2013). This method helped to elucidate e.g. the complex influence of flow on a red blood cell's shape in a computationally very efficient manner. Figure 5.4 demonstrates the exceptional agreement between the new computational method and the well-known SPH solution of the shape deformations imposed on an RBC in Poiseuille-flow. The speed-up realized by the NSPH method in this particular example was a factor of 2000.

5.4 Multi-scale methods

In the past, multi-scale methods have been devised in the group on the software side on an ad hoc basis with the specific problem in mind (Ghysels, Samaey, Tijskens, et al. 2009; Van Liedekerke, Ghysels, Tijskens, Samaey, Roose, et al. 2011). Using the newly

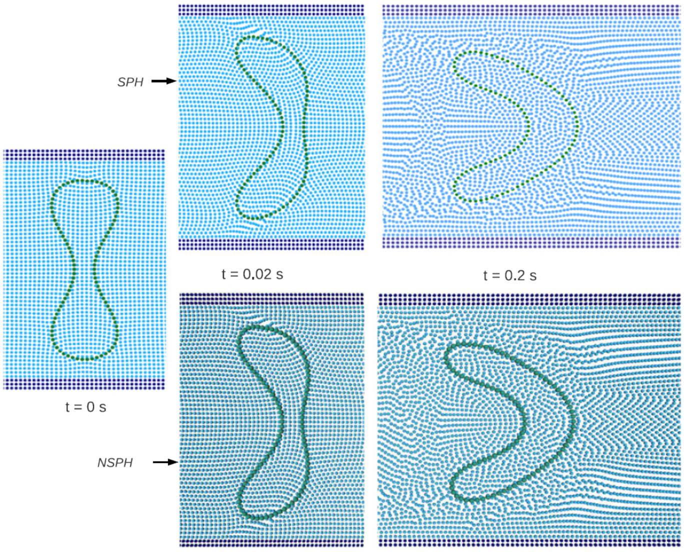

Figure 5.4: Comparison of the solution of an RBC model in Poiseuille flow between the SPH (top) and the NSPH (bottom) methods, from (Van Liedekerke, Smeets, Odenthal, et al. 2013).

developed python interface, a more structured approach to even broader multi-scale simulation approaches becomes attainable.

A general interface (see figure 5.5) can be devised quite simply from the cell/agent-based model's point of view; it must be able to:

- query from the PDE-grid which grid-cell(s) is/are relevant for each agent,
- query the current time and PDE-time-step (i.e. duration for which it should run)
- obtain either the concentration(s) or a vector (of stresses) from the corresponding grid-cell(s).
- set newly computed stresses or concentrations in the PDE-model
- solve a (possibly custom) Ordinary Differential Equation (ODE) whenever needed.

If a PDE-ODE multi-scale model is required, a solution could be a dummy agent-based model, which only updates concentrations.

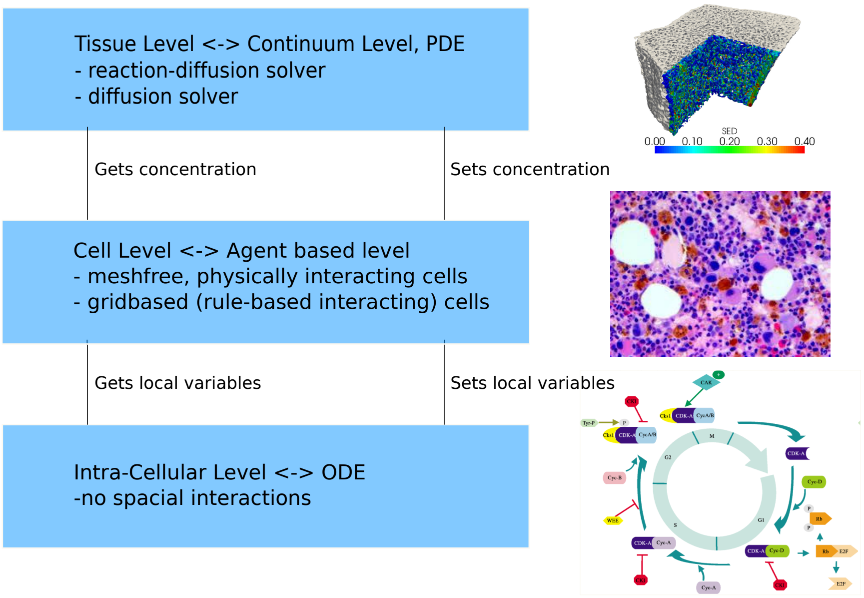

Figure 5.5: Schematic of multi-scale modelling framework with an example application in bone tissue engineering for illustration purposes.

Thanks to the comparative ubiquitousness of python interfaces for successful ODE and PDE libraries, this can be achieved from the python side without having to adapt the C++ source code with only minor losses of computational efficiency.

5.5 Conclusions on software development

The particular strength of the software platform presented here lies in the comparatively easy combination of the techniques of classical IBM, the deformable cell model, SPH, NSPH as well as ODE solvers in a multi-scale model. Apart from the possibility to loosely couple DEMeter++ -Bio to a continuum solver through python, direct coupling of the continuum (N)SPH methods to the IBM is possible and promises highly efficient computations. While there has been a particular emphasis on mechanically correct simulations, more and more biological information can be included in future endeavours by using the multi-scale scheme explained in the previous section. Another interesting example is the coupling of the deformable cell model with an algorithm to solve fluid-flow using the immersed boundary method (under development), which is possible thanks to the modularity of the implementation.

One of the additional synergies between the different methods is that the majority of source-code can be reused fully or with marginal modifications, leading to good cross-checking of implementations by different users with distinct goals. In other words, these quite diverse methods rely in parts on common algorithms – most importantly contact detection. Only the design as a highly modular, integrated platform makes it possible to efficiently combine the different methods.

Chapter 6

Conclusion and future directions

> There is a theory which states that if ever anybody discovers exactly what the Universe is for and why it is here, it will instantly disappear and be replaced by something even more bizarre and inexplicable.
> There is another theory which states that this has already happened.
>
> Douglas N. Adams

To draw general conclusions about the work accomplished during the research for this thesis, the goals described at the outset (section 1.3) are revisited. In addition to the plans for the future mentioned in the context of each of the goals, a dedicated section points out concrete directions for future research in the field.

6.1 Development of a flexible software platform for physical simulations of biological systems at the cellular scale

During the development of the computational framework for IBM, roughly 57 k lines of source code have been written by the author[1], 42 k of which in C++ and 15 k in Python. This effort forms the basis for a considerable extension of the DEMeter++

---

[1] This number is less exact as could be hoped for, since Bart Smeets produced the majority of his code under the user-name TimO. Therefore, the number of lines reported is half of the sum of the combined

platform to adapt it for models which are useful at the cellular scale. In particular, methods including classical IBM, the deformable cell model, SPH, NSPH as well as ODE solvers in a multi-scale modelling environment have been developed in a common mesh-free framework.

While such a software project is by design never "finished", a substantial amount of the platform has reached high maturity as evidenced by the fact that it could be directly used by other researchers (B. Smeets, P. Van Liedekerke, T. Heck, A. Rashidi and others). Currently, a new version of the basic DEMeter++ platform is in testing and a major amount of the code written will be transferred in the near future, improving maintainability, extensibility, usability and computational speed.

This platform will be used in future endeavours which build on the results obtained in this work, especially in the research project MAtrix[2] headed by Hans Van Oosterwyck and in the ongoing collaboration with the interdisciplinary research group Prometheus, the division of Skeletal Tissue Engineering at KU Leuven[3]. These two main collaborations established on the basis of this modelling platform already point out the capability of these models to be used both in "fundamental" as well as "applied" research leading to concrete improvements of e.g. cell culturing schemes (Smeets, Odenthal, Tijskens, et al. 2013). In addition, close ties have been developed to the research group of "multi-cellular systems biology" at IZBI, Leipzig (Germany) and INRIA, Rocquencourt (France)[4] to achieve an exchange with the CellSys platform. As these collaborations show, interest in the developed platform is high and it can be concluded that the goal to develop a flexible software platform for mechanically sound, physical simulations of biological systems at the cellular scale has been achieved by the work described in this thesis.

6.2 Establishing experimental protocols to determine the cell mechanical parameters

The second specific goal – establishing experimental protocols to determine the cell mechanical parameters which are crucial for the models – has been reached as well. In particular, the measurements of yeast stiffness yielded interesting results, since it can be concluded from the observed values that cell-sorting in a system with those two yeast strains (an adhesive, FLO^+ and a non-adhesive flo^- strain) is not caused

---

line-count of B. Smeets and T. Odenthal. In any case, solely counting the produced lines of code is a poor measure of software development productivity.

[2] European Research Council starting grant (FP7/2007-2013)/ ERC Grant Agreement n° 308223, `www.kuleuven.be/eu/erc/2012/oosterwyck.html`

[3] `www.kuleuven.be/prometheus/`

[4] `ms.izbi.uni-leipzig.de/`

by differences in Young’s modulus. It has been shown how cell’s Young’s moduli and adhesion energies can be experimentally obtained in measurements with MA and AFM. Both techniques can be further developed to more efficiently arrive at the observables of interest.

6.3 Application of individual cell-based models to relevant research problems

The model developed for the specific research questions of cell-sorting in yeast could substantiate the hypothesis of sorting due to differential adhesion in combination with the measurement of Young’s modulus of the yeast strains (Odenthal, Smeets, Christiaens, et al. 2012).

The work on cell cultures for bone tissue engineering was carried out in close collaboration with and mainly pushed forward by Bart Smeets. This line of research produced very interesting results on the mechanical stresses experienced by osteochondroprogenitor cells expanded in micro-carrier culture (Smeets, Odenthal, Tijskens, et al. 2013): when the cells reach confluency on the micro-carriers, stresses generally peak, but the model predicts an unexpectedly large heterogeneity of these compressive stresses. Since it is known that cell fate may be influenced by the stresses cells experience through “mechanotransduction” (Huang, Kamm, and Lee 2004; Ingber 2006), this could be a reason for increased biological heterogeneity of the cell population after this expansion phase. These results indicate that the third goal as formulated in the introduction – to apply the IBMs to relevant research problems – has been achieved. Moreover, the new method for deformable cell models allows for a deeper understanding of initial cell-spreading dynamics: Both the role of energy dissipation upon contact as a main determinant for spreading speed as well as the absence of irreversible deformations of the cell have been pointed out for the first time (Odenthal, Smeets, Van Liedekerke, et al. 2013).

6.4 Advancing the state of the art in simulation techniques at the cellular scale

Finally, we extended the modelling tools available to the field – fulfilling the fourth specific goal – by developing the NSPH method (Van Liedekerke, Smeets, Odenthal, et al. 2013), allowing to efficiently simulate (cells in) low-Reynolds number flow with deformable boundaries.

Furthermore, the newly developed deformable cell model for IBM with its general, theoretically well-founded treatment of adhesion should open up new possibilities for more detailed simulations of a cell's interaction forces. This is not only required for proper analysis of passive spreading, but should also improve models for active spreading and cell-locomotion. The deformable cell model is also a versatile method to investigate different models for the cytoskeleton (see section 4.4); this aspect should be further pursued based on concrete experimental data. In my point of view, this model will be most fertile for future endeavours in investigating numerous aspects of cell-cell and cell-matrix interaction and cell motion. Additionally, to incorporate fluid flow in a general and efficient as well as very precise way, we are investigating the combination of said model with the immersed boundary method. This promises highly accurate simulations of cells in flow which come into contact with other cells or substrates such as RBCs squeezing through micro-vasculature.

6.5 Opportunities for future research

There remains a considerable body of work for physically sound models at the cellular scale. On the one hand, further fundamental research based on the developed methods and platform may be most fertile in

- exploring the dynamical contributions of cytoskeletal elements to the mechanical responses of a cell,
- investigating mechanisms of active cell motion both on a substrate as well as in a three-dimensional environment,
- elucidating cellular mechanical interactions with the environment, especially when dynamic deformations and adhesion play an important role, e.g. blood-clots in micro-vasculature or leukocyte extravasation, but also initial formation of biofilms,
- further analysing interactions with the fluid-flow to find out how cells may "feel" the flow and actively respond to it,
- using SPH methods to unravel effects of e.g. shock-waves or heat-waves impinging on cellular tissue,
- up-scaling the described models to find emergent phenomena on cell agglomerate level or in functional sub-units of organs, e.g. endochondral ossification or wound healing.

Obviously, this list is not exhaustive, since there will always be a need for additional in-depth research of specific mechanisms (see also the introductory quotation); I believe that starting with physical models from a cellular scale opens a particularly interesting door to fundamental biological research.

On the other hand, direct applications may be derived from the established technologies (also by other researchers in the field); no attempt was made to compile a complete list of applied research directions, since the biomedical field is far too vast for a single researcher to have a complete overview. Some examples could be:

- Biofilm formation dynamics on medical devices could be predicted,
- Cell culturing methods, in particular in three-dimensional cultures can be modelled and optimized
- Cell-seeding in perfusion bio-reactors can be optimized using the simulation techniques described,
- Effects of cell-behaviour altering drugs can be elucidated, e.g. drugs inducing cell death for cancer treatment.

These items still represent quite broad modelling applications which would need to be narrowed down to the specific goal of research.

Overall, it could be shown that the foundations have been laid to tackle numerous challenges in the field of cell mechanical models, and that by applying those well established physical theories in biological systems, be it for measurements or in modelling system dynamics, we can significantly expand our knowledge and understanding of many aspects of the systems' behaviour.

Appendix A

Protocol for Micropipette Aspiration as established in Exeter

Following a research stay at the University of Exeter under the supervision of Sharon Jewel, PhD. and Prof. Peter Petrov, we established the following protocol for Micropipette Aspiration.

A.1 List of materials

Materials for micropipette preparation:

- Micro pipette puller (SUTTER)
- Glass capillaries
- Storage box for prepared micropipettes
- Glass with pipette holder (and buffer)...
- Microfill syringes with filter (World Precision Instruments)
- Micro-manipulator
- Heating wire on microscope plate and power supply

- Rudimentary pressure system (syringe and tubing)

Materials for chamber preparation and cell suspension:

- Buffer
    - H_2O
    - Phosphate Buffered Saline (PBS)
    - Bovine Serum Albumin (BSA) (1 g/l)
    - Scale
    - Magnetic stirring plate
- Cells in suspension
- Centrifuge, centrifuge tubes
- Pipette(s) (100 µl)
- Glasses, glass with scale/volume measure
- Parafilm
- Scissors
- Heating stove
- Microscope slides & cover slid (chamber)

Materials for a MA experiment:

- Microscope
    - brightfield, phase contrast
    - 10 x, 40 x magnification objective
    - x-y table to move the sample/ heating wire
- Pressure system
    - Filling/rinsing syringe
    - Reservoir syringe (open!)
    - Tubing
    - Three way valve
    - Hight adjustment of reservoir with scales (down to micron scale)
- Micro-manipulator

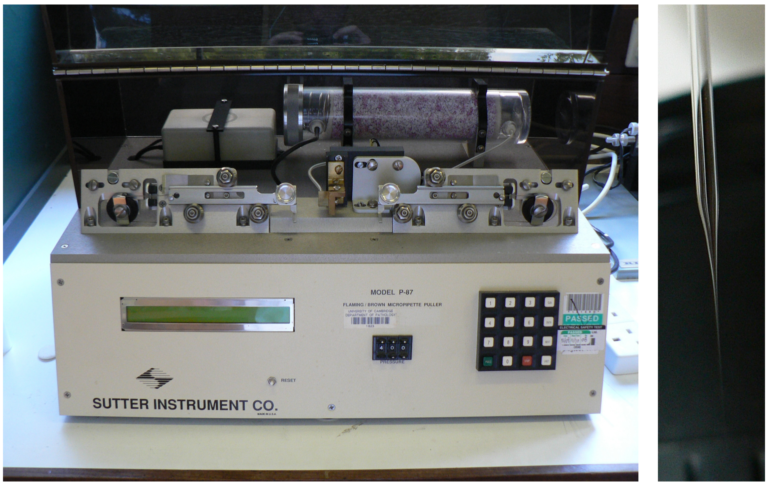

(a) Micropipette puller

(b) Micropipette

Figure A.1: Micropipette puller to produce micro-pipettes with defined tether shape and tip radius (a). Micropipette with long tether and approximately 1 µm radius (b).

A.2 Preparing Micro-Pipettes

- Start from glass-capillaries with $d_{out} = 1\,\mathrm{mm}$
- Automatic puller with variable programmes depending on glass & wanted shape
- Parameters: Heat, pulling force, velocity, cooling air flow (repeat)

A.2.1 Prepare tip

- BF microscope (10 x)
- Stick into molten glass bead
- Cool bead → retracts → breaks off tip cleanly

A.2.2 Filling pipettes with buffer

- Capillary forces to fill tip, $t \sim 10\,\mathrm{min}$ (figure A.3)

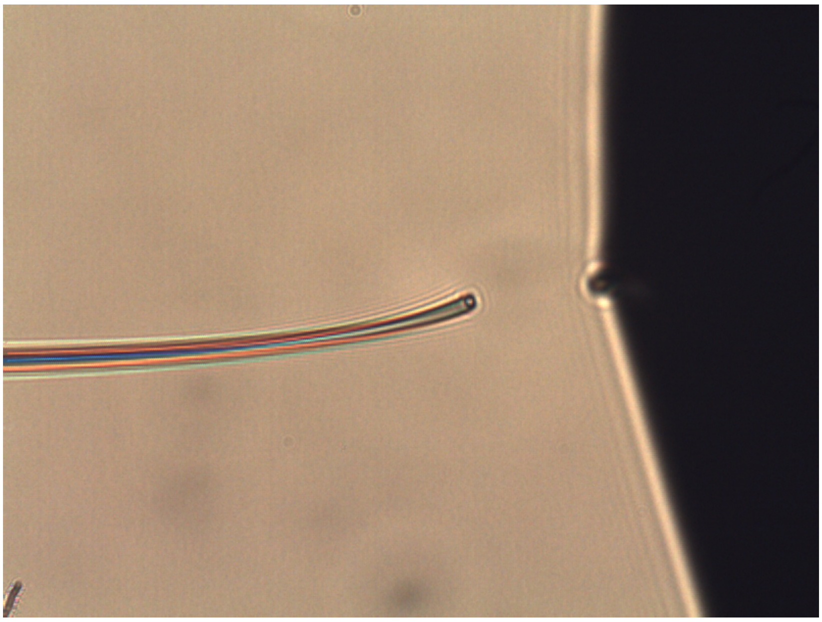

Figure A.2: Preparing tip of micro-pipette by abrupt cooling of molten glass bead (right side of frame), breaking off a clean, straight and smooth tip.

- Syringe $d_{out} < 0.5\,\mathrm{mm}$ fill pipette
- Check under microscope

Coping with Bubbles

- Naked eye: let rise to top
- Close to tip: heat tip (heating wire)
- Small, in between: pull out with pressure system
- Else: throw pipette away...

A.3 Preparing Chambers & Cell-suspension

To build an experimental chamber (figure A.4), put

Figure A.3: Buffer-filled glass to store filled pipettes and to fill tip of micro-pipettes: capillary forces will rise buffer levels inside the micro-pipette over a timespan of minutes.

- Four layers parafilm on
- Microscope glass covered with
- Coverglass, heated (100 °C) & pressed tight with spatula.
- Fill with BSA solution to prevent cells from sticking to glass,
- Rinse with buffer.

Suspend cells in (PBS) buffer – the correct tonicity is important to prevent cells from being osmotically stressed.

A.4 Pressure System

For the pressure system (figure A.5), we need

- Reservoir syringe (open)

Figure A.4: Materials needed for the sample preparation and cell suspension, finished U-shaped chambers (bottom centre).

- Height adjustment of reservoir with scales; precision achieved by µm scale.
- Tubes, adaptors for small diameter
- Three way valve
- Filling/rinsing syringe
- Fill with identical buffer as chamber
- Important: Bubble free!

A.5 Aspiration Setup in Exeter

The complete experimental system used to aspirate cells and record the deformation of the cells is shown in figure A.6. Its main components are:

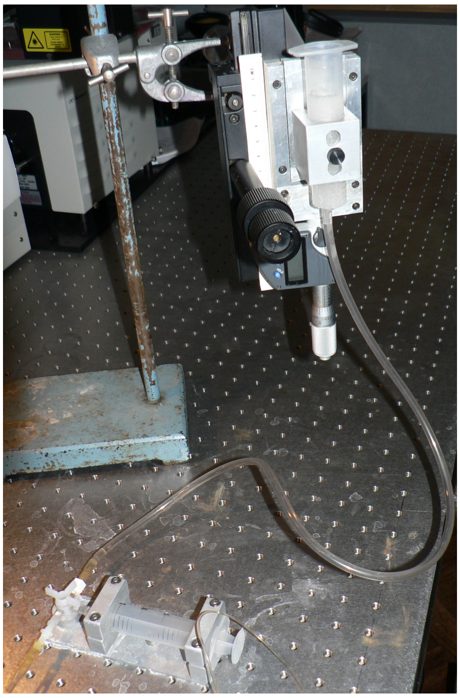

Figure A.5: MA pressure system at Biomedical Physics, University of Exeter. Height adjustment of reservoir with scales (to µm precision)

- Screen & video recorder
- Inverted microscope
- Micro-manipulators
- Pressure system.

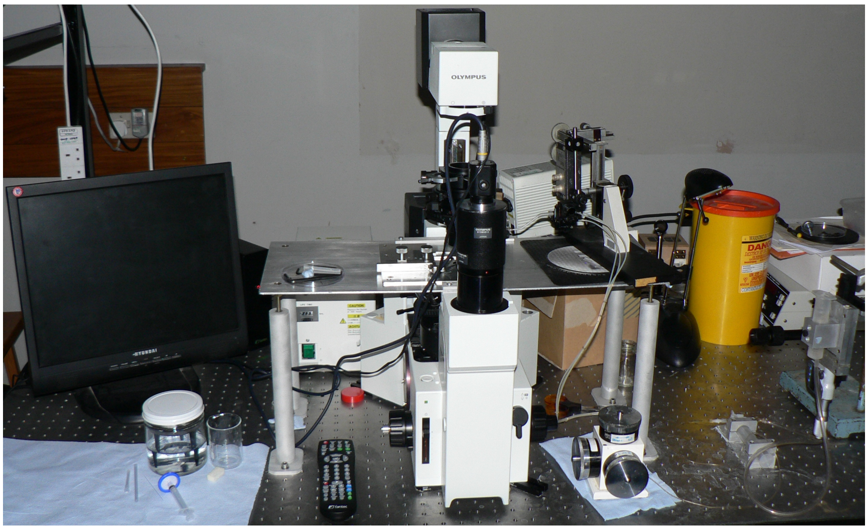

Figure A.6: MA setup at Biomedical Physics, University of Exeter: inverted microscope with camera system and screen, hydraulic micro-manipulators, and pressure system.

Appendix B

Results for AFM measurements on Saccharomyces Cerevisiae

B.1 Protocol for measuring stiffness of Saccharomyces Cerevisiae with AFM

B.1.1 Materials

- Yeast cells in buffer (PBS) suspension
- Pipettes (10–100 µl, 100–1000 µl)
- Syringe & tubing
- Culture tubes
- Filter holder
- Filters, 5 µm diameter holes
- Double-sided, transparent sticky tape
- Microscope slide
- Deionized water

- PBS buffer
- AFM device

B.1.2 Sample preparation

The usage of the AFM device is not explained here, as an extensive user guide exists in both printed and digital versions: (*NanoWizard 3 User Manual SPM Software Release 4.2* 2012).

Remark 2 (Biological deactivation)**.** *Everything that is possibly contaminated with yeast cells is washed three times in a concentrated Halamid (chloramine-T, N-chloro 4-methylbenzenesulfonamide) solution before disposal, especially pipette tips. Surfaces (filters, test-tubes) which need to be de-contaminated have to be left in contact with Halamid for at least* 15 minutes.

1. From dense suspension of *Saccharomyces Cerevisiae* produce 10 ml dilution (20 x), after 30 s mixing on vortex mixer to separate possibly flocculating cells.
2. Prepare filter in filter holder – "shiny" side "up" to receive the cells; the matte side has too high surface roughness.
3. With large-diameter syringe (⇒ low pressure), rinse filter holder and filter with 10 ml of water.
4. Prepare microscope slide with double-sided sticky tape to hold filter.
5. Fill syringe with 10 ml (diluted) cell suspension.
6. Push suspension through filter (harder seems better - one try each...).
7. Remove filter from holder; remove excess liquid by placing filter on paper tissue.
8. Glue filter with sticky tape on microscope slide.
9. Carefully rinse with $\approx$ 100 µl buffer – at least three times.
10. Mount on AFM device; add buffer droplet $\approx$ 50 µl from the side of the glass block, on which the cantilever is mounted.
11. Before (and possibly after) measurements, calibrate sensitivity and spring constant of the cantilever and laser settings, as explained in the manual (Hutter and Bechhoefer 1993; *NanoWizard 3 User Manual SPM Software Release 4.2* 2012).

This protocol allows for comparatively quick sample preparation, but the measurements in the liquid drop suffer from thermal drift and from water evaporation. The protocol could possibly be improved by using the temperature controlled (bio-)chamber with the sealing ring to effectively block evaporation for the duration of the experiments.

B.1.3 Extracting Young's modulus from raw data

Before the Hertz-model can be fitted by the software to a force-distance curve, several pre-processing steps have to be applied to the raw data, since the raw data consist of voltage-distance curves.

1. Apply sensitivity and spring constant settings (saved in the same file) to convert to force-distance curves.
2. Subtract force-baseline using the uppermost 7 % of the data.
3. Set point of contact (zero distance) as point in data closest to maximum force with (force) value zero.
4. Correct the apparent displacement for bending of the cantilever, obtaining the true tip-sample separation.

Finally, the Hertz-fit can be applied to the data after prescribing the correct tip-shape (spherical) and radius (1 µm) and a presumed Poisson's ratio of 0.4. These settings are then applied by the software to all force curves, thereby extracting the Young's modulus at every pixel of the image.

The analysis was based on the tools available in the "JPK Data Processing"[1] software, since data extraction requires a significant computational effort which is adequately solved by the provided software. For this reason, only rectangular patches could be selected, and the Young's modulus $\bar{E}$ was averaged over the pixels within the selection (shown in white in the figures in tables B.1 and B.2) while at the same time estimating the standard "roughness" $R_\mathrm{a} = \frac{1}{N}\sum_{i=1}^{N}|E_i - \bar{E}|$ as a measure for the statistical error of the measurement.

B.2 Results of stiffness measurements of S. Cerevisiae

The following results (see tables B.1, B.2) have been measured using SD-Sphere-FM cantilevers from NANO*SENSORS*™ with a tip radius of $R_\mathrm{Tip} = 1\,\mu\mathrm{m}$.

---

[1] JPK Data Processing version 4.2.59

The AFM device was used in its “Quantitative Imaging” mode, recording a force-distance curve at every pixel. From this information, height maps and Young’s moduli (for assumed Poisson’s ratio of 0.4) could be extracted using the Hertz model as implemented in the analysis software “JPK Data Processing”. To take the curvature of the cells into account, the results were multiplied by a factor $\hat{R}/R_{\mathrm{Tip}} = \sqrt{5/7}$, assuming an average radius of $R_{\mathrm{Cell}} = 2.5\,\mu\mathrm{m}$ of the cells.

Repeated measurements of the same cell in the time-frame of several minutes yield results well within the reported statistical error (N=2).

Table B.1: Young’s modulus results WT strain. Mean: 221 kPa, Median: 167 kPa. The column containing comments points out non-obvious choices of the fitting region. The graphics include the fitting region (and quite unfortunately only part of the description of the size of the fitting region). The colour scale varies from picture to picture.

Date - Time	$\bar{E}/\mathrm{kPa}$	R_a/kPa	Comment	Image
2012.11.28-12.24.05	621.1	25.3		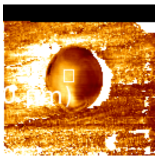
2012.11.28-12.43.00	176.6	5.2	moved	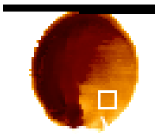
2012.12.05-11.45.09	261.2	27.3	partial	
2012.12.11-14.08.55	170.7	20.0	moved	
2012.12.11-15.05.35	128.5	25.0	moved	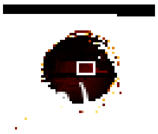

Table B.1: Continued: Young's modulus results WT strain.

Date - Time	$\bar{E}$/kPa	R_a/kPa	Comment	Image
2012.12.12-10.56.17	166.5	27.5		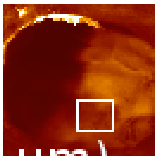
2012.12.12-11.16.23	540.9	45.6		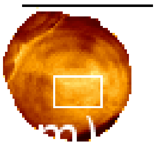
2012.12.12-11.21.45	72.6	2.5		
2012.12.12-11.41.47	147.6	10.0	moved	
2012.12.12-11.46.53	91.9	2.0	moved	
2012.12.12-11.52.46	54.7	4.6	moved	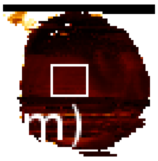

Table B.2: Young's modulus results JC1 strain. Mean: 265 kPa, Median: 116 kPa.The column containing comments points out non-obvious choices of the fitting region. The graphics include the fitting region (and quite unfortunately only part of the description of the size of the fitting region). The colour scale varies from picture to picture.

Date - Time	$\bar{E}$/kPa	R_a/kPa	Comment	Image
2012.12.18- 11.46.55	65.7	4.7	on top	
2012.12.18- 13.07.17	1080.1	189.2	128x128, very flat	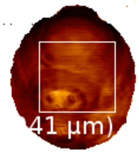
2012.12.18- 13.25.39	109.5	5.0	with bud	
2012.12.18- 13.29.21	101.3	7.1	lost during measurement	
2012.12.18- 13.48.40	183.4	15.9	partial, moved, but ok	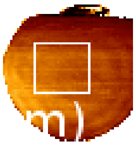
2012.12.18- 13.52.06	252.7	22.8	does not completely fill hole	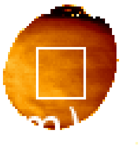

Table B.2: Continued: Young’s modulus results JC1 strain.

Date - Time	$\bar{E}$/kPa	R_a/kPa	Comment	Image
2012.12.18-16.34.39	53.8	4.7	bad fits	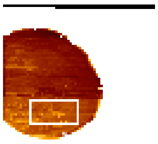
2012.12.18-17.03.56	126.8	15.4	moved	
2012.12.19-10.50.11	65.4	2.8	deep in hole	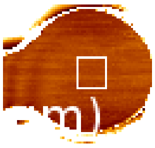
2013.01.08-11.26.56	328.8	67.6	bud scars visible	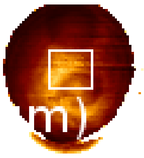
2013.01.09-10.08.22	25.7	2.3	bud in hole (cell on top)	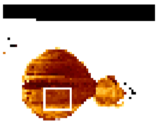
2013.01.09-11.19.51	92.3	4.9	2 cells, deep in combined hole, high-res	
2013.01.09-11.41.05	116.0	37.9	moved during measurement, partially bad fit	

Table B.2: Continued: Young's modulus results JC1 strain.

Date - Time	$\bar{E}$/kPa	R_a/kPa	Comment	Image
2013.01.09-12.18.00	612.1	65.8	bud	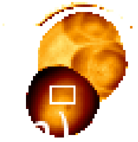
2013.01.09-12.18.00	759.9	109.2	mother (in hole)	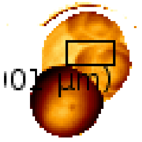

B.2.1 Observational errors in the measurements

There are several sources of observational or measurement error that have to be considered in assessing the data shown above:

1. Due to the uncontrolled evaporation of buffer during the experiments, the tonicity of the buffer might become increasingly hypertonic while the measurements are ongoing in the liquid droplet. From a naive point of view, this would decrease the perceived stiffness, since water would flow out of the cells.

2. Although yeast cells generally survive with a very high probability when dispersed in PBS buffer, the possibility of cell death cannot be excluded.

3. Using Hertz' model to extract the Young's modulus may not be entirely appropriate: adhesion forces between the spherical tip and the cells may modify the measured forces in a non-trivial way. Additionally, the assumption that the cell is a homogeneous, linearly elastic solid is quite questionable in itself. The modification of the Young's modulus due to adhesion can be assumed to be very small (see also discussion in chapter 3.1.2). For a complex geometrical and mechanical structure like a living cell, homogenizing the complexity and assuming linearity (at least for a certain range of forces) is the only way to extract a simple parameter describing contact stiffness. Since that parameter is very useful for for individual cell-based models, and the Hertz model is widely applied in the literature, it seems to be the best approach, also for reasons of comparison. For this reason, the error incurred by using an "inappropriate" model is ignored for the estimation of the total observational error for this measurement.

4. Operator bias in selecting the regions on the cells in which the average Young's modulus is calculated. To assess this observational error, three datasets were analysed by two additional researchers, so that the results can be compared to estimate the severity of the operator bias. There were three rules applied in deciding on the region over which the Young's modulus should be averaged:

   (a) Take as many data points as possible into account, to achieve a reliable estimation (and improved precision).

   (b) Preferentially take a region of low Root Mean Square Deviation (RMSD) between the fitted data and the Hertz-fit (a helpful measure provided by the analysis software).

   (c) Define the region away from the edge of the hole in which the cell is trapped to avoid artefacts caused by interaction with that edge and the higher slope of the cell.

   Since these rules are open to interpretation, separate operators can obviously still define distinct regions, thereby potentially causing an additional source of observational error. The comparison is shown in table B.3, showing that the operator bias is small compared to the statistical error of the measurement.

Table B.3: Comparison of results for the average Young's moduli of three cells obtained by three different operators, using the same measured data. Assuming $R_a \approx$ *RMSD* and an equal number of ≈ 100 samples, none of the discrepancies is statistically significant according to a two-sided Student's t-test ($\alpha = 0.05$).

	Operator 1		Operator 2		Operator 3	
Date - Time	$\bar{E}$/kPa	R_a/kPa	$\bar{E}$/kPa	R_a/kPa	$\bar{E}$/kPa	R_a/kPa
2012.12.18-13.25.39	109.5	5.0	106.4	5.6	104.2	7.7
2012.12.18-13.52.06	252.7	22.8	260.1	10.9	270.3	19.6
2012.12.18-16.30.59	53.8	4.7	47.2	4.1	50.1	4.3

5. The curvature of the cell itself was neglected for the fit, and the final results were corrected with the appropriate factor, assuming a cell radius of 2.5 µm. Since the true curvature at the contact point could not be taken into account by the analysis software, we have to assume a comparatively large bias of 0.3 µm (estimated from the range of diameters of several samples). Additionally, the true radius of the cantilever-tip was not measured either; the assumed radius of 1.0 µm is given by the manufacturer without an estimate of its accuracy, but from the given digit,

it can be assumed that the accuracy will be $\approx 0.1\,\mu\text{m}$. This leads to a total bias of the reduced radius of contact ($\hat{R}$) (filling in the values to obtain the last line) of

$$\begin{aligned}\Delta\hat{R} &= \frac{\partial}{\partial R_1}\Delta R_1\hat{R} + \frac{\partial}{\partial R_2}\Delta R_2\hat{R} \\ &= \frac{\Delta R_1}{R_1^2\left(\frac{1}{R_1}+\frac{1}{R_2}\right)^2} + \frac{\Delta R_2}{R_2^2\left(\frac{1}{R_1}+\frac{1}{R_2}\right)^2} \\ &\approx 0.26\,\mu\text{m}.\end{aligned} \tag{B.1}$$

6. To calculate a force applied by the tip, the most simple linear relationship can be used, since for a correct choice of cantilever only small deformations occur, therefore: $F = k(x - x^*)$. This requires to calibrate the deflection ($d_x = x - x^*$) of the cantilever (sensitivity) and the spring constant k. The sensitivity is fitted from the linear part of a voltage-distance curve taken on a hard, non deforming substrate with the equally non-deforming tip. The second important step is determining the spring constant from the magnitude of the thermal oscillations of the cantilever by estimating the area under the resonance peak in the power spectrum (by fitting a Lorentz-function to the peak). This measurement is very precise and accurate for a known temperature of the system (but it is not even strongly dependent on the temperature in a typical room-temperature range)(Hutter and Bechhoefer 1993). Contrary to that, the error of the sensitivity measurement of the AFM device is difficult to estimate a priori, because it depends on many factors, the most important of which are:

   - The point on the substrate where the voltage-distance curve is recorded which is used for the calibration,
   - the laser position on the cantilever – which may drift during the course of an experiment,
   - the laser output strength as well as the reflectivity of the cantilever and the transparency as well as scattering of the buffer all have an influence,
   - the fitting of the voltage-distance curve (although the error incurred here was very small in tests conducted during calibration),
   - the overall data acquisition (AD-converters, etc.)

   Comparing trial calibrations before and after measurements, the apparent cantilever spring constant for the same cantilever (relying on the sensitivity) was found to vary in a range of 2.6–3.3 N /m (the nominal value according to the manufacturer being 3.1 N /m). Although this observational error is likely dominated by the error on the sensitivity and therefore by Δd_x, for the error on the force measurement, we can subsume it under the error in the spring constant calibration due to the linearity of the problem:

$$\begin{aligned}\Delta F &= \frac{\partial}{\partial k} F\,\Delta k + \frac{\partial}{\partial d_x} F\,\Delta d_x \\ &= d_x\,\Delta k + k\,\Delta d_x \\ &\approx d_x\,\Delta k \\ &\approx 1.17\,\mathrm{nN}\end{aligned} \tag{B.2}$$

Here we assume half the maximum cantilever deformation for a set maximal force of 20 nN of $d_x \approx 3.3\,\mathrm{nm}$ and, from the range quoted above, an observational error for the spring constant of $\Delta k \approx 0.35\,\mathrm{N/m}$.

7. The Poisson's ratio ν – assumed to be 0.4 – can be expected to be over or underestimated by $\Delta\nu \approx 0.1$.

To roughly estimate the total systematic error in the measurements described, we recall the basic Hertz' formula for extracting the Young's modulus:

$$E = \frac{3(1-\nu^2)F_{\mathrm{Hertz}}}{4\sqrt{\hat{R}}\delta^{3/2}} \tag{B.3}$$

We again calculate the error at half the set-point force[2] (maximum force applied by the AFM device) of $F \approx 10\,\mathrm{nN}$, the average measured Young's modulus $E \approx 250\,\mathrm{kPa}$, and therefore an indentation of $\delta \approx 100\,\mathrm{nm}$. This indentation is assumed to carry a negligible systematic error due to the typical high accuracy of the displacement as measured by an AFM device. Under these assumptions, we can estimate the order of magnitude of the systematic error of the measured Young's moduli as follows:

$$\begin{aligned}\Delta E &= \frac{\partial}{\partial \nu} E\Delta\nu + \frac{\partial}{\partial \hat{R}} E\Delta\hat{R} + \frac{\partial}{\partial F} E\Delta F \\ &= \frac{6\nu F_{\mathrm{Hertz}}}{4\sqrt{\hat{R}}\delta^{3/2}}\Delta\nu + \frac{3(1-\nu^2)F_{\mathrm{Hertz}}}{8\sqrt{\hat{R}}^3\,\delta^{3/2}}\Delta\hat{R} + \frac{3(1-\nu^2)}{4\sqrt{\hat{R}}\delta^{3/2}}\Delta F_{\mathrm{Hertz}} \\ &\approx 84\,\mathrm{kPa} \\ \frac{\Delta E}{E} &\approx 0.34\end{aligned} \tag{B.4}$$

---

[2] Since the error on the force is linearly multiplicative, i.e. zero at no indentation and maximal at the greatest applied force, the (mean) error is estimated at the mean applied force.

It is interesting to investigate the relative importance of the estimated error terms: The typical estimated error in the "measurement" of $\hat{R}$ is by far the most important contribution to this comparatively large systematic error, accounting for 54 % of it. Therefore, the results could be considerably improved by extracting the local curvature at the contact point before fitting the Hertz-model to extract the Young's modulus. This should be directly implemented in the "JPK Data Processing" software to avoid unreasonable computation times to extract the parameter. Additionally, one could establish a protocol for ascertaining the tip's radius of curvature e.g. by measuring the artefact at a known sharp step (Allen, Hud, Balooch, et al. 1992).

The second largest contribution to that error (28 %) stems from the uncertainty of the Poisson's ratio ν of the cells. Since it cannot currently be independently measured with comparable accuracy, one could simply report $\hat{E} = \left(\frac{1-\nu_{\mathrm{cell}}^2}{E_{\mathrm{cell}}} + \frac{1-\nu_{\mathrm{tip}}^2}{E_{\mathrm{tip}}} \right)^{-1}$, which is a very useful parameter for individual-cell based models on its own.

Finally, to reduce the bias due to the sensitivity and spring-constant calibration, one should conduct the experiments in a temperature controlled, evaporation-sealed chamber and allow for a sufficient equilibration time of the instrument before starting the experiments – the manufacturer's recommendation received during a second training (on 28th February 2013) on the instrument is 1 h.

Statistical or random errors in the measurements reported in tables B.1 and B.2 are estimated by the value of the "roughness", R_{a}, the total systematic error or bias is estimated above. Clearly, most of the variation of the cell's Young's moduli stems from biological variation, while we cannot exclude the possibility of bias due to increased tonicity of the buffer during experimentation.

B.3 Cell-probe protocols

To prepare a cell probe as employed by e.g. (Bowen, Hilal, Lovitt, et al. 1999; Bowen, Lovitt, and Wright 2001; Hinterdorfer and Dufrene 2006; Zhang, Chen, De Leon, et al. 2004), several trials were undertaken to establish a protocol to reproducibly prepare a cell probe.

Two conceptually different methods were tested to immobilize a cell at the apex of a tip-less cantilever:

- Using a standard glue to keep the cell in place (as described by (Bowen, Lovitt, and Wright 2001))
- Modifying the cantilever surface with "adhesins", allowing the cells to adhere as described by e.g. (Zhang, Chen, De Leon, et al. 2004).

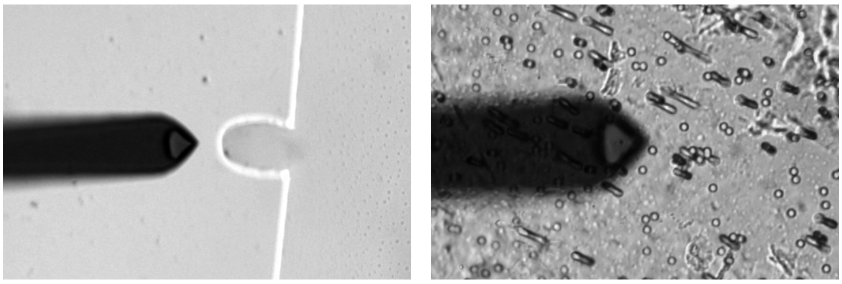

(a) Applying glue (b) Glue with attached cell?

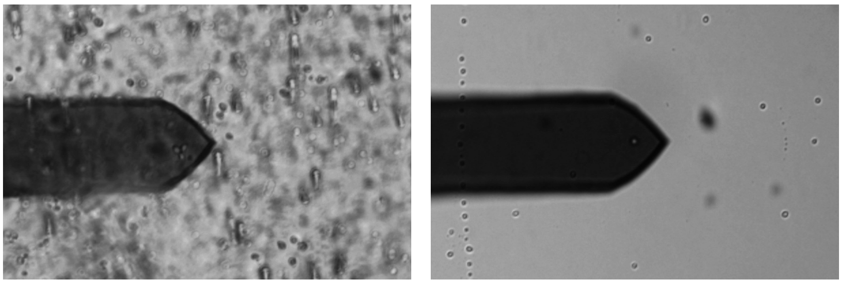

(c) Cells attached to fibronectin (d) Cell attached to polylysene

Figure B.1: Examples of cell attachment during cell-cell adhesion trials (20 x objective, width of cantilever: 50 µm). Figure (a) shows the application of glue (right in frame) to the cantilever, (b) shows a cell attached to the glue on the cantilever. (c) demonstrates the difficulty of picking up only a single cell (here with fibronectin), and finally (d) shows a single cell attached to a cantilever which had been modified with polylysene – the cell may be too far from the apex of the cantilever for a successful experiment of cell-cell adhesion.

Table B.4 gives an overview over the different protocols used.

For all methods, first the glue/adhesin was applied to the cantilever, after which a single cell with ample surrounding space on the glass slide was approached with a fixed set-force, which was held for various times from 30 s to 3 min. After that, the cell was gently picked up by the AFM device. Figure B.1 shows several examples of views on the cantilever of the AFM device with cells attached.

Table B.4: Overview of the different protocols for cell-cell adhesion measurements.

	Gluing trials			Adhesion trials	
	Loctite	Scotch	2-component	Fibronectin	Polylysene
Methods	1. cells in liquid and 2. briefly dried-up cells	1. cells in liquid and 2. briefly dried-up cells	1. cells in liquid and 2. briefly dried-up cells	Cells in liquid, keeping cantilever immersed at at all times	Cells in liquid, keeping cantilever immersed at at all times
Results	No pick-up possible, or cell lost while moving in air	No pick-up possible, or cell lost while moving in air	Cell lost when moving into liquid	Pick-up worked several times, cells loosely attached and lost during movement/during adhesion test	Pick-up worked several times, cells often lost when moving the cantilever; some positive results

Appendix C

Brownian motion force for IBM

To derive the magnitude of the force that can represent Brownian motion for a particle or cell in a low Reynold's number environment for an IBM, we start from the *Diffusion Law* in 3D:

$$\left\langle \|\mathbf{x}\|^2 \right\rangle (\Delta t) = 6 D \Delta t, \tag{C.1}$$

where D is the diffusion constant in three dimensions, $\left\langle \|\mathbf{x}\|^2 \right\rangle$ the mean-squared displacement, and Δt the time-step considered.

It is possible to replace the displacement over the time-step by an expression using the instantaneous average velocity $\mathbf{x}(\Delta t) = \mathbf{v}\Delta t$. In addition, inertia may be neglected because of the assumption that Reynold's number is low: $\mathbf{v} = \mathbf{F}\zeta^{-1}$. Extracting the constants Δt, ζ from the average (ζ being the drag constant), it follows that

$$\left\langle \|\mathbf{F}\|^2 \right\rangle = 6 D \zeta^2 \frac{1}{\Delta t}. \tag{C.2}$$

Substituting the famous *Einstein Relation* $D = \frac{k_\mathrm{B} T}{\zeta}$ (where T is the absolute temperature and k_B is Boltzmann's constant) leaves us with

$$\left\langle \|\mathbf{F}\|^2 \right\rangle = 6 k_B T \zeta \frac{1}{\Delta t} \tag{C.3}$$

Assuming our particle or cell is roughly spherical (a generally good approximation for most cell types in solution), we substitute *Stokes' formula* $\zeta = 6\pi\eta r$, (r being the radius of the particle/cell, η the fluid viscosity) which finally yields

$$\left\langle \|\mathbf{F}\|^2 \right\rangle = \frac{36\pi k_\mathrm{B} T \eta r}{\Delta t}. \tag{C.4}$$

Therefore, at each time-step in an IBM with a Brownian motion force for a particle/cell, we pick a random force unit vector $\hat{\mathbf{F}}_\mathrm{rand}$[1], and scale it in the following way:

$$\mathbf{F}_\mathrm{Brownian} = k \sqrt{\frac{r}{\Delta t}} \hat{\mathbf{F}}_\mathrm{rand} \text{ with } k = 6\sqrt{k_B T \pi \eta}. \tag{C.5}$$

Remark 3 (Modification due to cell-cell interaction)**.** *The derivation described above (and, indeed, the implemented models) do not take into account modifications of said force due to interactions between cells. On the one hand, it is obvious that no fluctuations of momentum due to thermal agitation take place at the area of contact between two interacting cells. On the other hand, the error incurred by neglecting this effect for calculating the Brownian motion force will on average cancel out for cells which are trapped by other cells. There is likely an effect of this error for the probability of breaking a single adhesive contact between two cells, but since the situation is complicated by the hydrodynamics (which are neglected on that scale by the described methods) of the moving cells, it is not trivial to estimate the importance of neglecting modifications of the Brownian motion force due to the cell-cell interaction.*

Remark 4 (Time discretization error in Langevin dynamics)**.** *There is a very interesting recent work on the impact of time discretization errors in Langevin dynamics equations of motion (Sivak, Chodera, and Crooks 2013), but luckily the case for an IBM solving an explicitly low Reynold's number equation of motion does not suffer from many of these concerns since energy is not conserved in the system in the first place.*

---

[1] Care must be taken to obtain a truly random direction – just normalizing three random numbers will introduce artefacts, see e.g. (Cook 1957).

Appendix D

Proof that the friction matrix is positive definite

We start by constructing the friction matrix Γ for N cells:

Γ is symmetrical by design, because the friction coefficient between two cells i and j is symmetric (see equation 3.1):

$$\Gamma = \sum_{i,j \in \mathcal{N}} \underbrace{\begin{pmatrix} 0 & \cdots & & & \\ \cdots & m_{ij} & \cdots & -m_{ij} & \cdots \\ \vdots & & \ddots & & \cdots \\ \cdots & -m_{ij} & \cdots & m_{ij} & \cdots \end{pmatrix}}_{M_{ij}} + \underbrace{\begin{pmatrix} d_{11} & 0 & & \cdots \\ 0 & d_{22} & 0 & \cdots \\ \vdots & & \ddots & \\ 0 & \cdots & & d_{NN} \end{pmatrix}}_{D}$$

where the sum runs over all pairs of interacting cells $\mathcal{N}$ and the elements $d_{ii} = \Gamma_{iw}$ and m are 3×3 matrices for a 3D system.

- The elements of D are diagonal matrices Γ_{iw} and contain values $\in \mathbb{R}^{+}$. For the spherical yeast cells, this term is directly derived from Stokes' law.
- The matrices m describe the interaction of two cells, and are defined in the following way: m is constructed as $m_{ij} = \underbrace{\gamma_n \mathbf{n}_{ij} \mathbf{n}_{ij}^{\mathrm{T}}}_{a} + \underbrace{\gamma_t \left(I - \mathbf{n}_{ij} \mathbf{n}_{ij}^{\mathrm{T}} \right)}_{b}$ where $\mathbf{n}_{ij}$ is the normalized direction vector between the cells i and j and $\gamma_n, \gamma_t \in \mathbb{R}^{+}$ are, respectively, the normal and tangential friction constants.

- For m to be positive-definite, we need to show that $\mathbf{x}^{\mathrm{T}} m \mathbf{x} > 0 \ \forall \mathbf{x} \in \mathbb{R}^3_{\backslash \mathbf{0}}$.
- Look at both parts of the sum:

  a: $\gamma_n \mathbf{x}^{\mathrm{T}} \mathbf{n}_{ij} \mathbf{n}_{ij}^{\mathrm{T}} \mathbf{x} = \gamma_n (\mathbf{x} \cdot \mathbf{n}_{ij})^2 > 0$, so a is positive definite.

  b: $\gamma_t (\mathbf{x}^{\mathrm{T}} \mathbf{x} - \mathbf{x}^{\mathrm{T}} \mathbf{n}_{ij} \mathbf{n}_{ij}^{\mathrm{T}} \mathbf{x}) \geq 0$:

  - True, if and only if $(\mathbf{x} \cdot \mathbf{x}) \geq (\mathbf{x} \cdot \mathbf{n}_{ij})^2$
  - Using the Cauchy-Schwarz inequality: $(\mathbf{x} \cdot \mathbf{n}_{ij})^2 \leq (\mathbf{x} \cdot \mathbf{x}) \cdot (\mathbf{n}_{ij} \cdot \mathbf{n}_{ij}) = (\mathbf{x} \cdot \mathbf{x}) \cdot 1$.

  ⇒ b is positive semi-definite.

⇒ m is positive definite, since the sum of a positive definite matrix and a positive semi-definite matrix is positive definite.

- It remains to be proven that M_{ij} is positive semi-definite:

  Let us consider the two-cell case: $M_{ij} = \begin{pmatrix} m & -m \\ -m & m \end{pmatrix}$, since the generalization is obvious. We show that $\mathbf{x}^{\mathrm{T}} M_{ij} \mathbf{x} \geq 0$:

  Let $\mathbf{x}^{\mathrm{T}} = (\mathbf{a}, \mathbf{b})$ with $\mathbf{a}, \mathbf{b}$ chosen to be the basis of $\mathbb{R}^3$ for which m is diagonal with $m_{ii} \in \mathbb{R}^+$ - which is possible, since m is symmetrical and positive definite, as just proven, then:

$$\begin{aligned} \mathbf{x}^{\mathrm{T}} M_{ij} \mathbf{x} &= \sum_{i=1}^{3} (a_i m_{ii} a_i + b_i m_{ii} b_i - a_i m_{ii} b_i - b_i m_{ii} a_i) \\ &= \sum_{i=1}^{3} m_{ii} (a_i - b_i)^2 \geq 0 \end{aligned}$$

⇒ M_{ij} is positive semi-definite, and since the sum of a positive semi-definite matrix and the positive-definite diagonal matrix D is positive definite,

⇒ Γ is positive definite. q.e.d.

Thanks to this result, in our algorithm, we solve the equation of motion 3.1 at each time-step as a coupled system for the velocities of the cells $\mathbf{v}$ with the Conjugate Gradient Method using the diagonal- or Jacobi-preconditioner, since the Matrix is diagonally dominated.

I am grateful for discussions about this proof (which has been published in a modified way in (Van Liedekerke, Smeets, Odenthal, et al. 2013)) with Bart Smeets, Christian Hammann, Florian Johann and Tobias Seifen.

Appendix E

Rounded triangles: resolution of contact & calculation of contact point

Here we derive the contact point between two contacting triangles, which have encompassing spheres. We assume that the actual contact point must be within the contact plane of the spheres. Any other position of the contact point would “favor” one sphere over the other for no apparent reason. Therefore, we first orthogonally project the corner points of both triangles $P = \{p_1, p_2, p_3\}$ and $Q = \{q_1, q_2, q_3\}$ to the contact plane of the spheres, as illustrated in figure E.1.

The overlap area and the two projected triangles $P' = \{p_{1'}, p_{2'}, p_{3'}\}$ and $Q' = \{q_{1'}, q_{2'}, q_{3'}\}$ are all located in the same plane, which is shown in figure E.2. An actual contact between the triangles exists when there exists an intersecting area of both contact circle, P' and Q' (indicated by the dark red area in figure E.2). As the overlap between the encompassing spheres decreases monotonously when going away from c, the contact point where the overlap between the encompassing spheres is maximal must be the point in the dark red area that is closest to c. This point is also the point in the light red area that is closest to c, as the extra part in the light red area is outside the circle and therefore always further away from c.

The light red area is the polygon $S = \{q_{1'}, s_1, p_{3'}, s_2\}$. The number of corner points of this polygon can vary dependent on the relative positions of the two triangles, and can take values between 3 and 6. In order to fully determine this polygon we need to calculate the intersection points (in this case s_1 and s_2). The intersection s between two

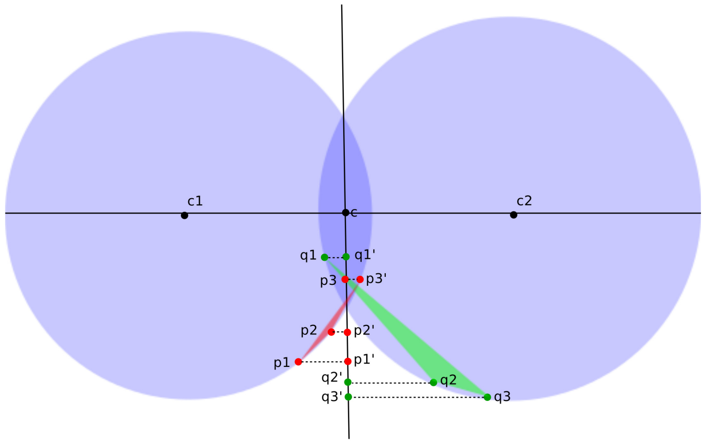

Figure E.1: Triangles P and Q, which belong to two (deformable) bodies in contact, are projected onto the contact plane of their encompassing spheres. This is needed to check, if a contact force and a contact moment is generated from this particular pair of facets, and if so to calculate the magnitudes.

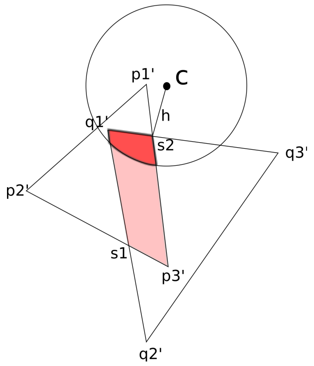

Figure E.2: Intersection of triangles $P' = \{p_{1'}, p_{2'}, p_{3'}\}$, $Q' = \{q_{1'}, q_{2'}, q_{3'}\}$ and the contact area of the two encompassing spheres of the triangles with center c.

lines defined by four points x_1, x_2, x_3 and x_4 can be found as:

$$s = x_1 + a\frac{(c \times b) \cdot (a \times b)}{\|a \times b\|^2} \tag{E.1}$$

with $a = x_2 - x_1$, $b = x_4 - x_3$ and $c = x_3 - x_1$. Of course we will always find an intersection between two lines within a plane. We also need to check whether s is effectively on the triangle segment. For a triangle segment between p_1 and p_2, this is true if:

$$\|p_1 - s\|^2 < \|p_1 - p_2\|^2 \tag{E.2}$$

and

$$\|p_2 - s\|^2 < \|p_1 - p_2\|^2 . \tag{E.3}$$

This check requires no (expensive) calculations of square roots. In order to find all intersection points between two triangles P' and Q' we have to calculate equation E.1 nine times (three times for each side of P') and perform 18 checks of the squared norms.

The polygon S is the collection of all intersection points and all corner points of the triangles P' that are within triangle Q' and corner points of triangle Q' that are within triangle P'. This requires six checks again. Next, we sort each point p_i from $\{p_2 \dots p_n\}$ according to the dot product with p_1, yielding a set of counter-clockwise sorted elements. We then calculate the closest distance from this sorted polygon S to c, giving the closest point c_p as the contact point and the squared distance h^2. h^2 can be used to calculate the overlap δ_t. If c is within S, the distance between S and c is zero and the contact point will be c itself. From h^2, we can calculate the actual overlap δ_t as:

$$\delta_t = \delta_s - R_1 - R_2 + \sqrt{R_1^2 - h^2} + \sqrt{R_2^2 - h^2} \tag{E.4}$$

with $h = \|c - c_p\|^2$ and δ_s being the overlap for a sphere-sphere contact ($\delta_s = \|c_2 - c_1\| - R_1 - R_2$).

An additional check that we need to perform for this method is whether one of the two triangles actually is on the opposite side of the sphere. We only need to calculate contacts between triangles which are facing each other with their “outside” direction. We define the threshold angle for this to be 90°, i.e. for angles of more than 90° between any triangle and the contact plane, the triangles do not face each other and no contact should be calculated:

$$n_1 \cdot (c_2 - c_1) > 0 \quad \wedge \quad n_2 \cdot (c_1 - c_2) > 0 \tag{E.5}$$

in which n_1 and n_2 are normal vectors on triangle 1 (P) and triangle 2 (Q). If equation E.5 holds, the triangles are facing each other. In the implementation, this check is performed at the start of contact resolution, because we can immediately discard the contact if this simple check does not hold.

Appendix F

Bouncing ball simulation and mesh-independence of the contact force

As a proof-of-principle problem, we let a soft, but rigid (with only six degrees of freedom) ball bounce on a soft flat substrate. The only acting forces are gravity and a velocity dependent drag force as body forces on the ball, and Hertz' contact force between the ball and the substrate. We solve Newton's equations of motion:

$$\mathbf{F}_{\text{ball}} = m \cdot \mathbf{g} - c \cdot \mathbf{v} + \frac{4\hat{E}a^3}{3\hat{R}} \cdot \hat{n} = m \cdot \mathbf{a}, \tag{F.1}$$

using an explicit leap-frog time integration method (Tijskens, Ramon, and De Baerdemaeker 2003). Here $\hat{n}$ is the normal vector to the contact plane. Figure F.1 shows the result of that simulation with the rigid sphere, but also with three differently coarse meshes, using the algorithm explained in chapter 4.

F.1 Meshed bouncing ball

As figure F.1 illustrates, the newly developed contact model achieves the same results for this situation as the well-known Hertz model (red sphere). On top of that, the outcome of the simulations does not depend on the refinement of the chosen mesh: Only minor deviations can be seen after approximately ten "bounces" for the coarsest mesh.

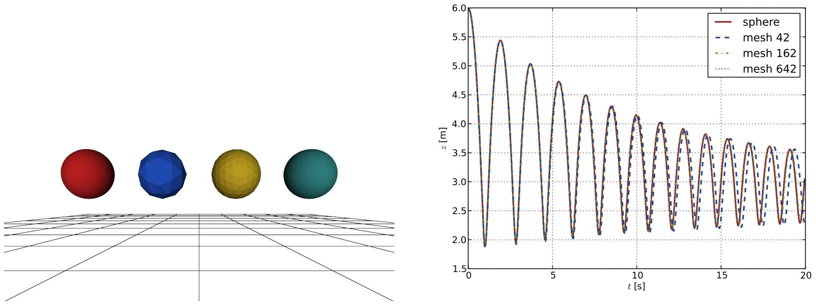

(a)

(b)

Figure F.1: Bouncing ball simulation. (a) gives a view on the starting point of the simulation. (b) shows the time evolution of the z-coordinate of the centre of mass for all four representations of the ball. For the coarsest mesh with 42 nodes, deviations at the end of the simulation are visible.

F.2 Meshed sphere adhesion

We show convergence with mesh refinement by simulating an adhesive triangulated sphere ($R = 3\,\mu\text{m}$, $W = 1\,\text{mJ/m}^2$) that is being loaded onto a flat plane. Five different mesh refinements are considered, all based on regular subdivisions of the icosahedron yielding 48 to 10 242 nodes. Figure F.2(a) shows force versus penetration depth for subdivisions with 48, 642 and 10 242 nodes, calculated by integrating the MD pressure for a Tabor coefficient (μ) of 0.1, compared to the solution of Hertz (no adhesion), JKR, MD andDMT. Figure F.2(b) shows the change in normalized RMSD with mesh refinement for different Tabor coefficients μ. For high values of μ (close to the JKR limit), the error in the calculated forces is larger as the adhesive tension diverges near the edge of the contact radius (compare to equations 4.4 and 4.10).

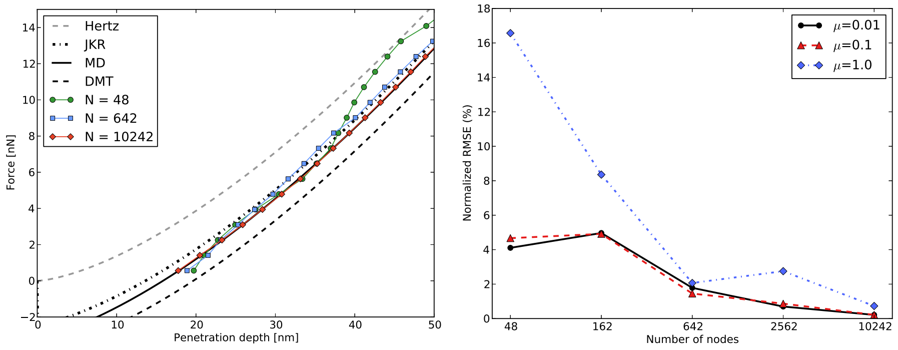

(a) (b)

Figure F.2: Adhesive sphere simulation. (a) Force versus penetration depth for adhesive meshed sphere (MD, $\mu = 0.1$) with different mesh refinements, compared with analytical solutions for Hertz, JKR, MD and DMT. (b) Root Mean Square Deviation (RMSD), normalized as a percentage of the maximal force, for prediction of the analytical MD solution as a function of mesh refinement for different Tabor coefficients μ.

Appendix G

Installation HowTo of DEMeter++ on linux (KUbuntu)

G.1 Prerequisites

G.1.1 System libraries

To reuse shared libraries which may be already loaded as much as possible as well as ease installation and maintenance, we try to use as many low-level libraries the system provides as possible. In addition, this will significantly shorten compile-times.

To install those, you can of course use your favorite package manager, which will give additional information, but for simplicity, we provide the commands you should be able to execute on the command-line with the most basic package management tool in the debian world: apt-get.

Building For this it is most convenient to rely on the *build-essential* package containing g++(C++ compiler), libc6-dev (the standard library), make and dpkg-dev (which are not currently needed). *gcc* (C-compiler) and *gfortran* (Fortran-compiler) should be installed as well.[1]

---

[1] In these commands as well as all commands below, the $ signifies the command-line prompt and is not to be typed!

```
$ sudo apt-get install build-essential
$ sudo apt-get install gcc
$ sudo apt-get install gfortran
```

Loki Apparently, *loki-dev* is “the” C++ library of generic programming techniques, but what Bert uses it for, I have no clue... ;-)

```
$ sudo apt-get install libloki-dev
```

QGLViewer We only need to install *libqglviewer-qt4-dev*, which will pull in all other dependencies, especially on Qt itself. This might be a lot of stuff, especially in Ubuntu without KDE, which itself relies on Qt...

```
$ sudo apt-get install libqglviewer-qt4-dev
```

Subversion We’ll need this to checkout (and later in) the DEMeter++ source code.

```
$ sudo apt-get install subversion
```

cmake Since we finally moved away from bjam to the more beautiful and a lot better documented cmake, you’ll probably want to install its “graphical” front end:

```
$ sudo apt-get install cmake-curses-gui
```

Python We now propose to install the enthought canopy[2], since this seems to be kept nicely compatible with basically all needed (or, in fact, ever wanted) python libraries in one place. You’ll have to register as an academic user to have access to some of the packages we’ve grown quite fond of.

```
$ chmod +x canopy-*.sh
$ ./canopy-*.sh
```

Here, you want to make sure that you install somewhere sensible like `$HOME/src/canopy/` or so. You’ll have to do some additional work now to make use of this installation of python stuff: Firstly, start canopy,

```
 $ canopy
```

and allow it to become your standard python environment. You probably want to log in with your account and install some more python packages. Afterwards, in your `$HOME/.bashrc`, you should add the line

---

[2] `https://www.enthought.com/store/`

```
source $HOME/.profile
```

and back in you shell

```
source $HOME/.bashrc
```

to let the change take effect. After that first start, canopy should have created a directory `$HOME/Enthought/`; for some reason they only put most required information here, however, so we have to make a link to the python headers as used by canopy in here as well:

```
$ cd $HOME/Enthought/Canopy_64bit/User/include
$ ln -s $HOME/src/canopy/appdata/\
     canopy-LONGVERSIONSTRING/include/python2.7
```

G.1.2 Environment variables

To get the linker to behave & to use the pyDEMeter module from python, you need to configure a few additional environment variables, which is typically done in `$HOME/.bashrc`. Example:

```
export PATH=.:$HOME/bin:$PATH:
export PYTHONPATH=.:$HOME/lib/:$PYTHONPATH:
export LD_LIBRARY_PATH=.:$HOME/lib/:$LD_LIBRARY_PATH:
export BOOST_INCLUDEDIR=$HOME/include:
export BOOST_LIBRARYDIR=$HOME/lib:
```

When you've done that, don't forget to either open a new shell to continue working, or do a quick
`source $HOME/.bashrc` in your current one, since otherwise the environment variables are not updated.

G.1.3 Boost

The default location for installing boost has proven to be not ideal. It is easier, to just install it in one's home directory. First, download your preferred version of boost[3].

Secondly, you'll want to do the following (assuming you have a dedicated directory for source code called `$HOME/src`):

---

[3] `http://www.boost.org/users/download/`. If unsure which one to download, the `.tar.bz2`-file is probably smallest & quickest to use.

```
$ cd $HOME/src
$ tar -xvjf /path/to/your/downloaded/boost.tar.bz2
$ cd boost_*
$ ./bootstrap.sh --with-libraries=system,filesystem,python,\
serialization,date_time,wave,test --prefix=/home/yourUsername
```

Now, you need to check the `project-config.jam` file in your boost-directory. Under `#Python configuration`, it should refer to your Enthought canopy installation - otherwise paste something like:

```
using python : 2.7 :
    /home/tim/Enthought/Canopy_64bit/User/bin :
    /home/tim/Enthought/Canopy_64bit/User/include/python2.7 :
    /home/tim/Enthought/Canopy_64bit/User/lib ;
```

If it found the Enthought canopy-stuff automatically (even if it doesn't explicitly give all the directories), even better...

Now, we need to make absolutely sure, that boost-wave is compiled with threading disabled, hence we modify (according to Simon) the `Jamroot` by adding the option

```
<define>BOOST_WAVE_SUPPORT_THREADING=0
```

in the

```
project boost
    : requirements
```

section. Then we're ready to finally do

```
$ ./b2 install -jNumberOfYourProcessors
```

That will create (if not already present) a `$HOME/lib` and `$HOME/include` directory.

G.1.4 CGAL

If you want to use the BIO module of DEMeter++ , you will have to download and compile CGAL[4] as well.

---

[4] `http://www.cgal.org/download.html`
We're currently using version 3.9 or 4.0, which both work fine for parameterizing 3D meshes to a 2D (u,v) map.

After you download and extract into a suitable folder, you have to use a slight[5] hack to make it work together with DEMeter++ +stdlibary+boost: CGAL prefers the stdlib-TR1 stuff over boost, while we do the other way round (for windows compatibility, I suppose), so we have to make CGAL do things our way.

The hack is: go to `$HOME/src/cgal/CGAL-3.9/config/testfiles` (or wherever you extracted CGAL) and in the files `CGAL_CFG_NO_TR1_ARRAY.cpp` and `CGAL_CFG_NO_TR1_TUPLE.cpp`, change the assert so that it fails (e.g. `assert(... == 3);` instead of `assert(... == 2);`). Then we can proceed to compile in `$HOME/src/cgal/CGAL-3.9/` using

```
ccmake .
make -jNumberOfProcessors
sudo make install
```

after ccmake, you will have to press [c]onfigure and [g]enerate, so that it gets actually done. We install into the default location so that we also have the manual installed properly - but you can change this however you like (if configured correctly in DEMeter++ 's ccmake!).

G.2 Installing DEMeter++

Now, we're ready to install DEMeter++ itself:

G.2.1 Getting DEMeter++

Using subversion is very convenient from the command-line, however once you check out one of the directories, you can just as easily use subversion from your file-manager (at least KDE's dolphin...). In the directory, where you want the DEMeter++ sources to be (typically `$HOME/src/dem/`), you can do (assuming the IP stays the same...)

```
$ svn co svn://10.33.84.87/Arraythmetic
$ svn co svn://10.33.84.87/DEMeter10
$ svn co svn://10.33.84.87/ETility
$ svn co svn://10.33.84.87/Tiny
$ svn co svn://10.33.84.87/cmake
$ svn co svn://10.33.84.87/YourUserName
```

---

[5] Ok, rather nasty!

G.2.2 Compiling with cmake

If you develop in DEMeter++ , it is most likely worthwhile to keep at least both a Debug and a Release version of the code. This can be easily done with cmake:

```
$ cd $HOME/src/dem/
$ mkdir build_debug
$ mkdir build_release
$ cd build_release
$ ccmake ../cmake/
```

Now, for the first time we simply hit `c`, and hopefully get a text informing us about some versions of the software. Hitting `e`, we are in a menu, in which we can and should configure our DEMeter++ building:

BOOST_ROOT Has to be set to your downloaded version!

PYTHON_MODULES Has to be ON for DEMeter++ to be usable

CMAKE_BUILD_TYPE If you're in the `build_release` directory, you'll choose Release, else Debug...

CMAKE_INSTALL_PREFIX Should be where you want to install, so typically your `/home/yourUsername`. That will install into `$HOME/bin` and `$HOME/lib`.

DEMETER_BIO If you're going to simulate biological systems, you want to turn this on...

DEMETER_OUTPUT_FORMAT You can choose between mpc (MultiplePersistentCollection) and dst (DataSet), the last of which is newer and better...

DEMETER_POLICY_LAYOUT Here you can have either the Interleaved (usually better) or the Array (cuda-compatible) layout

DEMETER_POLICY_STORAGE Choose between Blocked (better for changing particle numbers) and Contiguous (cuda-compatible) storage policy.

After pressing `t` you'll see tons of additional stuff, of which the following ones might be important:

CMAKE_CXX_FLAGS_RELEASE Maybe you want to turn on specific optimizations for your cpu...?

PYTHON_INCLUDE_DIR If you're using Enthought, this should be set to `/home/yourName/Enthought/Canopy_64bit/User/include/python2.7` – or wherever your valid `pyconfig.h` is...

PYTHON_LIBRARY If you're using Enthought, you should set that to `/home/yourUsername/Enthought/Canopy_64bit/User/include/lib`.

When you're happy with your settings, hit `c` again, and `e` and `g` afterwards, to generate the makefiles. Now, you can call make && make install, but to not see all those ugly warnings & more easily find the error - should such a thing occur - we suggest using:

```
$ make -jNumberOfYourCpus 2>errors.txt && make install
```

Now you have the latest working DEMeter++ [6]!

If you need to debug code, I'd suggest also immediately setting up a `build_debug` directory, into which you copy the `build_release/CMakeCache.txt` file and then change the `CMAKE_BUILD_TYPE` using `ccmake ../cmake/` to `Debug`. Then you can compile here again - and `make install` only when necessary. It probably also pays to execute

```
$ make test
```

from time to time, which will run all unit test, checking if basic functionality is still ok.

---

[6] Unless of course, you changed something and made an error, in which case you can open errors.txt and search for the line with the error-information. There are some unavoidable benign warnings due to the advanced use of templates & the preprocessor - but possibly also avoidable ones!

Bibliography

Adams, D. N. (2010). *The ultimate hitchhiker's guide to the galaxy*. Random House Digital, Inc. (cit. on p. 1).

Allen, M. J., N. V. Hud, M. Balooch, R. J. Tench, W. J. Siekhaus, and R. Balhorn (1992). „Tip-radius-induced artifacts in {AFM} images of protamine-complexed {DNA} fibers". In: *Ultramicroscopy* 42–44, Part 2, pp. 1095–1100. ISSN: 0304-3991. DOI: `10.1016/0304-3991(92)90408-C` (cit. on p. 108).

Alsteens, D., V. Dupres, K. Mc Evoy, L. Wildling, H. Gruber, and Y. Dufrêne (2008). „Structure, cell wall elasticity and polysaccharide properties of living yeast cells, as probed by AFM". In: *Nanotechnology* 19, p. 384005. URL: `http://www.iop.org/EJ/abstract/0957-4484/19/38/384005` (cit. on pp. 20, 21).

Altinisik, F. (2011). „Determination of cell mechanical properties with a micropipette aspiration system". MA thesis. KU Leuven (cit. on pp. 14, 15).

Anderson, A. R., M. A. J. Chaplain, K. A. Rejniak, and W. Alt, eds. (2007). *Single-Cell-Based Models in Biology and Medicine*. Mathematics and Biosciences. Birkhaeuser Verlag AG (cit. on p. 2).

Ashkin, A. (Jan. 1970). „Acceleration and Trapping of Particles by Radiation Pressure". In: *Physical Review Letters* 24 (4), pp. 156–159. DOI: `10.1103/PhysRevLett.24.156` (cit. on p. 17).

Baaijens, F., W. Trickey, T. Laursen, and F. Guilak (2005). „Large Deformation Finite Element Analysis of Micropipette Aspiration to Determine the Mechanical Properties of the Chondrocyte". In: *Annals of Biomedical Engineering* 33, pp. 494–501. URL: `http://www.springerlink.com/content/q47402n3g7t64846/` (cit. on p. 14).

Barber, C. B., D. P. Dobkin, and H. Huhdanpaa (1996). „The quickhull algorithm for convex hulls". In: *ACM Transactions on Mathematical Software (TOMS)* 22.4, pp. 469–483. URL: `http://www.qhull.org` (cit. on p. 33).

Barreto, S., C. H. Clausen, C. M. Perrault, D. A. Fletcher, and D. Lacroix (2013). „A multi-structural single cell model of force-induced interactions of cytoskeletal components". In: *Biomaterials* 34.26, pp. 6119–6126. ISSN: 0142-9612. DOI: `10.1016/j.biomaterials.2013.04.022` (cit. on pp. 5, 68).

Barrett, R. (1994). *Templates for the solution of linear systems: building blocks for iterative methods*. Society for Industrial Mathematics. ISBN: 0898713285 (cit. on p. 75).

Barthel, E. (2008). „Adhesive elastic contacts: JKR and more". In: *Journal of Physics D: Applied Physics* 41.16, p. 163001. URL: `http://stacks.iop.org/0022-3727/41/i=16/a=163001` (cit. on p. 47).

Binning, G. (1986). „Atomic force microscope". In: *Physical Review Letters* 56, pp. 930–933 (cit. on p. 17).

Boal, D. (2012). *Mechanics of the Cell*. 2nd ed. Cambridge University Press (cit. on pp. 2, 59, 63).

Boal, D. H. and M. Rao (Sept. 1992). „Topology changes in fluid membranes". In: *Physical Review A* 46 (6), pp. 3037–3045. DOI: `10.1103/PhysRevA.46.3037` (cit. on p. 53).

Bowen, W. R., N. Hilal, R. W. Lovitt, and C. J. Wright (1999). „An atomic force microscopy study of the adhesion of a silica sphere to a silica surface—effects of surface cleaning". In: *Colloids and Surfaces A: Physicochemical and Engineering Aspects* 157, 117–125 (cit. on p. 108).

Bowen, W. R., R. W. Lovitt, and C. J. Wright (2001). „Atomic Force Microscopy Study of the Adhesion of Saccharomyces cerevisiae". In: *Journal of Colloid and Interface Science* 237, pp. 54–61 (cit. on pp. 22, 108).

Brady, J. and G. Bossis (1988). „Stokesian Dynamics". In: *Anuual Review of Fluid Mechanics* 20, pp. 111–157. ISSN: 0066-4189. DOI: `10.1146/annurev.fluid.20.1.111` (cit. on pp. 7, 64).

Cappella, B. and G. Dietler (1999). „Force-distance curves by atomic force microscopy". In: *Surface Science Reports* 34, pp. 1–104 (cit. on p. 17).

Chazelle, B. (Dec. 1993). „An optimal convex hull algorithm in any fixed dimension". In: *Discrete & Computational Geometry* 10.1, pp. 377–409. DOI: `10.1007/BF02573985` (cit. on p. 33).

Chu, Y. S., S. Dufour, J. P. Thiery, E. Perez, and F. Pincet (2005). „Johnson-Kendall-Roberts Theory Applied to Living Cells". In: *Physical Review Letters* 94.2, p. 028102. DOI: `10.1103/PhysRevLett.94.028102` (cit. on pp. 14, 27, 47).

Chu, Y.-S., W. Thomas, O. Eder, F. Pincet, E. Perez, J. Thiery, and S. Dufour (2004). „Force measurements in E-cadherin-mediated cell doublets reveal rapid adhesion strenghtened by actin cytoskeleton remodeling through Rac and Cdc42". In: *The Journal of Cell Biology* 167, pp. 1183–1194 (cit. on p. 14).

Compucell3D (n.d.). URL: `http://www.compucell3d.org/` (cit. on p. 5).

Cook, J. (1957). „Rational formulae for the production of a spherically symmetric probability distribution". In: *Mathematics of Computation* 11.58, pp. 81–82 (cit. on p. 112).

Cowper, G. R. (1973). „Gaussian quadrature formulas for triangles". In: *International Journal for Numerical Methods in Engineering* 7.3, pp. 405–408. ISSN: 1097-0207. DOI: `10.1002/nme.1620070316` (cit. on p. 50).

Cuvelier, D., M. Thery, Y.-S. Chu, S. Dufour, J.-P. Thiery, M. Bornens, P. Nassoy, and L. Mahadevan (2007). „The universal dynamics of cell spreading". In: *Current Biology* 17, pp. 694–699 (cit. on pp. 42, 44, 56, 59, 60, 64–67).

Dao, M., J. Li, and S. Suresh (Sept. 2006). „Molecularly based analysis of deformation of spectrin network and human erythrocyte". In: *Materials Science and Engineering: C* 26.8, pp. 1232–1244. ISSN: 09284931. DOI: `10.1016/j.msec.2005.08.020` (cit. on pp. 7, 44).

Dawkins, R. (1976). *The selfish gene*. Oxford University Press Inc., New York (cit. on pp. 26, 38).

Deutsch, A. and S. Dormann (2004). *Cellular Automaton Modeling of Biological Pattern Formation: Characterization, Applications, and Analysis (Modeling and Simulation in Science, Engineering and Technology)*. Birkhaeuser Verlag AG. DOI: `10.1007/b138451` (cit. on p. 5).

Discher, D. E., D. H. Boal, and S. K. Boey (1998). „Simulations of the Erythrocyte Cytoskeleton at Large Deformation. II. Micropipette Aspiration". In: *Biophysical Journal* 75, pp. 1584–1597. DOI: `10.1016/S0006-3495(98)74076-7` (cit. on pp. 14, 53).

Drasdo, D., S. Hoehme, and M. Block (2007). „On the Role of Physics in the Growth and Pattern Formation of Multi-Cellular Systems: What can we Learn from Individual-Cell Based Models". In: *Journal of Statistical Physics* 128, pp. 287–345 (cit. on pp. 8, 27, 29, 44, 59).

Drasdo, D., R. Kree, and J. S. McCaskill (Dec. 1995). „Monte Carlo approach to tissue-cell populations". In: *Physical Review E* 52.6, pp. 6635–6657. DOI: `10.1103/PhysRevE.52.6635` (cit. on pp. 7, 29).

Dunn, S.-J., A. G. Fletcher, S. J. Chapman, D. J. Gavaghan, and J. M. Osborne (Apr. 2012). „Modelling the role of the basement membrane beneath a growing epithelial monolayer". In: *Journal of Theoretical Biology* 298, pp. 82–91. DOI: `10.1016/j.jtbi.2011.12.013` (cit. on p. 8).

Enderling, H., A. R. Anderson, M. A. Chaplain, A. Beheshti, L. Hlatky, and P. Hahnfeldt (Nov. 2009). „Paradoxical Dependencies of Tumor Dormancy and Progression on Basic Cell Kinetics". In: *Cancer Research* 69.22, pp. 8814–8821. DOI: `10.1158/0008-5472.CAN-09-2115` (cit. on p. 4).

Español, P., M. Serrano, and I. Zuñiga (Aug. 1997). „Coarse-Graining of a Fluid and its Relation with Dissipative Particle Dynamics and Smoothed Particle Dynamic". In: *International Journal of Modern Physics C* 08.04, pp. 899–908. DOI: `10.1142/S0129183197000771` (cit. on p. 7).

Evans, E. (1980). „Minimum energy analysis of membrane deformation applied to pipet aspiration and surface adhesion of red blood cells". In: *Biophysical Journal* 30.2, pp. 265–284. ISSN: 0006-3495 (cit. on p. 14).

Fedosov, D. A., B. Caswell, and G. E. Karniadakis (2010). „Systematic coarse-graining of spectrin-level red blood cell models". In: *Computer Methods in Applied*

Mechanics and Engineering 199.29–32, pp. 1937–1948. ISSN: 0045-7825. DOI: `10.1016/j.cma.2010.02.001` (cit. on pp. 7, 42, 44, 52, 53, 59, 64).

Fedosov, D. A., H. Lei, B. Caswell, S. Suresh, and G. E. Karniadakis (Dec. 2011). „Multiscale Modeling of Red Blood Cell Mechanics and Blood Flow in Malaria". In: *PLoS Computational Biology* 7.12, e1002270. DOI: `10.1371/journal.pcbi.1002270` (cit. on pp. 7, 42, 53, 56, 64).

Fingar, D. C., S. Salama, C. Tsou, E. Harlow, and J. Blenis (2002). „Mammalian cell size is controlled by mTOR and its downstream targets S6K1 and 4EBP1/eIF4E". In: *Genes & development* 16.12, pp. 1472–1487 (cit. on p. 29).

Fung, Y. and P. Tong (1968). „Theory of the sphering of red blood cells". In: *Biophysical journal* 8.2, pp. 175–198 (cit. on p. 48).

Galle, J., M. Loeffler, and D. Drasdo (2005). „Modeling the effect of deregulated proliferation and apoptosis on the growth dynamics of epithelial cell populations in vitro". In: *Biophysical journal* 88.1, pp. 62–75. ISSN: 0006-3495 (cit. on pp. 8, 31, 55, 59).

Gardel, M. L., F. Nakamura, J. H. Hartwig, J. C. Crocker, T. P. Stossel, and D. A. Weitz (2006). „Prestressed F-actin networks cross-linked by hinged filamins replicate mechanical properties of cells". In: *Proceedings of the National Academy of Sciences of the United States of America* 103.6, pp. 1762–1767. DOI: `10.1073/pnas.0504777103` (cit. on p. 69).

Gardner, M. (1970). „Mathematical games: The fantastic combinations of John Conway's new solitaire game "life"". In: *Scientific American* 223.4, pp. 120–123. URL: `http://www.math.kth.se/~gunnarj/LIFE/lifegame5w.html` (cit. on p. 4).

Geris, L., P. V. Liedekerke, B. Smeets, E. Tijskens, and H. Ramon (2009). „A cell based modelling framework for skeletal tissue engineering applications". In: *Journal of Biomechanics* 10, p. 1016 (cit. on p. 27).

Ghysels, P., G. Samaey, B. Tijskens, P. V. Liedekerke, H. Ramon, and D. Roose (2009). „Multi-scale simulation of plant tissue deformation using a model for individual cell mechanics". In: *Physical Biology* 6.1, p. 016009. URL: `http://stacks.iop.org/1478-3975/6/i=1/a=016009` (cit. on pp. 7, 78).

Giessibl, F. J. (July 2003). „Advances in atomic force microscopy". In: *Reviews of Modern Physics* 75.3, pp. 949–983. DOI: `10.1103/RevModPhys.75.949` (cit. on p. 19).

Gingold, R. A. and J. J. Monaghan (1977). „Smoothed particle hydrodynamics-theory and application to non-spherical stars". In: *Monthly notices of the royal astronomical society* 181, pp. 375–389 (cit. on p. 7).

Graner, F. and J. A. Glazier (1992). „Simulation of Biological Cell Sorting Using a Two-Dimensional Extended Potts Model". In: *Physical Review Letters* 69, pp. 2013–2016. URL: `http://www.citeulike.org/user/Doug/article/2970604` (cit. on p. 5).

Graziano, L. and L. Preziosi (2007). „Mechanics in tumor growth". In: *Modeling of biological materials*. Springer, pp. 263–321 (cit. on p. 5).

Hategan, A., R. Law, S. Kahn, and D. E. Discher (2003). „Adhesively-Tensed Cell Membranes: Lysis Kinetics and Atomic Force Microscopy Probing". In: *Biophysical Journal* 85.4, pp. 2746–2759. ISSN: 0006-3495. DOI: `10.1016/S0006-3495(03)74697-9` (cit. on p. 59).

Hategan, A., K. Sengupta, S. Kahn, E. Sackmann, and D. E. Discher (2004). „Topographical Pattern Dynamics in Passive Adhesion of Cell Membranes". In: *Biophysical Journal* 87.5, pp. 3547–3560. ISSN: 0006-3495. DOI: `10.1529/biophysj.104.041475` (cit. on pp. 44, 56, 59, 60, 64–66).

He, K., S. Dong, and Z. Zhou (Mar. 2007). „Multigrid contact detection method". In: *Phys. Rev. E* 75.3, p. 036710 (cit. on p. 74).

Heath, M. T. (2005). *Scientific Computing: An Introductory Survey*. 2nd. McGraw-Hill (cit. on p. 75).

Henriksen, J. and J. Ipsen (2004). „Measurement of membrane elasticity by micropipette aspiration". In: *European Physical Journal E: Soft Matter* 14, pp. 149–167. DOI: `10.1140/epje/i2003-10146-y` (cit. on pp. 13, 14).

Herant, M. and M. Dembo (2010). „Cytopede: a three-dimensional tool for modeling cell motility on a flat surface". In: *Journal of Computational Biology* 17.12, pp. 1639–1677 (cit. on pp. 5, 6).

Hertz, H. (1881). „Ueber die Beruehrung fester elastischer Koerper". In: *Journal fuer die reine und angewandte Mathematik* 91, pp. 156–171 (cit. on p. 27).

Hinterdorfer, P. and Y. Dufrene (2006). „Detection and localization of single molecular recognition events using atomic force microscopy". In: *Nature Methods* 3.5, pp. 347–355 (cit. on pp. 22, 108).

Hochmuth, R. (2000). „Micropipette aspiration of living cells". In: *Journal of Biomechanics* 33, pp. 15–22 (cit. on p. 14).

Hoehme, S. and D. Drasdo (2005). „A single-cell-based model of tumor growth in vitro: monolayers and spheroids". In: *Physical Biology* 2, pp. 133–147 (cit. on pp. 7, 27, 54, 55).

Hoehme, S., M. Brulport, A. Bauer, E. Bedawy, W. Schormann, M. Hermes, V. Puppe, R. Gebhardt, S. Zellmer, M. Schwarz, E. Bockamp, T. Timmel, J. G. Hengstler, and D. Drasdo (2010). „Prediction and validation of cell alignment along microvessels as order principle to restore tissue architecture in liver regeneration". In: *Proceedings of the National Academy of Sciences* 107.23. Including Supporting information, pp. 10371–10376 (cit. on pp. 7, 55, 59).

Hoehme, S. and D. Drasdo (2010). „A cell-based simulation software for multicellular systems". In: *Bioinformatics* 26, pp. 2641–2642. DOI: `10.1093/bioinformatics/btq437` (cit. on pp. 8, 72).

Holcombe, M., S. Coakley, and R. Smallwood (2006). „A general framework for agent-based modelling of complex systems". In: *Proceedings of the 2006 European Conference on Complex Systems* (cit. on pp. 8, 72).

Huang, H., R. Kamm, and R. Lee (2004). „Cell mechanics and mechanotransduction: pathways, probes, and physiology". In: *American Journal of Physiology- Cell Physiology* 287.1, pp. C1–C11 (cit. on p. 85).

Hutter, J. L. and J. Bechhoefer (1993). „Calibration of atomic-force microscope tips". In: *Review of Scientific Instruments* 64, p. 1868. DOI: `10.1063/1.1143970` (cit. on pp. 98, 106).

Huveneers, S. and E. H. J. Danen (2009). „Adhesion signaling – crosstalk between integrins, Src and Rho". In: *Journal of Cell Science* 122, pp. 1059–1069. DOI: `doi:10.1242/jcs.039446` (cit. on p. 42).

Ingber, D. E. (2006). „Cellular mechanotransduction: putting all the pieces together again". In: *The FASEB Journal* 20.7, pp. 811–827. DOI: `10.1096/fj.05-5424rev` (cit. on p. 85).

Israelachvili, J. N. (2011). *Intermolecular and surface forces*. third edition. Academic press (cit. on pp. 28, 59, 65).

Jafari Bidhendi, A. and R. K. Korhonen (2012). „A finite element study of micropipette aspiration of single cells: effect of compressibility". In: *Computational and mathematical methods in medicine* 2012 (cit. on p. 14).

Johnson, K. L. and J. A. Greenwood (1997). „An Adhesion Map for the Contact of Elastic Spheres". In: *Journal of colloid and interface science* 192, pp. 326–333 (cit. on pp. 28, 47).

Johnson, K. L., K. Kendall, and A. Roberts (1971). „Surface energy and the contact of elastic solids". In: *Proceedings of the royal society* 324, pp. 301–313. URL: `http://www.jstor.org/pss/78058` (cit. on pp. 27, 47).

Johnson, K. (1997). „Adhesion and friction between a smooth elastic spherical asperity and a plane surface". In: *Proceedings of the Royal Society of London. Series A: Mathematical, Physical and Engineering Sciences* 453.1956, pp. 163–179 (cit. on p. 46).

Johnson, S. C. (1967). „Hierarchical clustering schemes". In: *Psychometrika* 32.3, pp. 241–254. DOI: `10.1007/BF02289588` (cit. on p. 33).

Kim, T., W. Hwang, H. Lee, and R. D. Kamm (July 2009). „Computational Analysis of Viscoelastic Properties of Crosslinked Actin Networks". In: *PLoS Computational Biology* 5.7. Ed. by D. A. Fletcher, e1000439. DOI: `10.1371/journal.pcbi.1000439` (cit. on p. 7).

Kosztin, I., G. Vunjak-Novakovic, and G. Forgacs (2012). „Colloquium: Modeling the dynamics of multicellular systems: Application to tissue engineering". In: *Reviews of Modern Physics* 84.4, pp. 1791–1805. DOI: `10.1103/RevModPhys.84.1791` (cit. on p. 7).

Kreft, J.-U., C. Picioreanu, J. W. T. Wimpenny, and M. C. M. van Loosdrecht (2001). „Individual-based modelling of biofilms". In: *Microbiology* 147, pp. 2897–2912 (cit. on p. 8).

Krinner, A., M. Hoffmann, M. Loeffler, D. Drasdo, and J. Galle (2010). „Individual fates of mesenchymal stem cells in vitro". In: *BMC Systems Biology* 4, pp. 1–9 (cit. on pp. 8, 55).

Kruskal, W. H. and W. A. Wallis (1952). „Use of ranks in one-criterion variance analysis". In: *Journal of the American statistical Association* 47.260, pp. 583–621. DOI: `10.1080/01621459.1952.10483441` (cit. on p. 21).

Leckband, D. and J. Israelachvili (2001). „Intermolecular forces in biology". In: *Quarterly Reviews of Biophysics* 34(2), pp. 105–267 (cit. on pp. 57, 62, 65).

Legant, W., C. Choi, J. Miller, L. Shao, L. Gao, E. Betzig, and C. Chen (2013). „Multidimensional traction force microscopy reveals out-of-plane rotational moments about focal adhesions". In: *PNAS* 110(3), pp. 881–886 (cit. on p. 64).

Lenas, P., M. Moos, and F. Luyten (2009a). „Developmental engineering: a new paradigm for the design and manufacturing of cell-based products. Part I: from three-dimensional cell growth to biomimetics of *in vivo* development". In: *Tissue Engineering: Part B* 15(4), 381:394 (cit. on p. 2).

— (2009b). „Developmental engineering: a new paradigm for the design and manufacturing of cell-based products. Part II. From genes to networks: tissue engineering from the viewpoint of systems biology and network science". In: *Tissue Engineering: Part B* 15(4), pp. 395–422 (cit. on p. 2).

Li, S., J.-L. Guan, and S. Chien (Aug. 2005). „BIOCHEMISTRY AND BIOMECHANICS OF CELL MOTILITY". In: *Annual Review of Biomedical Engineering* 7.1, pp. 105–150. DOI: `10.1146/annurev.bioeng.7.060804.100340` (cit. on p. 2).

Li, X., P. M. Vlahovska, and G. E. Karniadakis (2013). „Continuum- and particle-based modeling of shapes and dynamics of red blood cells in health and disease". In: *Soft Matter* 9 (1), pp. 28–37. DOI: `10.1039/C2SM26891D` (cit. on p. 44).

Lipke, P. N., M. C. Garcia, D. Alsteens, C. B. Ramsook, S. A. Klotz, and Y. F. Dufrêne (2012). „Strengthening relationships: amyloids create adhesion nanodomains in yeasts". In: *Trends in Microbiology* 20.2, pp. 59–65. ISSN: 0966-842X. DOI: `10.1016/j.tim.2011.10.002` (cit. on p. 22).

Lu, M. and G. McDowell (2007). „The importance of modelling ballast particle shape in the discrete element method". In: *Granular Matter* 9, pp. 69–80 (cit. on p. 43).

Macklin, P., M. E. Edgerton, A. M. Thompson, and V. Cristini (May 2012). „Patient-calibrated agent-based modelling of ductal carcinoma in situ (DCIS): From microscopic measurements to macroscopic predictions of clinical progression". In: *Journal of Theoretical Biology* 301, pp. 122–140. DOI: `10.1016/j.jtbi.2012.02.002` (cit. on p. 7).

Matteo, M. (n.d.). *A Tutorial on Clustering Algorithms*. URL: `http://home.deib.polimi.it/matteucc/Clustering/tutorial_html/hierarchical.html` (cit. on p. 33).

Matuttis, H., S. Luding, and H. Herrman (2000). „Discrete element simulations of dense packings and heaps made of spherical and non-spherical particles". In: *Powder Technology* 108, pp. 278–292 (cit. on p. 43).

Maugis, D. (1992). „Adhesion of spheres: The JKR-DMT transition using a Dugdale model". In: *Journal of Colloid and Interface Science* 150.1, pp. 243–269. ISSN: 0021-9797. DOI: `10.1016/0021-9797(92)90285-T` (cit. on pp. 45, 46).

Maurin, B., P. Canadas, H. Baudriller, P. Montcourrier, and N. Bettache (Jan. 2008). „Mechanical model of cytoskeleton structuration during cell adhesion and spreading". In: *Journal of Biomechanics* 41.9, pp. 2036–2041. DOI: `10.1016/j.jbiomech.2008.03.011` (cit. on p. 7).

Meyer, M., M. Desbrun, P. Schröder, and A. H. Barr (2002). „Discrete Differential-Geometry Operators for Triangulated Manifolds". In: *Visualization and Mathematics* 3.7, pp. 35–57 (cit. on p. 49).

Mirams, G. R., C. J. Arthurs, M. O. Bernabeu, R. Bordas, J. Cooper, A. Corrias, Y. Davit, S.-J. Dunn, A. G. Fletcher, D. G. Harvey, et al. (2013). „Chaste: An Open Source C++ Library for Computational Physiology and Biology". In: *PLoS computational biology* 9.3, e1002970 (cit. on pp. 8, 72).

Morton, C. I., L. Hlatky, P. Hahnfeldt, and H. Enderling (2011). „Non-Stem Cancer Cell Kinetics Modulate Solid Tumor Progression". In: *Theoretical Biology and Medical Modelling* 8.1, p. 48. DOI: `10.1186/1742-4682-8-48` (cit. on p. 4).

Nadell, C. D., K. R. Foster, and J. B. Xavier (2010). „Emergence of spatial structure in cell groups and the evolution of cooperation". In: *PLoS computational biology* 6.3, e1000716 (cit. on p. 39).

NanoWizard 3 User Manual SPM Software Release 4.2 (Sept. 2012). JPK Instruments AG. Bouchéstraße 12 12435 Berlin (cit. on p. 98).

Newman, T. J. (2005). „Modeling multicellular systems using subcellular elements". In: *Mathematical Biosciences and Engineering* 2.3, pp. 613–624. URL: `http://arxiv.org/abs/q-bio/0504028` (cit. on p. 7).

Noble, D. (2002). „The rise of computational biology". In: *Nature Reviews Molecular Cell Biology* 3.6, pp. 459–463. DOI: `10.1038/nrm810` (cit. on pp. 1, 2).

Odenthal, T., B. Smeets, J. Christiaens, K. Verstrepen, E. Tijskens, and H. Ramon (Apr. 2012). „EVOLUTION OF ADHESION PROPERTIES IN YEAST". In: *Proceedings of the 10th International Symposium on Computer Methods in Biomechanics and Biomedical Engineering*. Arup, pp. 431–437 (cit. on pp. 9, 10, 25, 85).

Odenthal, T., B. Smeets, P. Van Liedekerke, E. Tijskens, H. Van Oosterwyck, and H. Ramon (2013). „Analysis of initial cell spreading using mechanistic contact formulations for a deformable cell model". In: *PLoS Computational Biology* 9.10, e1003267. DOI: `10.1371/journal.pcbi.1003267` (cit. on pp. 10, 42, 78, 85).

office, C. press (Mar. 2013). *New results indicate that particle discovered at CERN is a Higgs boson*. CERN. URL: `http://press.web.cern.ch/press-releases/2013/03/new-results-indicate-particle-discovered-cern-higgs-boson` (cit. on p. 1).

OverlordQ (2009). *Atomic force microscope block diagram*. URL: `http://upload.wikimedia.org/wikipedia/commons/7/7c/Atomic_force_microscope_block_diagram.svg` (cit. on p. 18).

Palsson, E. (Sept. 2008). „A 3-D model used to explore how cell adhesion and stiffness affect cell sorting and movement in multicellular systems". In: *Journal of Theoretical Biology* 254.1, pp. 1–13. DOI: `10.1016/j.jtbi.2008.05.004` (cit. on p. 35).

Palsson, E. and H. G. Othmer (2000). „A model for individual and collective cell movement in Dictyostelium discoideum". In: *Proceedings of the National Academy of Sciences* 97.19, pp. 10448–10453. DOI: `10.1073/pnas.97.19.10448` (cit. on p. 8).

Pathmanathan, P., J. Cooper, A. Fletcher, G. Mirams, L. Montahan, P. Murray, J. Osborne, J. Pitt-Francis, A. Walter, and S. J. Chapman (2009). „A computational study of discrete mechanical tissue models". In: *Physical Biology* 6(3), p. 036001. URL: `http://www.iop.org/EJ/abstract/1478-3975/6/3/036001/` (cit. on p. 27).

Pelling, A. E., S. Sehati, E. B. Gralla, J. S. Valentine, and J. K. Gimzewski (2004). „Local Nanomechanical Motion of the Cell Wall of Saccharomyces cerevisiae". In: *Science* 305, pp. 1147–1150 (cit. on p. 21).

Peng, Z., X. Li, I. V. Pivkin, M. Dao, G. E. Karniadakis, and S. Suresh (2013). „Lipid bilayer and cytoskeletal interactions in a red blood cell". In: *Proceedings of the National Academy of Sciences* (cit. on pp. 7, 44).

Pöschel, T. and T. Schwager (2005). *Computational Granular Dynamics*. Springer (cit. on p. 43).

Purcell, E. (1977). „Life at low Reynolds-number". In: *American Journal of Physics* 45, pp. 3–11. URL: `http://www.nada.kth.se/~annak/Low_RE.pdf` (cit. on pp. 3, 54).

Qu, Z., J. N. Weiss, and W. R. MacLellan (2004). „Coordination of cell growth and cell division: a mathematical modeling study". In: *Journal of Cell Science* 117, pp. 4199–4207. URL: `http://jcs.biologists.org/cgi/content/abstract/jcs.01294v1` (cit. on p. 29).

Radmacher, M. (1997). „Measuring the Elastic Properties of Biological Samples with the AFM". In: *IEEE Engineering in Medicine and Biology* 97, pp. 47–57 (cit. on p. 17).

Ramis-Conde, I., M. A. J. Chaplain, A. R. A. Anderson, and D. Drasdo (2009). „Multiscale modelling of cancer cell intravasation: the role of cadherins in metastasis". In: *Physical Biology* 6, p. 016008. DOI: `10.1088/1478-3975/6/1/016008` (cit. on pp. 8, 55).

Salgado, A., O. Coutinho, and R. Reis (2004). „Bone tissue engineering: state of the art and future trends". In: *Macromolecular bioscience* 4, pp. 743–765. DOI: `10.1002/mabi.200400026` (cit. on p. 2).

Schaller, G. and M. Meyer-Hermann (May 2005). „Multicellular tumor spheroid in an off-lattice Voronoi-Delaunay cell model". In: *Physical Review E* 71.5, pages. DOI: `10.1103/PhysRevE.71.051910` (cit. on p. 5).

Schlüter, D. K., I. Ramis-Conde, and M. A. J. Chaplain (Sept. 2012). „Computational Modeling of Single-Cell Migration: The Leading Role of Extracellular Matrix Fibers". In: *Biophysical Journal* 103.6, pp. 1141–1151. DOI: `10.1016/j.bpj.2012.07.048` (cit. on p. 8).

Seifert, U. and R. Lipowsky (1990). „Adhesion of vesicles". In: *Physical Review A* 42(8), pp. 4768–4771 (cit. on pp. 59, 62).

Sivak, D. A., J. D. Chodera, and G. E. Crooks (Jan. 2013). „Using Nonequilibrium Fluctuation Theorems to Understand and Correct Errors in Equilibrium and Nonequilibrium Simulations of Discrete Langevin Dynamics". In: *Phys. Rev. X* 3 (1), p. 011007. DOI: `10.1103/PhysRevX.3.011007` (cit. on p. 112).

Smeets, B. (2010). „Individuele-cel modellen van gistkolonies: een discrete-elementen benadering". MA thesis. KU Leuven (cit. on pp. 9, 25, 29, 31).

Smeets, B., T. Odenthal, E. Tijskens, H. Ramon, and H. Van Oosterwyck (2013). „Quantifying the Mechanical Micro-environment during Three-dimensional Cell Expansion on Microbeads by means of Individual Cell-based Modelling". In: *Computer Methods in Biomechanics and Biomedical Engineering* 16.10, pp. 1071–1084. DOI: `10.1080/10255842.2013.829461` (cit. on pp. 8, 9, 77, 78, 84, 85).

Smeets, B., T. Odenthal, H. Van Oosterwyck, and H. Ramon (2012). „CHARACTERIZING THE MECHANICAL MICROENVIRONMENT OF 3D CELL CULTURES USING INDIVIDUAL-BASED MODELS". In: *Proceedings of the 10th International Symposium on Computer Methods in Biomechanics and Biomedical Engineering*. Arup, pp. 135–141 (cit. on p. 9).

Smukalla, S., M. Caldara, N. Pochet, A. Beauvais, S. Guadagnini, C. Yan, M. D. Vinces, A. Jansen, M. C. Prevost, J.-P. Latgé, G. R. Fink, K. R. Foster, and K. J. Verstrepen (2008). „FLO1 Is a Variable Green Beard Gene that Drives Biofilm-like Cooperation in Budding Yeast". In: *Cell* 135, pp. 726–737. DOI: `10.1016/j.cell.2008.09.037` (cit. on pp. 26, 31).

Spillmann, J. and M. Teschner (2005). „Contact surface computation for coarsely sampled deformable objects". In: *Proc. Vision, Modeling, Visualization*, pp. 289–296 (cit. on p. 43).

Suchodolskis, A., V. Feiza, A. Stirke, A. Timonina, A. Ramanaviciene, and A. Ramanavicius (2011). „Elastic properties of chemically modified baker's yeast cells studied by AFM". In: *Surface and Interface Analysis* 43(13), 1636–1640 (cit. on p. 17).

Suresh, S., J. Spatz, J. Mills, A. Micoulet, M. Dao, C. Lim, M. Beil, and T. Seufferlein (2005). „Connections between single-cell biomechanics and human disease states: gastrointestinal cancer and malaria". In: *Acta Biomaterialia* 1.1, pp. 15–30 (cit. on pp. 55–57).

Tijskens, E., H. Ramon, and J. De Baerdemaeker (2003). „Discrete element modelling for process simulation in agriculture”. In: *Journal of Sound and Vibration* 266.3, pp. 493–514. ISSN: 0022-460X. DOI: 10.1016/S0022-460X(03)00581-9 (cit. on pp. 27, 72, 119).

Tipler, P. A. (2000). *Physik*. Spektrum Akademischer Verlag (cit. on p. 17).

Touhami, A., B. Hoffmann, A. Vasella, F. A. Denis, and Y. Dufrene (2003). „Aggregation of yeast cells: direct measurement of discrete lectinñcarbohydrate interactions”. In: *Microbiology* 149, 2873ñ2878. URL: http://mic.sgmjournals.org/cgi/content/abstract/149/10/2873 (cit. on p. 31).

Touhami, A., B. Nysten, and Y. Dufrene (2003). „Nanoscale mapping of the elasticity of microbial cells by atomic force microscopy”. In: *Langmuir* 19.11, pp. 4539–4543 (cit. on pp. 20, 21).

Ullersma, P. (1966). „An exactly solvable model for Brownian motion: I. Derivation of the Langevin equation”. In: *Physica* 32.1, pp. 27–55. ISSN: 0031-8914. DOI: 10.1016/0031-8914(66)90102-9 (cit. on p. 3).

Van Liedekerke, P., P. Ghysels, E. Tijskens, G. Samaey, B. Smeets, D. Roose, and H. Ramon (2010). „A particle-based model to simulate the micromechanics of single-plant parenchyma cells and aggregates”. In: *Physical Biology* 7, p. 026006. DOI: 10.1088/1478-3975/7/2/026006 (cit. on p. 7).

Van Liedekerke, P., B. Smeets, T. Odenthal, E. Tijskens, and H. Ramon (2013). „Solving microscopic flow problems using Stokes equations in SPH”. In: *Computer Physics Communications* 184, pp. 1686–1696. DOI: 10.1016/j.cpc.2013.02.013 (cit. on pp. 55, 56, 78, 79, 85, 114).

Van Liedekerke, P., P. Ghysels, E. Tijskens, G. Samaey, D. Roose, and H. Ramon (2011). „Mechanisms of soft cellular tissue bruising. A particle based simulation approach”. In: *Soft Matter* 7.7, p. 3580. DOI: 10.1039/c0sm01261k (cit. on p. 78).

Van Liedekerke, P., E. Tijskens, H. Ramon, P. Ghysels, G. Samaey, and D. Roose (June 2010). „Particle-based model to simulate the micromechanics of biological cells”. In: *PHYSICAL REVIEW E* 81.6, Part 1, pages. ISSN: 1539-3755. DOI: 10.1103/PhysRevE.81.061906 (cit. on pp. 7, 48, 78).

Van Oosterwyck, H., J. F. Rodríguez, M. Doblaré, and J. M. G. Aznar (2012). „An affine micro-sphere-based constitutive model, accounting for junctional sliding, can capture F-actin network mechanics”. In: *Computer Methods in Biomechanics and Biomedical Engineering*, pp. 1–11. DOI: 10.1080/10255842.2011.648626 (cit. on p. 69).

Vanmaercke, S., E. Tijskens, G. Van den Eynde, and Y. Bartosiewicz (2011). „Numerical and experimental study of a spherical particle flow in a cylindrical tube under vacuum conditions”. In: *Granular Matter* 13.6, pp. 713–721 (cit. on p. 72).

Wang, N., E. Ostuni, G. Whitesides, and D. Ingber (2002). „Micropatterning Tractional Forces in Living Cells”. In: *Cell Motility and the Cytoskeleton* 52, pp. 97–106 (cit. on pp. 64, 67).

Werner, C. (2004). „Cell adhesion to polymer substrates characterized by the micropipette aspiration technique". In: *Journal of Adhesion* 80.10-11, pp. 895–911 (cit. on p. 14).

Wriggers, W., J. X. Tang, T. Azuma, P. W. Marks, and P. A. Janmey (Oct. 1998). „Cofilin and gelsolin segment-1: molecular dynamics simulation and biochemical analysis predict a similar actin binding mode". In: *Journal of Molecular Biology* 282.5, pp. 921–932. DOI: `10.1006/jmbi.1998.2048` (cit. on p. 6).

Xu, G. (2006). „Discrete Laplace–Beltrami operator on sphere and optimal spherical triangulations". In: *International Journal of Computational Geometry & Applications* 16, pp. 75–93 (cit. on p. 48).

Zhang, L., T. Cui, and H. Liu (2009). „A set of symmetric quadrature rules on triangles and tetrahedra". In: *J. Comput. Math* 27, pp. 89–96 (cit. on pp. 50, 51).

Zhang, X., A. Chen, D. De Leon, H. Li, E. Noiri, V. T. Moy, and M. S. Goligorsky (2004). „Atomic force microscopy measurement of leukocyte-endothelial interaction". In: *American Journal of Physiology-Heart and Circulatory Physiology* 286.1, H359–H367 (cit. on p. 108).

Zienkiewicz, O. C. and R. L. Taylor (2000). *The Finite Element Method: Solid Mechanics*. Vol. 2. Butterworth-Heinemann (cit. on p. 2).

Zygourakis, K., R. Bizios, and P. Markenscoff (Aug. 1991). „Proliferation of anchorage-dependent contact-inhibited cells: I. Development of theoretical models based on cellular automata". In: *Biotechnology and Bioengineering* 38.5, pp. 459–470. DOI: `10.1002/bit.260380504` (cit. on p. 5).

Curriculum Vitae

Tim Odenthal

Address: Mercuriusstraat 5/7
1930 Nossegem
België

Mobile: +32 474 32 42 38

Email: Tim.Odenthal@biw.kuleuven.be

Date of birth: 01 March 1983

Nationality: German

Profile

Highly motivated PhD-student of Bioengineering with a wide field of interest and focus areas in Biophysics, especially cell-mechanics and individual cell-based models, as well as atomic force microscopy experiments.

Education

2009 - today: PhD researcher at MeBioS, group computational cell mechanics, faculty of Bioengineering, KU Leuven

2003 - 2009: Studies of physics (final degree: Diplom)
Rheinische Friedrich-Wilhelms-Universität Bonn, Germany

Final result (Diplomprüfungen): Very Good (Sehr gut)

Experimental Physics:	1.0	Theoretical Physics:	1.7
Hadron & Detector Physics:	1.0	Biochemistry:	1.0

Thesis: Good (Gut)

field excursions to CERN (Genf), DESY (Hamburg), Karmann (Osnabrück)

8 - 13/06/08: DPG Physics School Biophysics at Interfaces, Bad Honnef

1994 - 2002: Abitur, University Entrance Exams, Grade range: Very good,
(German average score: 1.2),
Norbert-Gymnasium Knechtsteden, Dormagen

Professional Experience

2008 – 2009: **Teaching assistant** for experimental physics for non-physicists, Universität Bonn

2007 – 2008: **Research assistant** at the experimental anaesthesiology department, Universität Bonn (Prof. Dr. B.W. Urban)

2002 - 2003: **National service (Zivildienst)** as elderly care assistant, Seniorenzentrum Albert-Schweitzer Haus, Grevenbroich

05/03 – 06/03: **Intern**, Bayer Industry Services (BIS - PT - MT), department Physics & Chemistry of Interfaces, Leverkusen

Skills:

Language Skills: German (native), English (advanced), Dutch (advanced), French (basic)

Programming Skills: C(++), Python, Matlab, R

Publications

Journal Articles & full Proceedings

Nanova, M., V. Metag, E. Y. Paryev, D. Bayadilov, B. Bantes, R. Beck, Y. Beloglazov, S. Böse, K.-T. Brinkmann, T. Challand, V. Crede, T. Dahlke, F. Dietz, P. Drexler, H. Eberhardt, D. Elsner, R. Ewald, K. Fornet-Ponse, S. Friedrich, F. Frommberger, C. Funke, M. Gottschall, A. Gridnev, M. Grüner, E. Gutz, C. Hammann, D. Hammann, J. Hannappel, J. Hartmann, W. Hillert, P. Hoffmeister, C. Honisch, I. Jaegle, D. Kaiser, H. Kalinowsky, S. Kammer, I. Keshelashvili, V. Kleber, F. Klein, E. Klempt, B. Krusche, M. Lang, Y. Lopatin I. V. abd Maghrbi, K. Makonyi, J. Müller, T. Odenthal, D. Piontek, S. Schaepe, C. Schmidt, H. Schmieden, R. Schmitz, T. Seifen, A. Thiel, U. Thoma, H. van Pee, D. Walther, C. Wendel, U. Wiedner, A. Wilson, A. Winnebeck, and F. Zenke (2013). „Determination of the η'-nucleus optical potential". In: *arXiv preprint arXiv:1311.0122*.

Odenthal, T., B. Smeets, J. Christiaens, K. Verstrepen, E. Tijskens, and H. Ramon (Apr. 2012). „EVOLUTION OF ADHESION PROPERTIES IN YEAST". In: *Proceedings of the 10th International Symposium on Computer Methods in Biomechanics and Biomedical Engineering*. Arup, pp. 431–437.

Odenthal, T., B. Smeets, P. Van Liedekerke, E. Tijskens, H. Van Oosterwyck, and H. Ramon (2013). „Analysis of initial cell spreading using mechanistic contact formulations for a deformable cell model". In: *PLoS Computational Biology* 9.10, e1003267. DOI: `10.1371/journal.pcbi.1003267`.

Smeets, B., T. Odenthal, J. Keresztes, S. Vanmaercke, and H. Ramon (2013). „Virtueel fruit: hoe computersimulaties helpen bij preventies van blutsschade". In: *Fruitteeltnieuws* 19-20, pp. 18–19.

Smeets, B., T. Odenthal, E. Tijskens, H. Ramon, and H. Van Oosterwyck (2013). „Quantifying the Mechanical Micro-environment during Three-dimensional Cell Expansion on Microbeads by means of Individual Cell-based Modelling". In: *Computer Methods in Biomechanics and Biomedical Engineering* 16.10, pp. 1071–1084. DOI: `10.1080/10255842.2013.829461`.

Smeets, B., T. Odenthal, H. Van Oosterwyck, and H. Ramon (2012). „CHARACTERIZING THE MECHANICAL MICROENVIRONMENT OF 3D CELL CULTURES USING INDIVIDUAL-BASED MODELS”. In: *Proceedings of the 10th International Symposium on Computer Methods in Biomechanics and Biomedical Engineering*. Arup, pp. 135–141.

Van Liedekerke, P., B. Smeets, T. Odenthal, E. Tijskens, and H. Ramon (2013). „Solving microscopic flow problems using Stokes equations in SPH”. In: *Computer Physics Communications* 184, pp. 1686–1696. DOI: `10.1016/j.cpc.2013.02.013`.

International conferences

Odenthal, T., B. Smeets, H. Ramon, and H. Van Oosterwyck (2013). „Initial cell spreading investigated by a deformable cell model with mechanistic contact interactions”. In: *Conference on Particle-Based Methods PARTICLES*.

Odenthal, T., B. Smeets, K. Sliogeryte, P. Van Liedekerke, and E. Tijskens (2010). „DEM in Biological Physics: Simulating Yeast Colony Growth.” In: *International PhD & Research Day of the International Fine Particles Reasearch Institute (IFPRI)*.

Odenthal, T., B. Smeets, K. Sliogeryte, P. Van Liedekerke, E. Tijskens, and H. Ramon (2011). „DEM in Biological Physics: Individual-cell Based Models.” In: *European Cell Mechanics Meeting*.

Odenthal, T., B. Smeets, P. Van Liedekerke, E. Tijskens, V. Oosterwyck, and H. Ramon (2013). „A DEFORMABLE CELL MODEL AND ITS APPLICATION TO INVESTIGATE INITIAL CELL SPREADING”. In: *International Symposium on Computer Methods in Biomechanics and Biomedical Engineering*. Best Student Poster Presentation Prize.

Odenthal, T., B. Smeets, P. Van Liedekerke, E. Tijskens, and H. Ramon (2010). „Particle based simulation of cell growth and cell colony growth.” In: *Statistical Physics and Biology of Collective Motion*.

Odenthal, T., B. Smeets, P. Van Liedekerke, E. Tijskens, H. Ramon, and H. Van Oosterwyck (2013). „INITIAL CELL SPREADING INVESTIGATED BY A NEW DEFORMABLE CELL MODEL”. In: *International Conference on Computational Bioengineering*.

Odenthal, T., B. Smeets, P. Van Liedekerke, E. Tijskens, H. Van Oosterwyck, and H. Ramon (2012). „Particle-based Methods for Simulating Tissue.” In: *Belgian Symposium on Tissue Engineering*.

Smeets, B., T. Odenthal, H. Ramon, and H. Van Oosterwyck (17-18 September 2012). „Individual-based Modeling of Microcarrier Cell Expansion: A Sensitivity Analysis”. In: *Belgian Symposium on Tissue Engineering*. Leuven, Belgium.

— (24-25 October 2013a). „Particle-based methods for Tissue Engineering”. In: *Belgian Symposium on Tissue Engineering*. Leuven, Belgium.

— (18-20 September 2013b). „Quantifying mechanical heterogeneity in microbead cell expansion using individual-cell based models". In: *International Conference on Particle-based Methods*. Stuttgart, Germany.

Smeets, B., T. Odenthal, K. Sliogeryte, P. Van Liedekerke, and H. Ramon (17-19 October 2011). „Differential Adhesion and Socio-Evolution in Yeast". In: *European Cell Mechanics Meeting*. P37. Amsterdam, Netherlands.

Smeets, B., T. Odenthal, E. Tijskens, H. Ramon, and H. Van Oosterwyck (Nov. 2013a). „Individual-based modelling of the mechanical microenvironment". In: *International Conference on Computational Bioengineering*. Leuven, Belgium.

— (25-28 August 2013b). „The microenvironment for microbead cell expansion: mechanical characterization employing an individual-cell based model". In: *Congress of the European Society of Biomechanics*. Congress of the European Society of Biomechanics. Patras, Greece.

Smeets, B., T. Odenthal, E. Tijskens, S. Roberts, W. Tam, P. Van Liedekerke, H. Van Oosterwyck, and H. Ramon (2012). „Influence of mechanics on microcarrier cell expansion: a computational study." In: *Journal of Tissue Engineering and Regenerative Medicine: vol. 6. TERMIS World Congress.*

Smeets, B., T. Odenthal, P. Van Liedekerke, E. Tijskens, H. Ramon, and H. Van Oosterwyck (Mar. 2013). „Individual-cell based model for characterizing the mechanical microenvironment in microcarrier cell expansion". In: *Computer Methods in Biomechanics and Biomedical Engineering*. Salt Lake City, UT.

Smeets, B., T. Odenthal, P. Van Liedekerke, E. Tijskens, H. Van Oosterwyck, and H. Ramon (28 September - 2 October 2013). „Mechanical stress in microcarrier cell expansion investigated with a deformable cell model". In: *European Cell Mechanics Meeting*. Obergurgl, Austria.

Van Liedekerke, P., T. Odenthal, B. Smeets, E. Tijskens, and H. Ramon (2013). „SOLVING MICROSCOPIC FLOW PROBLEMS USING STOKES EQUATIONS IN SPH". In: *International Conference on Computational Bioengineering*.

FACULTY OF BIOSCIENCE ENGINEERING
DEPARTMENT OF BIOSYSTEMS
MEBIOS - COMPUTATIONAL CELL MECHANICS
Kasteelpark Arenberg 30 bus 2456
B-3001 Heverlee
Tim.Odenthal@biw.kuleuven.be
http://www.mebios.be